2017-01-01

Design And Regioselective SynThesis Of Fullerene Derivatives For Metal-Organic Hybrid Architectures

Catalina Suarez
University of Texas at El Paso, catalinasuarez.v@gmail.com

DESIGN AND REGIOSELECTIVE SYNTHESIS OF FULLERENE DERIVATIVES FOR METAL-ORGANIC HYBRID ARCHITECTURES

CATALINA SUAREZ VALLEJO

Master's Program in Chemistry

APPROVED:

Luis A. Echegoyen, Ph.D., Chair

Skye Fortier, Ph.D.

Yaoqiu Zhu, Ph.D.

Tunna Baruah, Ph.D.

Charles Ambler, Ph.D.
Dean of the Graduate School

Dedication

To Mors, for making my life better since the first day we met. Thank you for never stopping believing in me, even when I did.

DESIGN AND REGIOSELECTIVE SYNTHESIS OF FULLERENE DERIVATIVES FOR METAL-ORGANIC HYBRID ARCHITECTURES

by

CATALINA SUAREZ VALLEJO

THESIS

Presented to the Faculty of the Graduate School of

The University of Texas at El Paso

in Partial Fulfillment

of the Requirements

for the Degree of

MASTER OF SCIENCE

Department of Chemistry

THE UNIVERSITY OF TEXAS AT EL PASO

August 2017

Abstract

In the last years different fullerene derivatives and endohedral fullerenes have been reported and their potential applications as electronic, magnetic, catalytic, biological and optical materials have been explored. In this work we describe the characterization of new endohedral fullerenes; the exohedral functionalization of fullerenes with organic addends or metal clusters and their application in metal-organic hybrid architectures.

We synthesized fullerene polymers with a variety of staircase linear architectures, zigzag polymers and a perfectly linear polymer using an *hexakis*-fullerene adduct with two 4,5-diazafluorene groups located at *trans*-**1** positions, using Hg, Cd, Zn and33 Cu as the metal centers. Our results showed that both, the metal and the metal:ligand ratio, have an impact on the structural and optical properties of the polymeric chains. To date, there are no reports of a 3D porous-metal organic framework (MOF) where fullerenes are used as integral linkers of the structure as opposed to adsorbed inside the pores. We designed, synthesized and characterized different carboxylate-fullerene derivatives to be used as integral linkers in MOFs. Furthermore, we explored the construction of fullerene based bimetallic units; we synthesized a discrete molecular system using dimolybdenum units and a carboxylate fullerene derivative. Of particular interest is the electronic coupling between the metallic center and the fullerene cage. For the synthesis of the carboxylate fullerene derivative we explored an unprecedented synthetic methodology for 1,3-dipolar cycloaddition reactions.

We also purified and characterized an endohedral fullerene with formula Lu_2C_{82}. Our results indicate that Lu_2C_{82} corresponds to the dimetallic endohedral $Lu_2@C_{82}$ and not to the corresponding carbide $Lu_2C_2@C_{80}$. The dimetallic endohedral was characterized by MALDI-TOF MS, UV spectrometry and electrochemistry. Finally, we synthesized the first *bis*-parallel C_{60}-metal cluster complex: *parallel*-$[Ru_3(CO)_9]_2\{\mu_3\text{-}\eta^2,\eta^2,\eta^2\text{-}C_{60}[C(COOC_2H_5)_2]_4\}$.

Table of Contents

Abstract v

Table of Contents vi

List of Tables x

List of Figures xi

Chapter 1: [60] Fullerene Based Supramolecular Architectures 1

1.1 Introduction 1

1.1.1 Derivatization of C_{60} 1

1.1.2 Fullerene based metallopolymers 3

1.2 Results And Discussion 9

1.3 Conlusions 17

1.4 Future Work 18

1.4 Experimental Section 19

1.4.1. Orthogonal transposition method: 19

Synthesis of compound 3. 19

Synthesis of compound 4. 19

Synthesis of compound 5. 20

1.4.2. Metallopolymers: 20

Synthesis of compound 6: 20

Synthesis of polymer 10: 20

Synthesis of polymer 11: 21

Synthesis of polymer 12: 21

Synthesis of polymer 13: 21

Synthesis of polymer 14: 21

Crystallographic data: 21

Chapter 2: Fullerene Based Metal Organic Frameworks 23

2.1 Introduction 23

2.1.1 Metal Organic Frameworks 24

2.1.2 Fullerenes as hydrogen storage materials 25

2.1.3 Fullerene and MOFs 28

2.1.3.1 Fullerenes inside MOFs 28
2.1.3.2 Fullerene-based MOFs 29
2.2 Results And Discussion 31
2.3 Future Work 36
2.4 experimental Section 37
2.4.1 Instrumentation 37
2.4.2 Synthesis of compound 16 37
Synthesis of compound 16a: 37
Synthesis of compound 16b: 38
Synthesis of compound 16: 38
2.4.3 Synthesis of compound 17 38
Synthesis of compound 17a: 39
Synthesis of compound 17b: 39
Synthesis of compound 17D: 40
Synthesis of compound 17e: 40
Synthesis of compound 16g: 40
2.4.4 Synthesis of compound 18 41
Synthesis of compound 18a: 41
Synthesis of compound 18b: 41
Synthesis of compound 18c: 41
2.4.4 Synthesis of compound 19 42
2.4.5 Synthesis of BODIPY 42
Synthesis of compound B1: 43
Synthesis of compound B2: 43
2.4.4 Synthesis of MOFs 43
Synthesis of MOF-3 43
Synthesis of MOF-4 44
Chapter 3: Fullerene-based Bimetallic Assemblies 45
3.1 Introduction 45
3.2 Results And Discussion 46
3.3 Future Work 50
3.4 Experimental Section 51

Synthesis of compound 28. 51

Chapter 4: 1,3-Dipolar Cycloadditions to Fullerenes 52

4.1. Introduction 52

4.1. 1. 1,3-dipolar cycloaddition 52

4.2 Results And Discussion 53

4.3 Conclusions 65

4.4 Experimental Section 65

4.4.1 Synthesis 65

Synthesis of compounds 32b and 33b 66

Synthesis of compounds 35 and 37 66

Synthesis of compounds 32a and 33a 66

Synthesis of compounds 34 and 36 67

Synthesis of compound 28 67

Synthesis of compounds 30 67

Chapter 5: Isolation And Characterization Of The Dimetallofullerene $Lu_2@C_{3v}(8)$-C_{82} 68

5.1 introduction 68

5.1.2 Dimetallofullerenes and carbide fullerenes 68

4.2 Results And Discussion 70

6.3 Conclusions 75

6.4 Experimental Methods 75

Chapter 6: Exohedral Metallic Clusters On C_{60} 76

6.1 Introduction 76

6.1.1 Exohedral complexes on C_{60} 76

6.3 Conclusions 84

6.4 experimental section 84

6.4.1 General methods 84

6.4.2 Synthesis 85

Reaction of compound 39 and $Ru_3(CO)_{12}$ 85

Characterization of 40. 85

Characterization of parallel-3 and tilted-3. 86

6.4.2 Crystallographic Data 86

X-ray Crystallography and Data Collection of 40. 86
X-ray Crystallography and Data Collection of parallel-3. 87
6.4.2 Plots 87
References 88
Appendix 99
Appendix 1 99
Appendix 2 100
Appendix 3 101
crystal structure report for complex 8 102
crystal structure report for polymer 13 104
crystal structure report for polymer 14 106
Vita… 109

List of Tables

Table 1.1: Distances between cages and cage-metal-cage angles in the different polymers,..... 15
Table 4.1. Conditions and product yields for the reactions between primary amines, 3a and 3b, and ethylbromoacetate. 56
Table 4.2. Reaction conditions and product yields for the reactions between compounds **34** or **35** with C_{60}. Paraformaldehyde was added to the reactions. 58
Table 4.3. Reaction conditions and product yields for the reactions between compounds **36** or **37** with C_{60} without the addition of paraformaldehyde. 60
Table 4.4. Reaction conditions and product yields for the reaction between compound **37** and C_{60} with the addition of pyridine. 65
Table 5.1: Computed energies for the most stable isomers of $Lu_2@C_{82}$ and $Lu_2C_2@C_{80}$ 73
Table 5.2: HOMO-LUMO levels for isomers 6 and 8 of $Lu_2@C_{82}$. 75

List of Figures

Figure 1.1: Hirsch nomenclature for the eight regioisomers (depicted in different colors) for C60 bis-adducts with respect to the first addition (purple bond). 2
Figure 1.2: Orthogonal transposition method. Malonates are designated with red balls representing $-C(CO_2Et)_2$ groups. 2
Figure 1.3: *Hexa*-adduct with two 4,5-diazofluorene groups in *trans*-**1** position relative to each other. As in figure 1.2, the malonate groups are represented with red balls. 3
Figure 1.4: Crystal structure of the first fullerene-metal sandwich complex {Rh6(CO)5(dppm)2(CNR)}{μ3-η2, η2, η2-{(C60)2}}. Reproduced with permission from ref21. Copyright Elsevier B. V. Appendix 1. 4
Figure 1.5: Representation of metal-organic polymer {Ni(Me3P)2](μ-η2,η2-C60)}∞. Color code: C, gray; P, orange; Ni, green; short interfullerene C-C distances are marked in red. 22 Reproduced with permission from ref21. Copyright Elsevier B. V. Appendix 1. 5
Figure 1.6: Fullerene-based supramolecular architecture. Reproduced with permission from ref21. Copyright Elsevier B. V. Appendix 1. 5
Figure 1.7: metal-organic hybrid architectures synthesized from AgPF6 and a) para-pyridylmalonic ester fullerene monoadduct to form b) discrete molecular units and c) polymers. Reproduced with permission from ref21. Copyright Elsevier B. V. Appendix 1. 7
Figure 1.8: a) Structure of *trans*-**1** *bis*-diazafluorene, **6**; red balls represent diethylmalonates. b) Single crystal X-Ray diffraction structure, purple atoms = Ag^+. Reproduced with permission from ref32. Copyright Royal Society of Chemistry. Appendix 2. 8
Figure 1.9: Fullerene *hexa*-adduct with four pyridyl groups. 8
Figure 1.10: a) Crystal structure of the linear polymer synthesized via slow diffusion of a solution containing $AgPF_6$ into a solution of the *trans*-**1** *hexa*-adduct containing pyridine groups. Color code: carbon atoms, gray ellipsoids; oxygen atoms, red ellipsoids; nitrogen atoms, blue ellipsoids; silver ions, violet ellipsoids. For clarity, the anions and solvate molecules are not shown. 9
Figure 1.11: Crystal structure of complex **8**. Color code: Hg, gray; O, red; N, blue; Cl, green... 10
Figure 1.12: Crystal structure of polymer **9**. The polymer is formed by weak Hg-fullerene interactions. Ethyl groups were omitted for clarity. Color code: C, gray; Hg, light gray; Cl, green; O, red. 11
Figure 1.13: Crystal structure of polymer **10.** Hydrogen atoms are omitted for clarity. Hg atoms are depicted in gray, Cl atoms in green and O atoms in red. 11
Figure 1.14: Crystal structure of polymer **11,** a zigzag polymer, where the Cd centers and fullerene cages are distributed in a zigzag arrangement**.** Hydrogen atoms are omitted for clarity. Color code: C, gray; O, red; Cd, yellow; N, blue. 12
Figure 1.15: Crystal structure of polymer **12,** a zigzag polymer, where the Zn centers interact with only one nitrogen in the daf group**.** Hydrogen atoms are omitted for clarity. Color code: C, gray; O, red; Zn, dark red; N, blue. 13
Figure 1.16: Crystal structure of polymer **13,** where Cu centers and the fullerene cages adopt a staircase configuration. Hydrogen atoms are omitted for clarity. Color code: C, gray; O, red; Cu, green; N, blue. 14

Figure 1.17: Crystal structure of polymer **14,** where Cu centers and the fullerene cages form a straight line. Hydrogen atoms are omitted for clarity. Color code: C, gray; O, red; Cu, green; N, blue..... 15
Figure 1.18: Crystal structure of polymer **15.** Color code: C, gray; O, red; Cu, green; Hg, light gray; N, blue..... 15
Figure 1.19: Thermo gravimetric analysis of compound **6** – black line; polymer **10** –red line; polymer **11** – green line; polymer **12** – purple line; polymer **13** – blue line. 16
Figure 1.20: UV-vis spectrum of compound **6** – black line; polymer **10** –red line; polymer **11** – green line; polymer **12** – purple line; polymer **13** – blue line; polymer **14** – orange line. Solvent: DMF 17
Figure 1.21: Computed 2D-MOF using tetra-daf as the linker and Cu(II) as the metal..... 19
Figure 1.22: Fullerenes *hexa*-adducts for the application in single molecule conductance..... 19
Figure 2.1: Structure of MOF-5. A) Assembly of the MOF by the reaction of terephthalic acid and Zn. B) Representation of the porosity of the framework. The yellow ball represents the empty space..... 24
Figure 2.2: Pictorical representation of the assembly of MOFs. Part 1 shows the assembly of a dicarboxylate fullerene derivative. Carboxylic acids are represented by the yellow balls. 2a) Shows the struts and their assembly into a 2b) 2D-layer in the presence of Zn. The 2D-layer can be transformed into a porous 3D-structure using 2c) bipyridine linkers as the pillars. The blue squares represent the pyridine groups. Both insets, a) and b) show the coordination of the Zinc atom represented by the blue pyramids. 26
Figure 2.3: 1a) $Li_8@C_{48}B_{12}$. 1b) Li-doped benzenedicarboxylate. c) 3-D organic framework constructed by 1a and 1b. 2a) $Ca_{32}C_{60}$. 2b) *p*-dihydroxybenzene. C) 2-D film constructed by 2a and 2b. Reproduced with permission from ref32..... 28
Figure 2.4: A C_{60}-impregnated MOF-177 structure. Copyright Royal Society of Chemistry. Appendix 3..... 29
Figure 2.5: Crystal structure of a 2D fullerene-based MOF. 30
Figure 2.6: Fullerene *hexakis*-adduct for the construction of MOFs. 30
Figure 2.7: Fullerene *hexakis*-adducts for the construction of MOFs. The malonate groups are represented with red balls. 31
Figure 2.8: Optimized geometries by DFT calculations of a) tetra-COOH porphyrin and b) compound 17. The arrows show the angles between the carboxylic acids which are located in a triangle. 32
Figure 2.9: Synthesis of MOF-1. The MOF structure was calculated using molecular mechanics. 32
Figure 2.10: Computed structure of MOF-2 using molecular mechanics. Color code: O, red; C, grey; N, blue..... 33
Figure 2.11: Computed structure of MOF-3 using molecular mechanics. Zinc atoms are shown in blue tetrahedrons. Color code: O, red; C, grey; N, blue. 33
Figure 2.12: Computed structure of MOF-4 using molecular mechanics. Zinc atoms are shown in blue tetrahedrons. Color code: O, red; C, grey; N, blue. 34
Figure 2.13: ATR-IR spectrum. Black line –yellow powder (MOF); red line-MOF after evacuation under vacuum; purple line – C_{60} tetramalonate; blue line – compound 16. 35
Figure 2.14: Synthetic scheme for MOF-4. 36
Figure 3.1: N,N'-di-*p*-anisylformamidinate (Danif). 45
Figure 3.2: Synthetic strategy for the assembly of different bimetallic Mo units. 46

Figure 3.3: Discrete molecular systems of fullerene derivatives with secondary building units. 47
Figure 3.4: Discrete molecular systems of fullerene derivatives with secondary building units. 47
Figure 3.5: ^{1}H-NMR of compound **29**. 48
Figure 3.6: MALDI-TOF spectrum of the reaction crude after 5 minutes, 1 hour and 2 hours. The calculated and experimental isotopic distributions for the products are shown on the bottom part of the figure. 49
Figure 3.7: UV-vis spectra of a) compound **28**, b) compound **27** and c) compound **29.** 50
Figure 3.8: Danif attack to the fullerene cage of the bimetallic complex. 50
Figure 3.9: Dimolibdenum-fullerene extended network. 51
Figure 4.1. Chemical structures of C60-monoadducts synthesized via 1,3-dipolar cycloaddition with terminal carboxylic acid and pyridine groups 54
Figure 4.2. **.** Syntheses of N-substituted glycines **34**-**37** through reactions of primary amines **31a** and **31b** with ethyl bromoacetate followed by the hydrolysis of compounds **32** or **33.** 55
Figure 4.3. Cyclic voltammogram of compound 28 in o-dichlorobenzene (0.05 M (n-Bu)4NPF6; scan rate 100 mV/s for CV) 57
Figure 4.4. Synthesis of N-substituted fulleropyrrolidines **28** and **30** through a 1,3-dipolar cycloaddition in the presence of paraformaldehyde. 58
Figure 4.5. Synthesis of N-substituted fulleropyrrolidines **28** and **30** through a 1,3-dipolar cycloaddition in the absence of paraformaldehyde 59
Figure 4.6. Comparison between the reaction yields for the synthesis of N-fulleropyrrolidines, compounds **1** and **2**. The blue bars represent the different methodologies for the synthesis of N-pyridine fulleropyrrolidine (**1**), the lighter bars show the yield when the reaction was done under standard conditions and the darker bars represent the yields when the reaction was done using N-pyridine imidinoacetic acid (**8**). The red bars represents the two different methodologies used for the synthesis of N-(4-carboxyphenyl)-fulleropyrrolidine (**2**), the lighter bars show the yield of the reaction when it was done using the N-(4-carboxyphenyl)-glycine (**7**) and paraformaldehyde. The darker red bars represent the yield of the reaction when it was done using N-(4-carboxyphenyl)-imidinoacetic acid (**9**) as the starting material. 62
Figure 4.7: Synthesis of N-substituted fulleropyrrolidines **28** and **30** through a 1,3-dipolar cycloaddition in the absence of paraformaldehyde 63
Figure 4.8: Synthesis of 4-(4-carboxyphenyl)-morpholine-2,6-dione under reflux in the presence and absence of paraformaldehyde 64
Figure 5.1. Endometallofullerenes. a) $La@C_{82}$-C_{2v} b)$La_2@C_{100}$ c)$Sc_2@C_{82}$ d)$M_3N@C_{80}$ 68
Figure 5.2: HPLC profile of the CS_2 extract containing lutetium EMFs. The top HPLC profile is an expansion of the chromatograms shown in the bottom of the figure. The experiment was done using a 5PBB column, with a flow rate of 5mL/min using toluene as the eluent. 70
Figure 5.3: HPLC profile of the largest fraction collected from the first step separation. The experiment was done using a Buckyprep column, with a flow rate of 5mL/min using toluene as the eluent. 71
Figure 5.4: a) MALDI-TOF spectrum of Lu2C82. b) Recycling HPLC chromatogram of Lu2C82. The experiment was done using a Buckyprep column, with a flow rate of 1.4 mL/min using toluene as the eluent. 71
Figure 5.5: UV spectrum of Lu_2C_{82} in CS_2. 73
Figure 5.6. Cyclic voltammogram of Lu2C82 in o-dichlorobenzene (0.05 M (n-Bu)4NPF6; scan rate 100 mV/s for CV). 74

Figure 6.1: Reaction of 39 with Ru3(CO)12. The ethyl formate groups (COOC2H5) are denoted by green balls and the Ru(CO)3 groups are denoted by blue balls. 77
Figure 6.2: (a) 1H NMR spectrum of **40** (600 MHz, $CDCl_3$) and expanded parts: (b) 4.60–4.05 ppm, (c) 1.50–1.15 ppm 78
Figure 6.3: (a) Front and (b) side views of the **40** configuration. The ethyl formate groups ($COOC_2H_5$) are denoted by Green balls and the $Ru(CO)_3$ groups are denoted by blue balls. 78
Figure 6.4: HPLC profile shows the first and second cycles in the purification. (Cosmosil Buckyprep column (20 mm x 250 mm), toluene as eluent and flow rate is 1mL/min. 79
Figure 6.5: (a) ^{1}H-NMR spectrum of mixture *parallel*-3–*tilted*-3 (600 MHz, $CDCl_3$) and expanded parts: (b) 4.45–4.10 ppm, (c) 1.45–1.15 ppm. 80
Figure 6.5: Expanded regio of the ^{1}H-NMR spectrum of the mixture *parallel*-3/*tilted*-3 (600 MHz, $CDCl_3$) at -20C 80
Figure 6.6: (a) Front and (b) side views of the *tilted*-3 isomer. The ethyl formate groups ($COOC_2H_5$) are denoted by green balls and the $Ru(CO)_3$ groups are denoted by blue balls. 81
Figure 6.7: (a) Front and (b) side views of the *parallel*-3 isomer. The ethyl formate groups ($COOC_2H_5$) are denoted by green balls and the $Ru(CO)_3$ groups are denoted by blue balls. 81
Figure 6.8: ^{13}C-NMR spectrum of mixture *parallel*-3/*tilted*-3. 82
Figure 6.9: A drawing of **39** with 30% thermal ellipsoids and only the methano carbon atoms of the di(ethoxycarbonyl)methano addends shown as black ellipsoids 83
Figure 6.10: van't Hoff plot for the *tilted*-3 ↔ *parallel*-3 interconversion 87

Chapter 1: [60] Fullerene Based Supramolecular Architectures

1.1 Introduction

In this chapter we explain the general synthetic strategy we used for the regioselective functionalization of different fullerene derivatives. Additionally, we report the synthesis of different fullerene-based metallopolymers.

1.1.1 Derivatization of C_{60}

In the last years fullerene derivatives have been reported and their potential applications as electronic, magnetic, catalytic, biological and optical materials have been explored.[1-5] In this chapter we describe the design and synthesis of fullerene based supramolecular architectures. The functionalization of C_{60} is a well-established field that began in 1990, as soon as macroscopic quantities of the fullerenes became available.[6] The regio-selective addition of multiple groups to the C_{60} cage is challenging as its framework has 30 equivalent reactive double bonds in [6,6] ring junctions.[7] After the addition of one group, successive additions of one, two, and three identical and symmetrical addends yield 8, 46, and 262 possible isomers, respectively.[8] After eight regioisomers of (ethoxycarbonyl)methylene-C_{60} *bis*-adducts were isolated and characterized, a general nomenclature for the different *bis*-adducts was established (Figure 1.1).[9] C_{60} is divided into two hemispheres; if the two addends are in the same hemisphere they are in a *cis* position relative to each other and if the two addends are in opposite hemispheres they are in a *trans* position relative to each other.

irent a car el paso

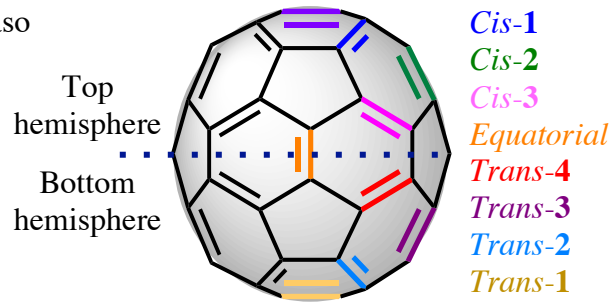

Figure 1.1: Hirsch nomenclature for the eight regioisomers (depicted in different colors) for C60 bis-adducts with respect to the first addition (purple bond).

In figure 1.1 the first addition goes to the purple double bond. If the second addition goes to the green bond, a *cis*-**2** isomer is formed; similarly, if the second addition goes to the blue bond a *trans*-**2** isomer is formed.

Multiple strategies can be and have been used to add different groups, especially while controlling the regiochemistry when more than one addend is attached. Probably the best known method to do this is the so-called "tether-directed-remote-functionalization," first introduced in 1994 and elegantly developed by Diedrich et al.[10-13] Another method for the regioselective synthesis of several C_{60} derivatives was introduced by Kräutler et al in 1996 and designated "orthogonal transposition", which is based on the exclusive formation of a *trans*-**1** bis-anthracene derivative when C_{60} is reacted with anthracene in the solid phase, see compound **3** in figure 1.2.[14-16]

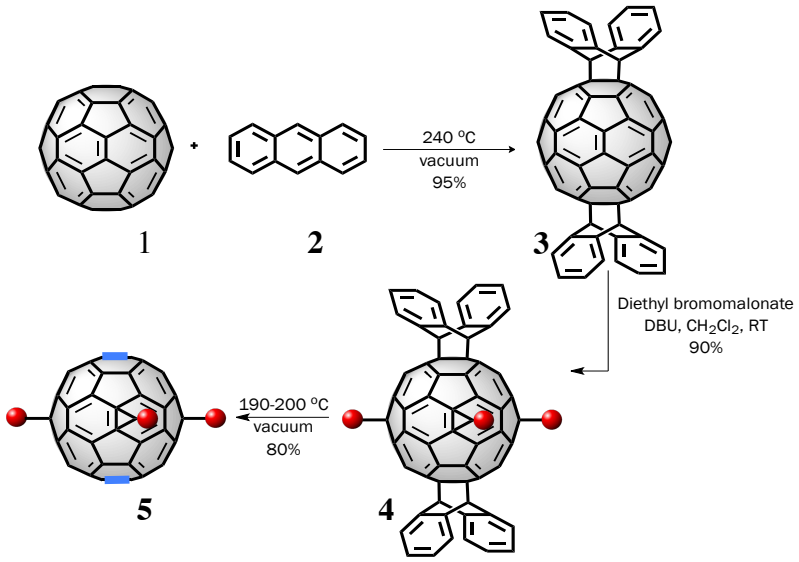

Figure 1.2: Orthogonal transposition method. Malonates are designated with red balls representing $-C(CO_2Et)_2$ groups.

Compound **3** reacts with diethyl bromomalonate to form an *hexa*-adduct with four malonates located in the equatorial belt, **4**. The all equatorial tetramalonate, **5**, is formed by heating compound **4** under vacuum. Using compound **5** as the precursor, we synthesized a

variety of fullerene derivatives with functional groups in a *trans*-**1** orientation relative to each other, as shown in figure 1.2 (compound **5**, blue bonds). We used the fullerene *hexa*-adducts to construct supramolecular architectures with different potential applications. Additionally, the *hexa*-adducts were tested in single molecule conductance measurements. In this chapter we describe the synthesis and characterization of different fullerene based metallopolymers using the *hexa*-adduct **6** as the building unit.

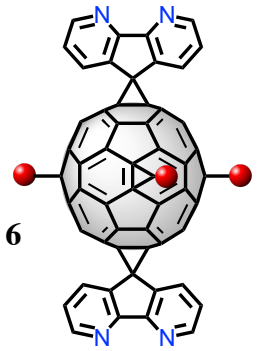

6

Figure 1.3: *Hexa*-adduct with two 4,5-diazofluorene groups in *trans*-**1** position relative to each other. As in figure 1.2, the malonate groups are represented with red balls.

1.1.2 Fullerene based metallopolymers

Fullerenes constitute an interesting family of materials due to their unique electronic and chemical properties. The poor yields of regioselectively functionalized fullerenes limits their use in the construction of supramolecular architectures with potential applications in materials science. On the other hand, the functionalization of the spherical fullerene cage gives easy access to a great variety of derivatives possessing molecular geometries which are generally not accessible for common small organic building blocks.[17] These geometries and the higher degrees of functionality might enhance both the scope and diversity of metal-organic hybrid architectures such as polymers and metal-organic frameworks (MOFs). We discuss the design and synthesis of fullerene-based MOFs in chapter 2.

Several strategies have been explored to build fullerene-based metallopolymers. The first reports on metal-organic hybrid architectures explored the ability of pristine fullerenes to easily react with transition metals. Hence, as a product of the reaction between C_{60} and transition

metals, different composite materials were synthesized: Pd_nC_{60}[18], Ru_3C_{60}[19] and Pt_nC_{60}[20]. The reported composites lacked cristallinity and only their stoichometries were known. To extend the scope of metal-fullerene architectures, different complexes were reported where two fullerene cages were connected through a metal complex that directly interacted with the carbon cage. Figure 1.4 shows the first example of two fullerenes complexed by a single metal center,[21] a dimeric complex $\{Rh_6(CO)_5(dppm)_2(CNR)\}\{\mu_3\text{-}\eta^2, \eta^2, \eta^2\text{-}\{(C_{60})_2\}\}$ ($R=CH_2C_6H_5$, dppm=bis(diphenylphosphino)methane).[17] For this complex, cyclic voltammetry studies revealed strong electronic coupling between the two C_{60} molecules.

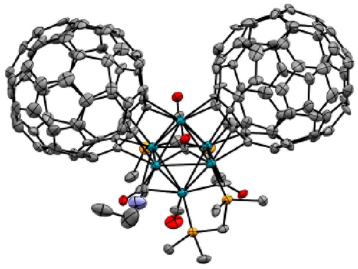

Figure 1.4: Crystal structure of the first fullerene-metal sandwich complex {Rh6(CO)5(dppm)2(CNR)}{μ3-η2, η2, η2-{(C60)2}}. Reproduced with permission from ref21. Copyright Elsevier B. V. Appendix 1.

Additionally, by direct interaction of fullerene cages with Ni atoms a 1-D polymer was formed and its structure was elucidated by single crystal X-ray diffraction. The polymer is shown in figure 1.5, every Ni atom is tetrahedrally coordinated to two fullerene units via a η^2-bonding motif involving the fullerene [6,6] double bonds.

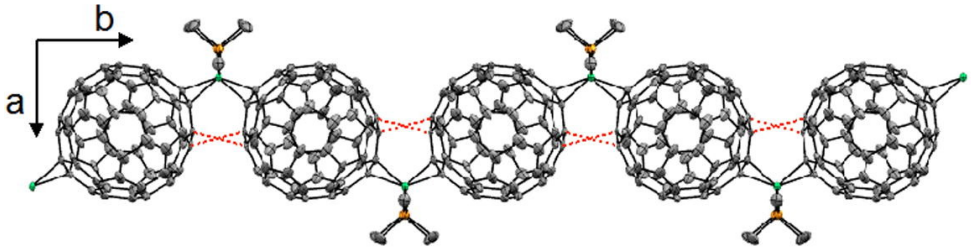

Figure 1.5: Representation of metal-organic polymer {Ni(Me3P)2](μ-η2,η2-C60)}∞. Color code: C, gray; P, orange; Ni, green; short interfullerene C-C distances are marked in red. 22 Reproduced with permission from ref21. Copyright Elsevier B. V. Appendix 1.

Not only the interaction between pristine fullerenes and metals has been studied, there are also different reports on the interaction between exohedral functionalized fullerenes and metals. The first reported supramolecular architecture based on a C_{60} was a fullerene-containing dimer assembled by the coordination of a bi-pyridyl fullerene derivative and two Pt(II) centers, see figure 1.6.[23]

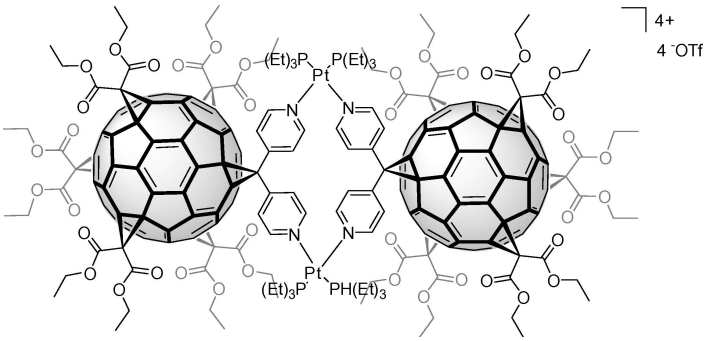

Figure 1.6: Fullerene-based supramolecular architecture. Reproduced with permission from ref21. Copyright Elsevier B. V. Appendix 1.

Although different attempts have been made to incorporate fullerenes into extended networks, in most cases only discrete molecular systems have been obtained.[24-29] The successful incorporation of fullerenes in discrete molecular assemblies shows the potential application of fullerene ligands in metal-organic assemblies. To further explore the use of fullerene derivatives in this type of architectures, different strategies to synthesize building blocks containing multiple binding sites have been implemented. The first one involved the incorporation of more than one binding site into a fullerene moiety.[29] Nierengarten and coworkers found that for *mono*-adducts bearing two reactive sites, competition between dimerization and polymerization would dictate the formation of either discrete assemblies or linear polymers.[17] Similarly, it was found that in the case of a bispyridyl monoadduct (figure 1.7a) the coordination topology could be switched

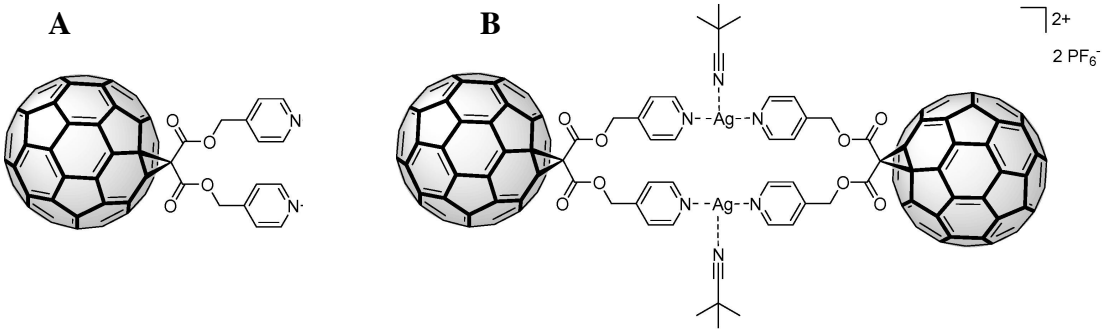

fro m dim er (figur e 1.7b) to polymer (Figure 1.7c) by changing the crystallization conditions. [17, 24]

C

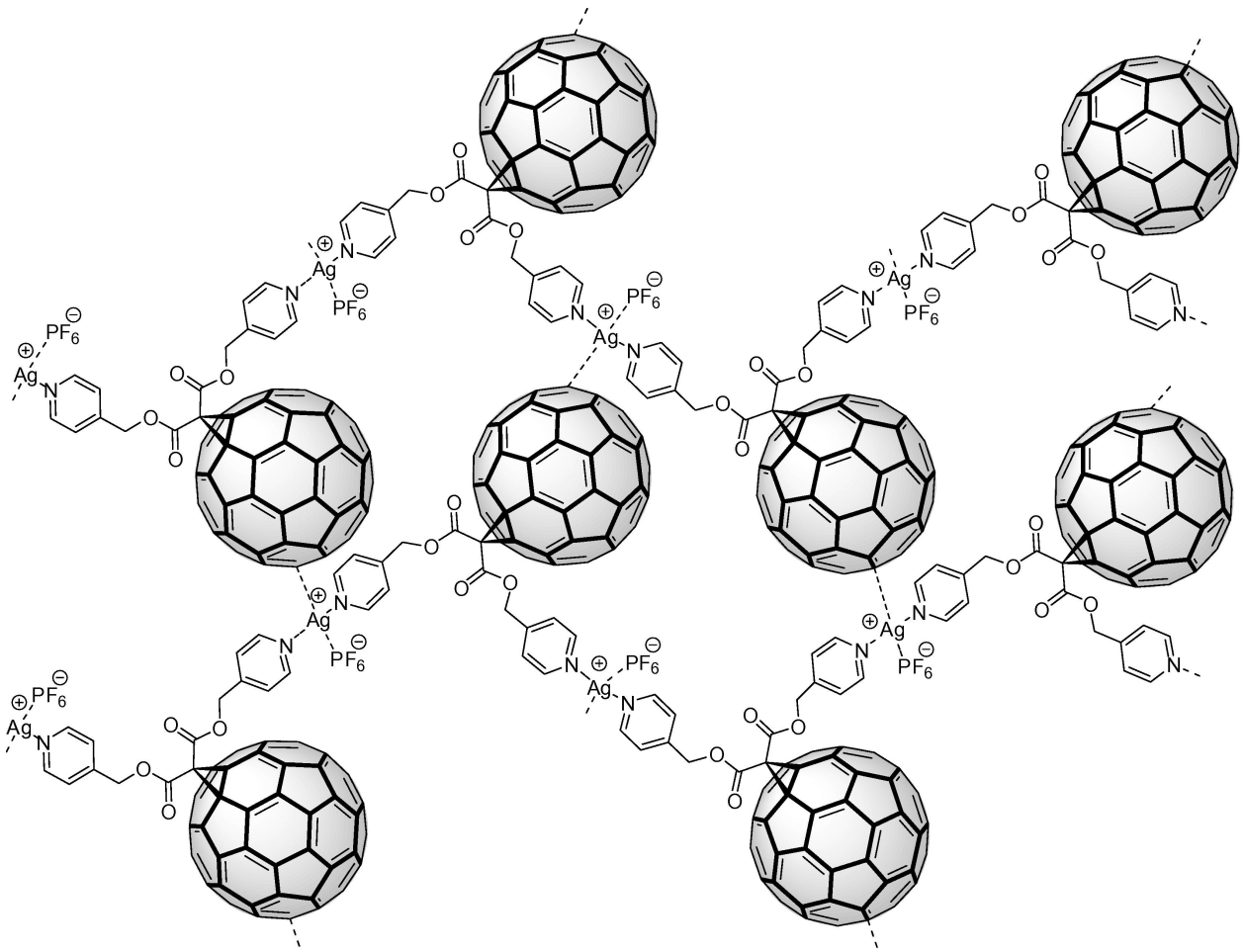

Figure 1.7: metal-organic hybrid architectures synthesized from AgPF6 and a) para-pyridylmalonic ester fullerene monoadduct to form b) discrete molecular units and c) polymers. Reproduced with permission from ref21. Copyright Elsevier B. V. Appendix 1.

As a next step towards the goal of fullerene-based extended networks, the bispyridyl monoadduct (figure 1.7 a) was elongated to favor polymerization instead of dimerization. However, the complexation of the elongated fullerene derivative with Cu did not result in any fullerene-fullerene interconnection, instead an *endo*-complex was formed.[25] In order to favor the polymeric chain growth, different fullerene derivatives with rigid reactive groups were designed. Balch and coworker designed and synthesized a piperazine fullerene *mono*-adduct, $[C_{60}(N(CH_2CH_2)_2N)]$, in which the addend exhibited a precise spatial separation between the two amino groups. The piperazine fullerene *mono*-adduct was successfully incorporated in different polymeric chains using Ag and Rh as the complexation metals.[30-31]

One of the advantages of C_{60} for the synthesis of extended networks is the distribution of different reactive sites on the fullerene cage. Therefore, it is very appealing to use the different regioisomers of C_{60} to design molecules with different binding motifs in a certain orientation. Using the orthogonal transposition method, Ping et al reported the synthesis of a fullerene derivative with two 4,5-diazofluorene (daf) ligands with a linear *trans*-**1** arrangement in a very high yield (91%). The resulting *hexa*-adduct (figure 1.8a) was assembled into a 1D- polymer using silver as the coordination metal (figure 1.8b).[32] Surprisingly, the resulting 1-D polymer with Ag(I) did not exhibit the expected tetrahedrally-linked bis daf motifs from adjacent fullerene compounds, instead the coordinated daf-Ag(I) units directly interacted with a neighboring cage via de Ag(I) ions.

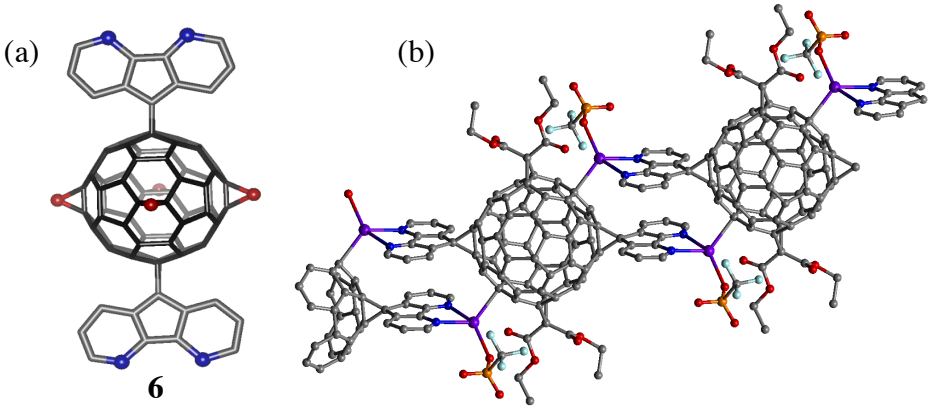

6

Figure 1.8: a) Structure of *trans*-**1** *bis*-diazafluorene, **6**; red balls represent diethylmalonates. b) Single crystal X-Ray diffraction structure, purple atoms = Ag^+. Reproduced with permission from ref32. Copyright Royal Society of Chemistry. Appendix 2.

Using the *orthogonal transposition* method, our group was able to synthesize an *hexakis*-adduct (figure 1.9, **7**) in good yields. Compound **7** reacted with $AgPF_6$ to yield a one-dimensional metal-organic polymer (Figure 1.10). The crystal structure revealed argentophilic interactions between the two Ag^+ ions, as well as π-π interactions between the pyridyl groups in neighboring struts.[33]

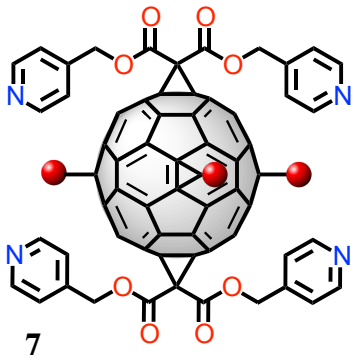

Figure 1.9: Fullerene *hexa*-adduct with four pyridyl groups.

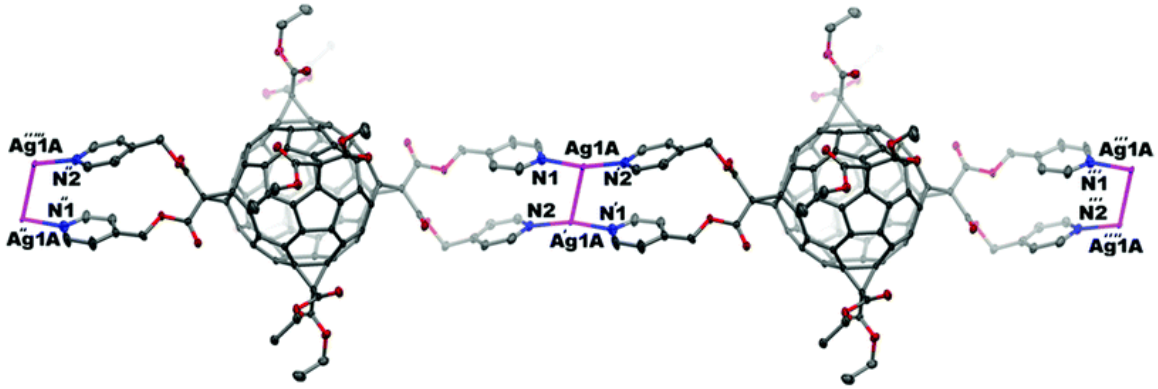

Figure 1.10: a) Crystal structure of the linear polymer synthesized via slow diffusion of a solution containing $AgPF_6$ into a solution of the *trans*-**1** *hexa*-adduct containing pyridine groups. Color code: carbon atoms, gray ellipsoids; oxygen atoms, red ellipsoids; nitrogen atoms, blue ellipsoids; silver ions, violet ellipsoids. For clarity, the anions and solvate molecules are not shown.

Although there are several reports of fullerene based 1D coordination polymers, the control of the polymer shape remains a challenge in order to build more complex supramolecular structures. It has been shown that the crystallization method favors either the polymerization or dimerization of fullerene derivatives; however, the effects of the solvent, the metal and metal ratio are not clear. Additionally, we hypothesized that the incorporation of different metals into a polymeric chain would not only affect its structural properties but also its stability and optoelectronic properties. In this work we explored the effect of the metal and metal ratio on the coordination geometry of compound **6** and we studied the changes in the stability and optoelectronic properties of the resulting polymeric chains.

1.2 Results And Discussion

Daf has been widely studied as a dinitrogen chelating ligand, which exhibits exceptional affinity for metal ion coordination.[34-35] The orientation of the daf addends in **6** is designed for the construction of linear polymeric structures upon complexation with suitable tetrahedral geometry metals. It can also serve as a building block for the formation of 2D and 3D networks. As mentioned before, compound **6** did not yield a perfectly linear polymer in the presence of Ag(I). As a consequence, we decided to try Cu(I) because it is well known to form tetrahedral complexes with bipyridyl ligands. However, stable single crystals were not obtained when **6** was reacted with $CuBr(CH_3)_2S$ or $Cu(CH_3CN)_4PF_6$.

Complexation of **6** with $HgCl_2$ led to a bimetallic molecular product (**8**, figure 1.11), where each daf unit coordinates with one $HgCl_2$. Toluene is included in the crystals of the compound and we were able to locate four molecules of solvent per complex molecule. The malonate ethyl groups were solved as isotropic due to the disorder observed. The crystal structure of complex **8** reveals the formation of polymer **9**.

Closer examination of the structure of **9** in figure 1.12 reveals a resemblance to the Ag polymer reported previously, since Hg exhibits an interaction with the fullerene moiety in a η^4 fashion, generating a coordination polymer in the direction of the crystallographic *c* axis. The dafs on the crystallographic structure are stacked with an interplanar distance of 3.469 Å and a shift of 4.909 Å from the centroid. Different secondary interactions are observed in the crystal structure: the Cl atoms form hydrogen bonds with the ester groups and the oxygen of the ester group interacts with the carbons of the neighboring cage in the direction of the crystallographic axis *a*.

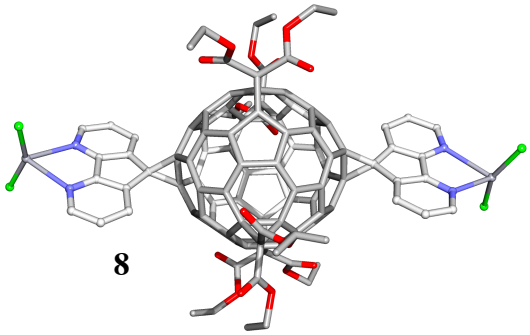

Figure 1.11: Crystal structure of complex **8**. Color code: Hg, gray; O, red; N, blue; Cl, green.

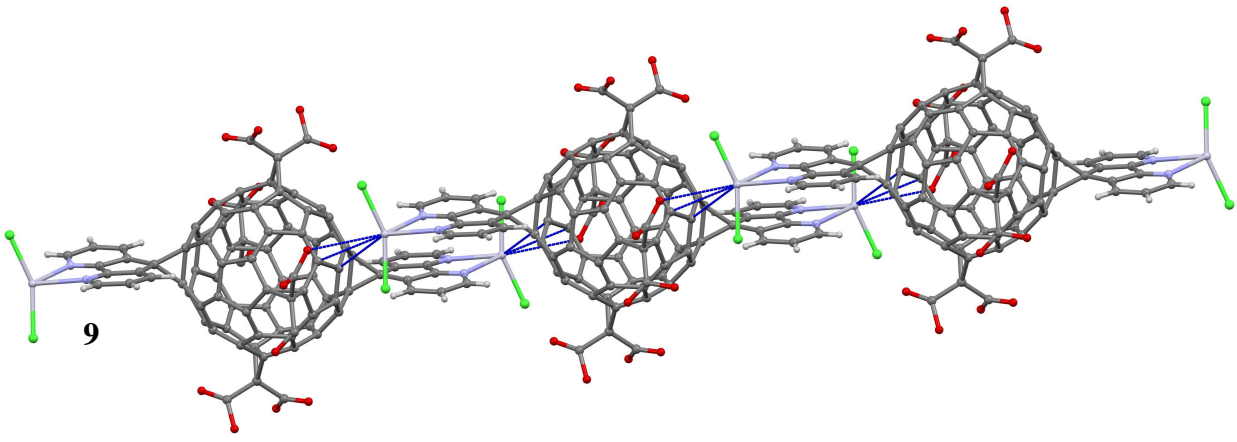

Figure 1.12: Crystal structure of polymer **9**. The polymer is formed by weak Hg-fullerene interactions. Ethyl groups were omitted for clarity. Color code: C, gray; Hg, light gray; Cl, green; O, red.

In polymer **9**, the ratio of compound **6** to Hg was 1:2. To establish the effect of the metal ratio on the configuration of the polymer, we used a ratio of compound **6** to $HgCl_2$ of 1:1 instead of 1:2. Light yellow crystals (figure 1.13) were obtained by slow diffusion of $HgCl_2$ in ethanol into a solution of compound **6** in chloroform followed by the addition of tetrachloroethane. In the crystal structure of polymer **10**, the fullerene cages were connected by coordination of Hg with the daf groups in an octahedral geometry and thus formed a zigzag linear polymer. It is noteworthy that the Cl-Hg-Cl angle is 111°, which is much less than that of polymer **9** (151°). As the results show, not only the central metal but also the ratio of fullerene derivative to metal plays an important role in the structure of the resulting 1D polymer.

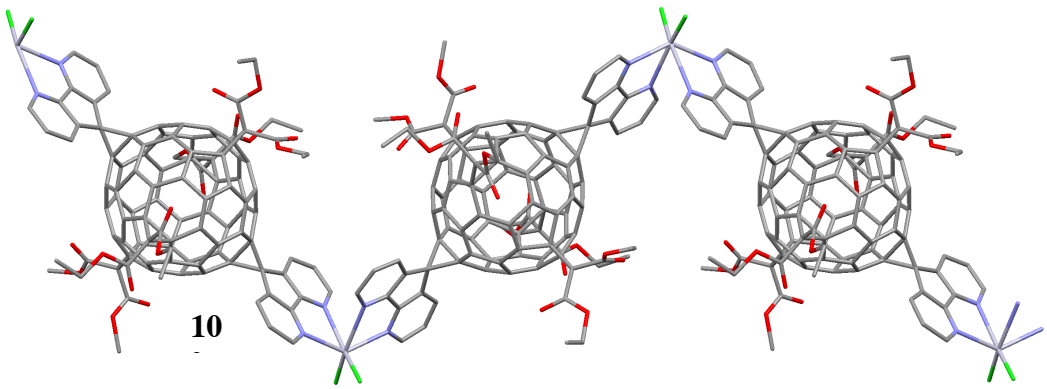

Figure 1.13: Crystal structure of polymer **10.** Hydrogen atoms are omitted for clarity. Hg atoms are depicted in gray, Cl atoms in green and O atoms in red.

Yellow crystals were obtained by slow diffusion of $Cd(NO_3)_2$ in methanol into a solution of compound **6** in chloroform, followed by the addition of toluene. The structure shows a zigzag polymer (**11**, figure 1.14). The center-to-center distance between adjacent cages along the polymer is 15.415 Å. This distance results from the octahedral geometry exhibited by Cd in which the bite angle cage-Cd-cage is 96.67°. No direct interactions between the linear polymers were observed in the crystal structure.

Zn also has the ability to form coordination complexes with 4,5-diazafluorene.[34-35] Yellow crystals of a 1D polymer (figure 1.15, **12**) were obtained by slow diffusion of $ZnBr_2$ in ethanol into a solution of compound **6** in chloroform followed by the addition of benzene. The Zn atom coordinated with four N atoms from daf units and Br atoms in a distorted octahedral geometry with the bite angle for Br-Zn-Br of103.04°. Two Zn-N bond lengths are 2.086 Å and the other two Zn-N distances are 2.591 Å. It is noteworthy that in all other polymers we obtained the metal coordinated with both of the nitrogen atoms except polymer **12**, in which the Zn atoms coordinate with only one nitrogen. The center-to-center distance between adjacent fullerene cages is 17.048 Å, which is longer than in polymer **11** (14.415 Å).

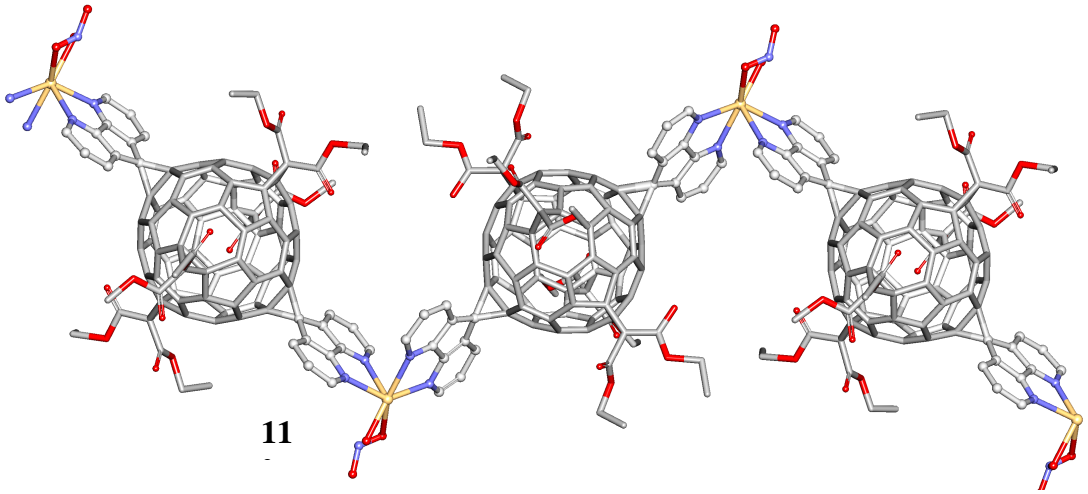

Figure 1.14: Crystal structure of polymer **11,** a zigzag polymer, where the Cd centers and fullerene cages are distributed in a zigzag arrangement**.** Hydrogen atoms are omitted for clarity. Color code: C, gray; O, red; Cd, yellow; N, blue.

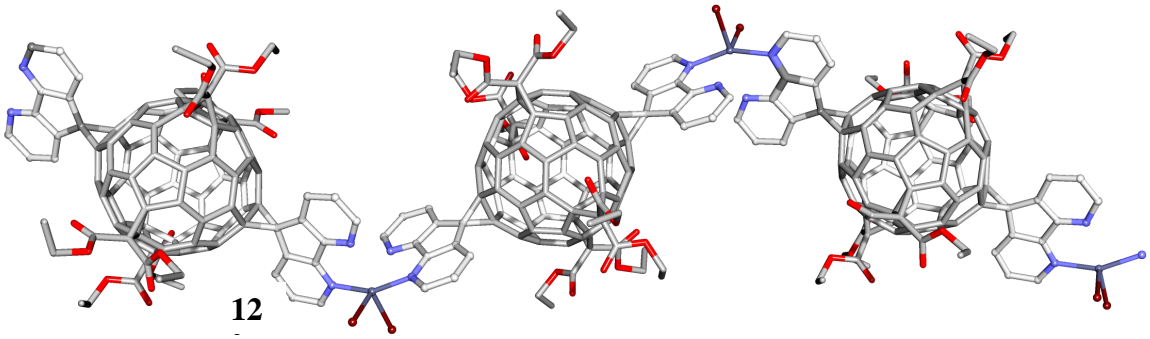

Figure 1.15: Crystal structure of polymer **12,** a zigzag polymer, where the Zn centers interact with only one nitrogen in the daf group**.** Hydrogen atoms are omitted for clarity. Color code: C, gray; O, red; Zn, dark red; N, blue.

Cu(II) can coordinate with two 4,5-diazafluorene-9-one and form an octahedral complex with the four nitrogen atoms located in a plane. Consequently, we also studied the coordination of Cu(II) with compound **6**. Green crystals of polymer **13** (figure 1.16) were obtained by slow diffusion of $CuCl_2$ in methanol into a solution of compound **6** in chloroform. Polymer **13** is a staircase linear polymer. The crystal structure shows a parallelogram consisting of two Cu and two Cl atoms. The Cu-Cl bonds are 2.273 and 2.671 Å in the parallelogram, and 2.233 Å outside. The distance between the adjacent cages is 20.931 Å, which is longer than for the zigzag polymers **11** and **12**.

Compared with polymers **11** and **12**, polymer **13** has a different stoichiometry as the ratio of metal to fullerene is 2:1 instead of 1:1. By changing the ratio of $CuCl_2$ to compound **6** to 1:1, we finally observed a perfectly linear polymer (**14**, figure 1.17). Yellow crystals of this polymer were obtained by slow diffusion of $CuCl_2$ in methanol into a solution of compound **6** in chloroform followed by the addition of benzene. The Cu atom coordinates with the four nitrogen atoms from the 4,5-diazafluorene and two Cl atoms in an octahedral geometry. The two Cu-N bonds are 1.997 and 2.609 Å due to a Jahn-Teller distortion. Additionally, adjacent linear polymers interact through hydrogen bonding between the malonate ester oxygen and the hydrogen from the ethyl group. The distance between adjacent fullerene cages along the polymer chain is 20.219 Å, which is slightly shorter than that of polymer **13**. Although polymer **13** and **14** correspond to Cu complexes, they have totally different structures.

We also studied the reaction between $CuCl_2$ and complex **8** (figure 1.11) with the aim to replace Hg with Cu and connect compound **6** to form a linear polymer. Surprisingly, a hetero tetra-metallic staircase polymer (**15**, figure 1.18) was obtained. To the best of our knowledge, it is the first example of a hetero-metallic fullerene polymer. Crystals of polymer **15** were formed

by slow diffusion of $CuCl_2$ in methanol to a solution of complex **8** in chloroform. The crystal structure shows the same main chain as polymer **13**. The Hg atoms were replaced by Cu to coordinate with nitrogen atoms of the fluorene. However, the Hg atoms were still connected to the polymer chain by sharing two Cl atoms with Cu. Compared with polymer **13**, the Cu-Cl bond lengths inside the central parallelogram are 2.271 and 2.743 Å, respectively. The distance between adjacent cages is 21.387 Å, which is a little longer than that of polymer **13** showing that the presence of Hg extended the length of the Cu-Cl bonds. Adjacent linear strands were connected by chloroform between the Cl atoms coordinated with Hg and the adjacent malonate carbonyl oxygen atoms.

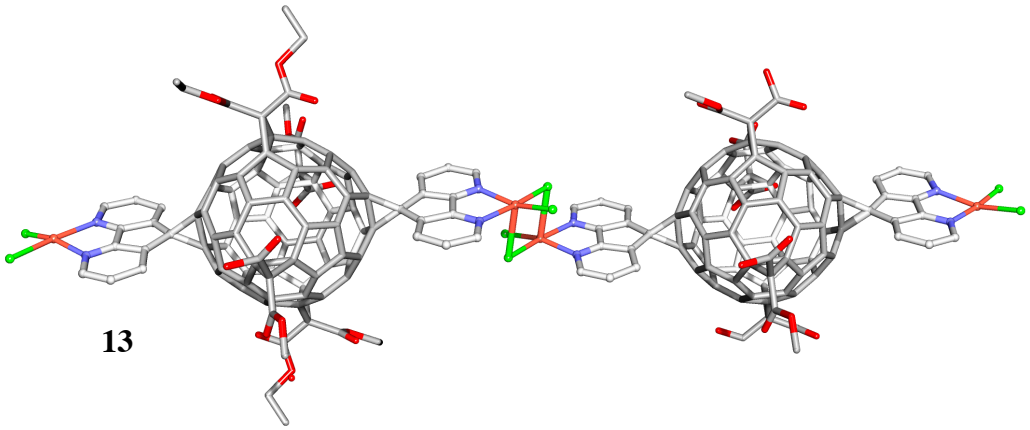

Figure 1.16: Crystal structure of polymer **13,** where Cu centers and the fullerene cages adopt a staircase configuration. Hydrogen atoms are omitted for clarity. Color code: C, gray; O, red; Cu, green; N, blue.

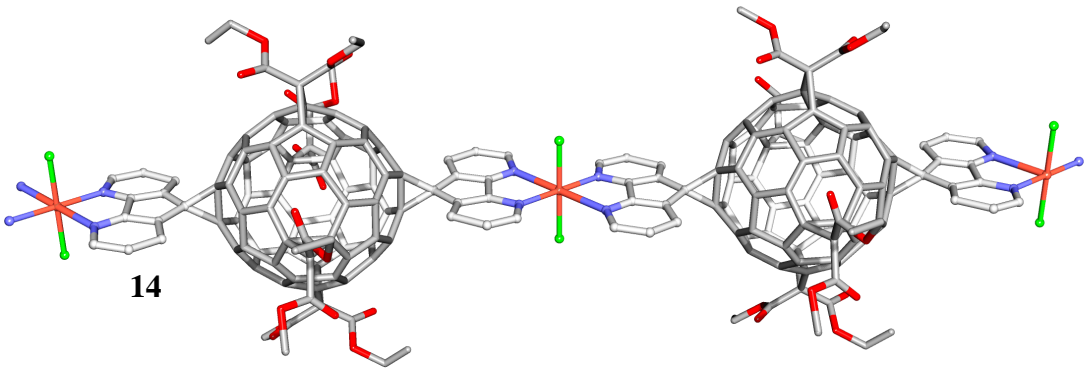

Figure 1.17: Crystal structure of polymer **14,** where Cu centers and the fullerene cages form a straight line. Hydrogen atoms are omitted for clarity. Color code: C, gray; O, red; Cu, green; N, blue.

The distances between adjacent fullerene cages in each of the polymers are listed in table 1. The pseudo polymer **9** has the shortest distance between fullerene cages at 15.225 Å. For zigzag polymers **11** and **12**, the distance is mainly determined by the cage-metal-cage angle. For linear polymers **13**, **14** and **15**, the distance is mainly determined by the coordination of the central metal. Polymer **14** exhibits the shortest distance as it has a single Cu center connecting

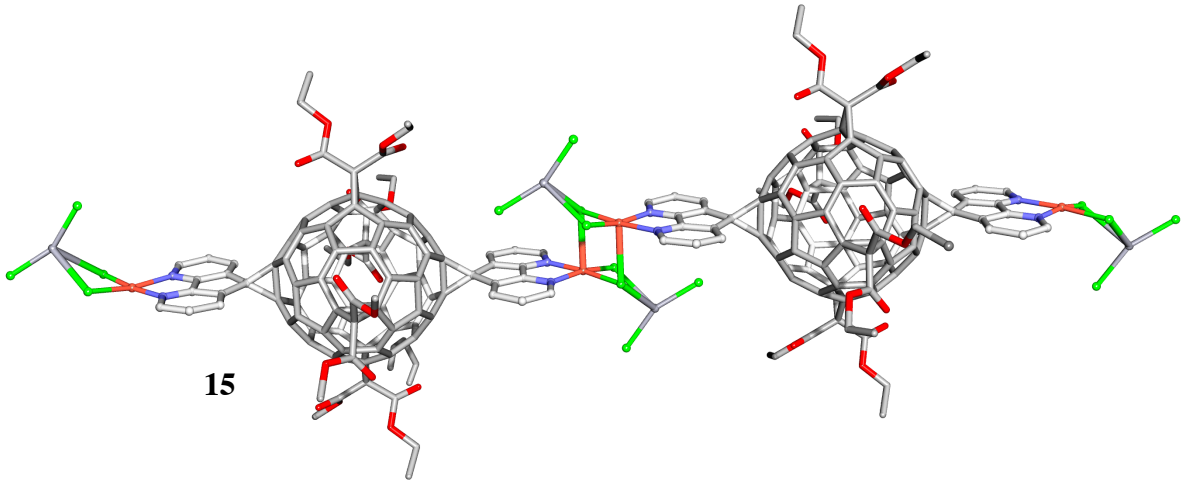

the fullerenes. Polymer **13** is slightly longer since the cages are connected by two Cu atoms. For polymer **15**, the presence of Hg extended the Cu-Cl bond and resulted in the longest fullerene intercage distance of all of the polymers.

Figure 1.18: Crystal structure of polymer **15.** Color code: C, gray; O, red; Cu, green; Hg, light gray; N, blue.

Table 1.1: Distances between cages and cage-metal-cage angles in the different polymers,

	Polymers						
	9	10	11	12	13	14	15
Cage Distance (A)	15.225	15.118	15.415	17.048	20.931	20.219	21.387
Cage-metal-cage angle	-	-	96.67	114.64	-	-	-

We synthesized polymers **10-14** using a different crystallization methodology to increase the stability of the polymers and analyze their opto-electronic properties. We found out that the crystal structure was more stable when either benzene or toluene were used for the crystallization instead of tetrachloroethane; the benzene ring interacts with the fullerene cages and stabilize the crystal structure.

Figure 1.19 shows the thermogravimmetric analysis (TGA) of compound **6** (black line) and polymers **10-14.** Compound **6** starts decomposing around 100°C with the loss of a daf group. When compound **6** was used to form polymeric chains, the polymeric structures started decomposing at 280 °C. Polymer **10** is the most stable polymer suggesting that the interaction between the daf and the metal in the daf-mercury complex is stronger. Our results show that the synthesized metallopolymers are suitable for applications that required high temperatures for the synthesis of materials.

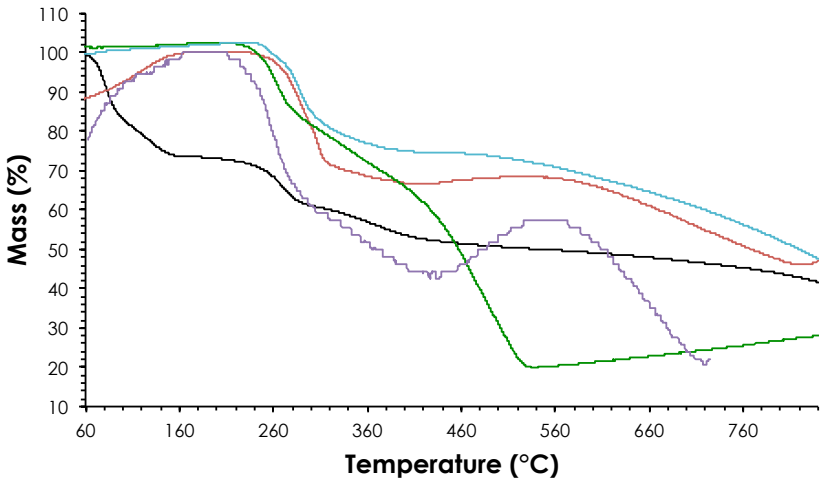

Figure 1.19: Thermo gravimetric analysis of compound **6** – black line; polymer **10** –red line; polymer **11** – green line; polymer **12** – purple line; polymer **13** – blue line.

Figure 1.20 shows the UV-vis spectra of compound **6** and polymers **10 – 14**. As figure 1.20 shows, the absorption varies with the identity of the metal and its configuration. Polymer **13**

is the only structure that exhibits a charge transfer (CT) band in the visible region as inset a shows. All the polymers exhibit a low-energy electronic transition around 1000 nm (inset c, figure 1.20), however, the intensity depends on the metal. The complex between daf and mercury exhibits the most intense low-energy electronic transition.

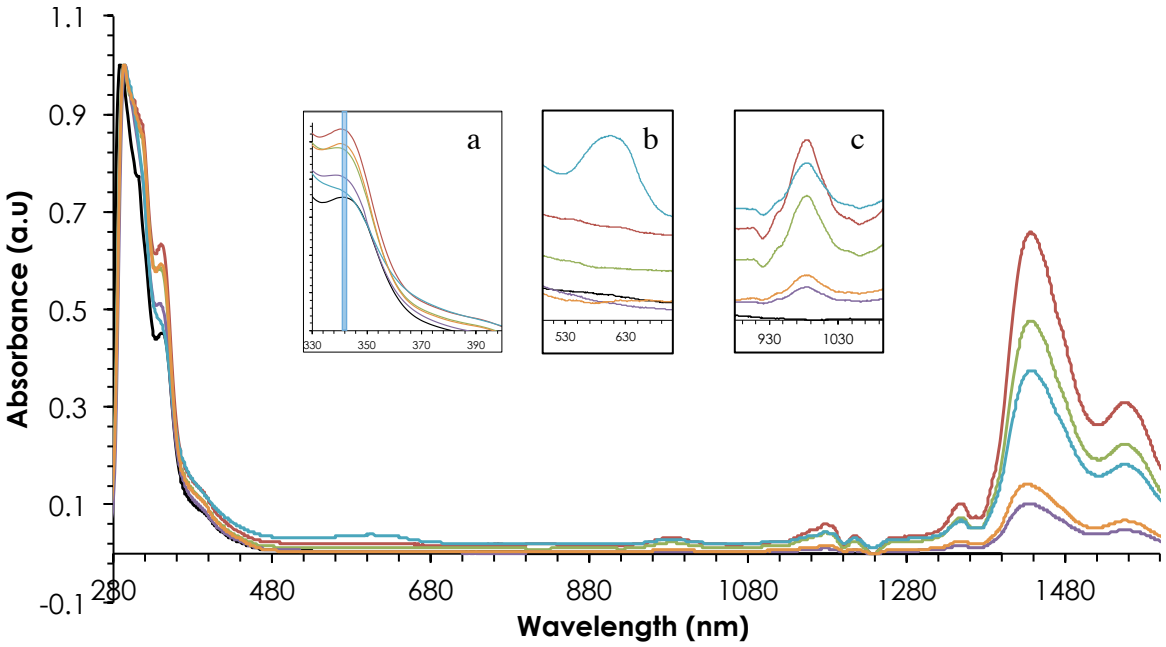

Figure 1.20: UV-vis spectrum of compound **6** – black line; polymer **10** –red line; polymer **11** – green line; polymer **12** – purple line; polymer **13** – blue line; polymer **14** – orange line. Solvent: DMF

1.3 CONLUSIONS

In summary, we synthesized fullerene linear polymers with a variety of staircase linear polymers, zigzag linear polymers and a perfectly linear polymer using a *hexakis*-fullerene adduct with two 4,5-diazafluorene groups located at *trans*-**1** positions and Hg, Cd, Zn or Cu as the metal centers. By selecting different metals and adjusting the stoichiometry between the fullerene derivative and the metals, different polymer structures were constructed. These results

encouraged us to investigate fullerene derivatives with similar ligand groups to form supramolecular structures, such as Metal Organic Frameworks (MOFs -see chapter 2), which might have potential usage in gas storage or organic molecule adsorption. Additionally, our results show that the polymeric chains are thermally stable and their opto-electronic properties can be tuned depending on the metal and on the metal to fullerene derivative ratio.

1.4 Future Work

The coordination chemistry of compound **6** should continue to be explored. Discrete molecular systems as the ones described in chapter 4 can be constructed using Ru dimetallic units. Additionally, an all equatorial daf-fullerene derivative can be synthesized using the "orthogonal transposition method" and try its complexation with Cu(II) to form a 2D-MOF as shown in figure 1.21. Similarly, an all *hexa*-daf fullerene derivative can be used to construct a 3D-MOF using an octahedral metal as Ru. Furthermore, we are exploring the application of compound **6**, together with the fullerene derivatives shown in figure 1.22, in single molecule conductance.

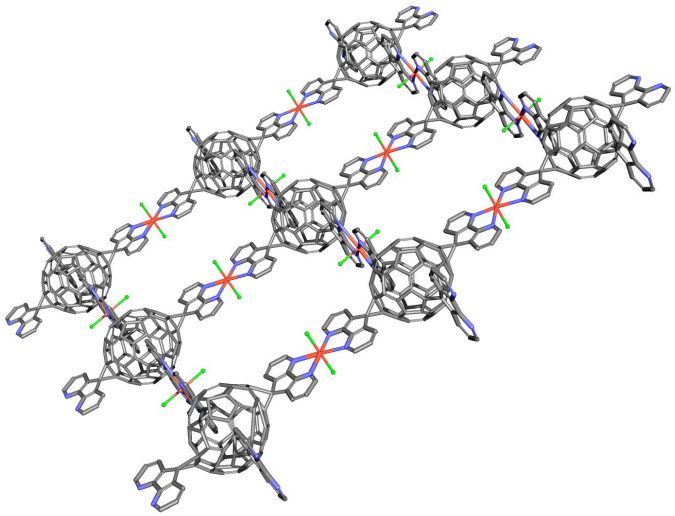

Figure 1.21: Computed 2D-MOF using tetra-daf as the linker and Cu(II) as the metal.

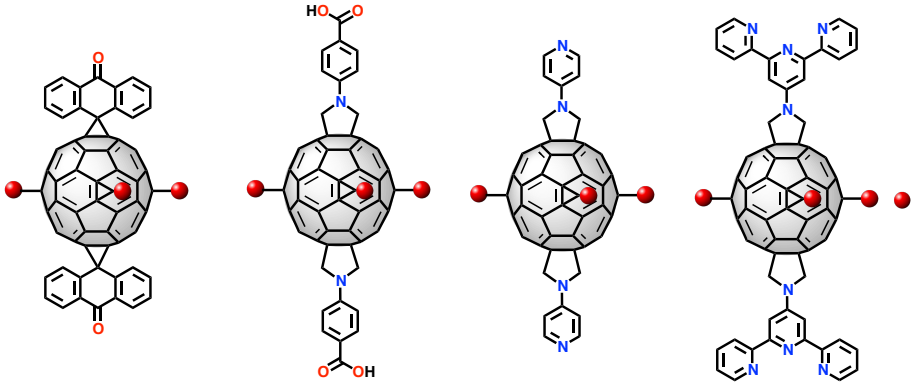

Figure 1.22: Fullerenes *hexa*-adducts for the application in single molecule conductance.

1.4 Experimental Section

1.4.1. Orthogonal transposition method:

Synthesis of compound 3.

C_{60}(2.0g, 2.74 mmol) was mixed in the solid phase with anthracene (0.98g, 5.48 mmol) and sealed under vacuum. The mixture was placed in the oven at 240°C for 1 hour. We transferred the solid to an Erlenmeyer flask and added 650mL of anhydrous diethyl ether. The black solid was collected by centrifugation followed by the addition of 150 mL of CS_2. The sample was sonicated for 30 minutes and a light brown solid was collected by filtration (2.1g, 88% yield).

Synthesis of compound 4.

Compound **3** (2.0g, 1.8 mmol) was added to a round bottom flask along with 100 mL of anhydrous DCM. The flask was sealed with a septum and the reaction was carried under an inert atmosphere. 1,8-Diazabicyclo[5.4.0]undec-7-ene (DBU-5.43 mL, 36.36 mmol) and diethyl bromomalonate (6.12 mL, 36.36 mmol) were added to the reaction mixture. The reaction was left at room temperature for 24 hours. After 24 hours, DBU and diethyl bromomalonate were added

again and the reaction was left for another 24 hours. After removal of the solvent, the red oil was washed with acetone. An orange powder was collected by filtration (87% yield)

Synthesis of compound 5.

Compound **4** was sealed under vacuum and left in the oven for 5 min at 195°C. The product was purified by column chromatography using DCM as the eluent. A brown-green solid was obtained (65% yield). ^{1}H-NMR (600 MHz, $CDCl_3$)= δ 4.49 (q, 16H), 4.46 (q, 16H), 1.43 (t, 22H), 1.40 (t, 24H).

1.4.2. Metallopolymers:

Synthesis of compound 6:

The compound was synthesized according to a modified literature procedure.[32] CBr_4 (53.7 mg, 0.162 mmol) and 4,5 diazofluorene (27.2 mg, 0.162 mmol) were added to a solution of compound **5** (100.0 mg, 0.073 mmol) in anhydrous CH_2Cl_2. The solution was stirred at room temperature for 15 min followed by the addition of 1,8-diazabicyclo[5.4.0]undec-7-ene (44.9 mg, 0.294 mmol). The reaction mixture was stirred at room temperature during 4 hours. After removal of the solvent under reduced pressure, the residue was purified by silica gel column chromatography using DCM : 10% MeOH as the mobile phase. A yellow solid was obtained in a 73% yield (89 mg). ^{1}H NMR (400 MHz, $CDCl_3$) δ 8.81 (dd, J = 4.8, 1.3 Hz, 4H), 8.70 (dd, J = 8.1, 1.3 Hz, 4H), 7.40 (m, 4H), 4.46 (q, J = 7.1 Hz, 8H), 4.23 (q, J = 7.1 Hz, 4H), 1.43 (t, J = 7.1 Hz, 12H), 1.24(t, J = 7.1 Hz 12H). UV-Vis λ_{max} (nm): 244, 285, 318, 340, 394. MALDI-TOF MS: calcd. 1684.338 $[M]^+$, found 1684.635 $[M]^+$.

Synthesis of polymer 10:

Compound **6** (10 mg) was dissolved in 1 mL of anhydrous CH_2Cl_2. A solution of $HgCl_2$ (1.6mg) in EtOH (1mL) was layered on top of the solution of compound **6**, followed by the addition of 0.5 mL of benzene. After two days light yellow crystals were formed and stored in the freezer.

Synthesis of polymer 11:

Compound **6** (10 mg) was dissolved in 1 mL of anhydrous CH_2Cl_2. A solution of $Cd(NO_3)_2$ (1.8mg) in M3OH (1mL) was layered on top of the solution of compound **6**, followed by the addition of 0.5 mL of toluene. After two days, light yellow crystals were observed and stored in the freezer.

Synthesis of polymer 12:

Compound **6** (10 mg) was dissolved in 1 mL of anhydrous CH_2Cl_2. A solution of ZnBr (1.3 mg) in EtOH (1mL) was layered on top of the solution of compound **6**, followed by the addition of 0.5 mL of benzene. After two days, light green crystals were observed and stored in the freezer.

Synthesis of polymer 13:

Compound **6** (10 mg) was dissolved in 1 mL of anhydrous CH_2Cl_2. A solution of $CuCl_2$ (0.7 mg) in MeOH (1mL) was layered on top of the solution of compound **6**, followed by the addition of 0.5 mL of benzene. After two days, light green crystals were observed and stored in the freezer.

Synthesis of polymer 14:

Compound **6** (10 mg) was dissolved in 1 mL of anhydrous CH_2Cl_2. A solution of $CuCl_2$ (1.4 mg) in MeOH (1mL) was layered on top of the solution of compound **6**, followed by the addition of 0.5 mL of benzene. After two days, light green crystals were observed and stored in the freezer.

Crystallographic data:

The crystallographic data for all the synthesized metallopolymers can be found in the appendix.

Chapter 2: Fullerene Based Metal Organic Frameworks

2.1 INTRODUCTION

Hydrogen promises to be one of the major energy sources that could replace fossil fuels. However, limited on-board storage capacity remains a challenge. For future automobile applications, the US Department Of Energy (DOE) has identified specific targets for hydrogen storage systems. Targets of 5.5 wt% H_2 gravimetric capacity and a volumetric capacity of 40g of H_2/L are based on the mass and volume of the entire system and must be achievable between 40 - 60L.[36] There are different methods to store hydrogen: high pressure tanks, cryogenic liquefaction of molecular hydrogen, chemical solid storage materials and physically adsorbing materials. Recently, a lot of research has been done on physically adsorbing materials as they do not require unacceptably high temperatures to release hydrogen and do not exhibit poor release kinetics and storage material recycling. For this type of materials, the hydrogen storage capacities appear to be governed by the specific surface area, pore shape and size.[37] Materials that satisfy these requirements include microporous materials as metal organic frameworks (MOFs). On the other hand, and as will be described later, fullerenes are also potential candidates for hydrogen storage materials. Hence, if we incorporate fullerenes as integral linkers in MOFs we should have a material with high gravimetric/volumetric density of hydrogen molecules able to operate at high pressures and we might enhance both the scope and diversity of MOFs.

In this chapter we will give a brief introduction to metal organic frameworks (MOFs) and their application in hydrogen storage. We will also describe the application of fullerenes in hydrogen storage and the incorporation of fullerenes in extended networks for different applications. Finally, we will present the design and synthesis of different novel regioselective fullerene derivatives and their incorporation as integral linkers of extended networks.

2.1.1 Metal Organic Frameworks

Metal Organic Frameworks (MOFs), hybrid materials from organic struts and inorganic nodes, constitute an alternative for achieving long-range organization and order.[38-40] MOFs exhibit exceptional chemical and structural diversity, porosity and tunable structure and properties. Additionally, these types of materials have different applications: gas and chemical storage, chemical separations, sensing, selective catalysis, ion exchange and drug delivery.[41-43] Their simple preparations are generally high yielding and scalable, and by careful use of building blocks different target products can be produced.[44]

In 1999 the first robust and highly porous MOF was reported, figure 2.1. MOF-5 resulted from the complexation of a dicarboxylate linker, terephthalic acid, in the presence of Zn(II). [45] Since then, multiple efforts have been made to use different organic linkers and metals to enhance both the scope and diversity of this type of materials.

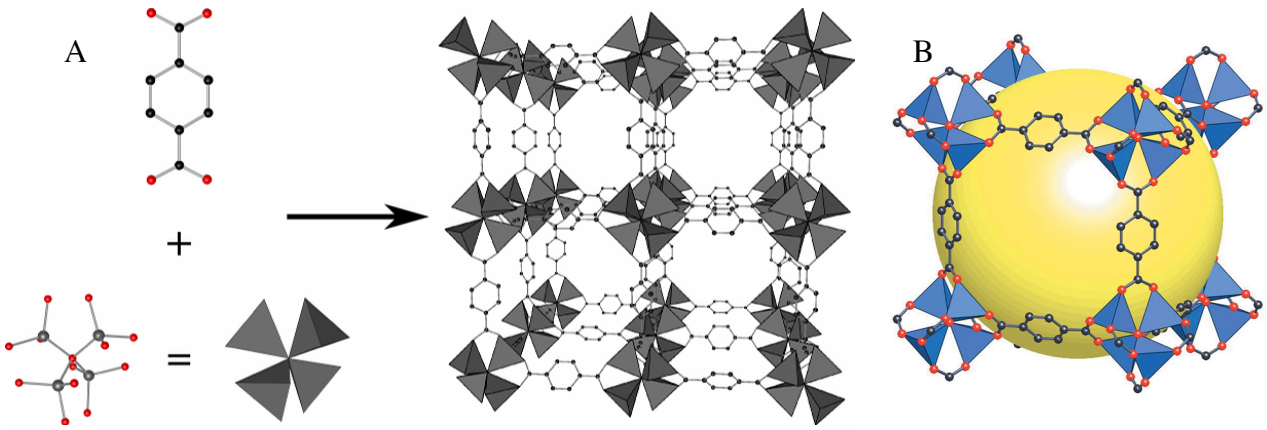

Figure 2.1: Structure of MOF-5. A) Assembly of the MOF by the reaction of terephthalic acid and Zn. B) Representation of the porosity of the framework. The yellow ball represents the empty space.

MOFs have attracted attention for hydrogen storage applications due to their large surface areas and relatively high hydrogen uptake at low temperatures.[44, 46-53] The Yaghi group first reported that MOF-5 showed a 4.5wt% H_2 uptake at 78K and 0.8 bar and it stored 1wt% of H_2 at 298K and 20 bar.[54] Different MOFs with the potential to improve the hydrogen storage properties

exhibited by MOF-5 have been synthesized; nonetheless, a material with high gravimetric/volumetric density of hydrogen molecules able to operate at high pressures is still missing. Additionally, it has been shown that the volume occupied by hydrogen in each material is quite low; only a small amount of the surface is occupied and most of the pore volume is not utilized.[44] Therefore, there is a need to optimize the pore size to reduce the fraction of under-utilized void space, increasing the volumetric capacity and attractive adsorbate-adsorbent interactions.[44]

MOFs are generally prepared in "one-pot" solvothermal syntheses under mild conditions. Among the different strategies for the assembly of MOFs, we are particularly interested in two of them. The first one is the use of a dicarboxylate linker in a reaction that gives super tetrahedron clusters forming cubic structures as the ones shown in figure 2.2. The second strategy consists in the formation of a 2D-layer (figure 2.2, b) followed by the addition of a linker that would act as a pillar (figure 2.2-c). Tetracarboxylic acid linkers are commonly used as struts and bipyridine linkers are used as pillars as shown in figure 2.2.

2.1.2 Fullerenes as hydrogen storage materials

Fullerenes are known to readily react with hydrogen and different hydrogenation methods have been studied: Brich reductions, zinc/acid reduction, borane reduction, transfer hydrogenation and catalytic hydrogenation.[55] In principle, a maximum of 60 hydrogen atoms can be bonded both endohedrally and exohedrally to the fullerene cage surface, resulting in a stable isomer, $C_{60}H_{60}$, loaded with 7.7wt% hydrogen which meets and exceeds all the requirements for hydrogen storage materials set by the DOE. However, the only fully hydrogenated fullerene that has been synthesized so far is $C_{20}H_{20}$.[56] Partially hydrogenated $C_{60}H_n$ cages, with n=2-44, have been synthesized [57-58] and theoretical calculations have predicted that the most stable $C_{60}H_n$ cages should be $C_{60}H_{18}$, $C_{60}H_{36}$ and $C_{60}H_{48}$.[59-61]

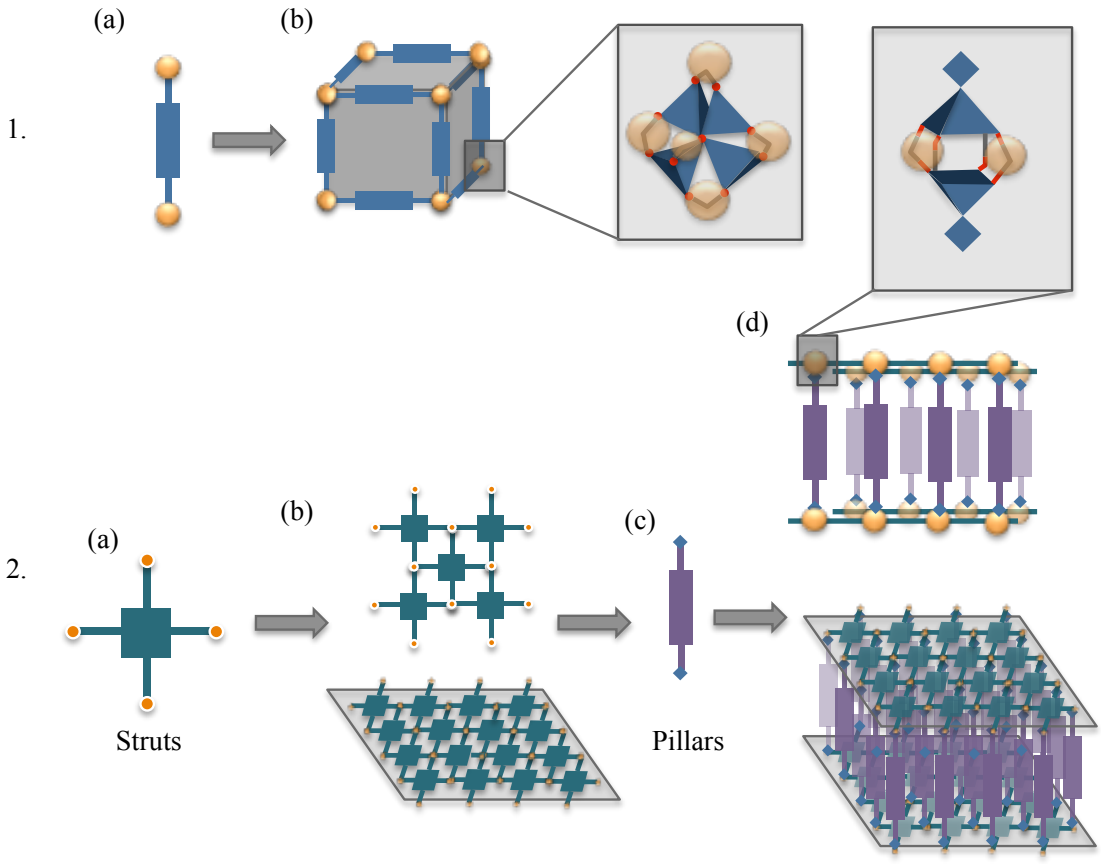

Figure 2.2: Pictorical representation of the assembly of MOFs. Part 1 shows the assembly of a dicarboxylate fullerene derivative. Carboxylic acids are represented by the yellow balls. 2a) Shows the struts and their assembly into a 2b) 2D-layer in the presence of Zn. The 2D-layer can be transformed into a porous 3D-structure using 2c) bipyridine linkers as the pillars. The blue squares represent the pyridine groups. Both insets, a) and b) show the coordination of the Zinc atom represented by the blue pyramids.

Fullerenes offer different possibilities for hydrogen storage because hydrogen cannot only be adsorbed on the surface of the fullerenes but it can also be accumulated inside them. [62-63] Theoretical studies have concluded that hydrogen accumulation inside fullerenes is not likely due to the high penetration barrier. Nevertheless, H adsorption on the fullerene outer surface is possible; H adsorption occurs without a barrier and molecular H_2 can be adsorbed if the activation energy for the dissociation is supplied.[62] In the case of H atom adsorption, the larger the curvature of the fullerene, the more reactive the surface is and the more easily the H_2

molecule dissociates and H atoms adsorb to the surface. Once two H atoms are adsorbed on the surface, they can recombine and form an H_2 molecule that desorbs from the fullerene. The energy required for the desorption of H_2 is lower for flat surfaces than for curved surfaces. Hence, the adsorption is more effective for smaller fullerenes, whereas the H_2 molecule recombination and desorption goes easier on flatter surfaces.

As mentioned before, a material useful for hydrogen storage should demonstrate a reversible storage capacity at ambient pressure and temperature. Hydrogen chemisorption on fullerenes fulfilled this requirement partially as the C-H bond is weaker than the C-C bond, an increase in temperature will preferably break the C-H bond and dehydrogenate the structure without destroying it.

Not only pristine fullerenes have been studied for application in hydrogen storage materials, recently, some theoretical studies predicted different organometallic carbon fullerenes as potential hydrogen storage materials. [64] Sun and coworkers predicted that a C_{60} fullerene can be coated with Li atoms on which H_2 can be adsorbed with an adsorption energy of 0.075 eV per H_2. [65] Additionally, the hydrogen storage capability of Transition Metals (TM)-coated C_{60} and $C_{48}B_{12}$ fullerenes has been studied. It was predicted that the maximum hydrogen storage in theses systems could be as high as 9 wt% which is higher that the one predicted for pristine C_{60}. [66-67] Additionally, Sun and coworkers also suggested that Li-coated and B-doped heterofullerene ($Li_{12}C_{48}B_{12}$) could store hydrogen up to 9 wt %. Finally, theoretical studies showed that Ca-coated fullerenes should be able to reach a hydrogen uptake of 8.4 wt%, which is close to the DOE target.[68]

Zhen and coworkers theoretically designed fullerene-based frameworks for hydrogen storage. Both frameworks were constructed connecting exohedral metallofullerene nodes with conjugated organic linkers (see fig 2.3). Their results showed that hydrogen molecules can be adsorbed in the frameworks with hydrogen binding energies ranging from 0.15-0.50 eV, meeting the optimal adsorption condition for hydrogen storage. The fullerene frameworks can entail molecular H_2 binding in the range of 8.0-9.2 wt %, meeting the DOE target.[64]

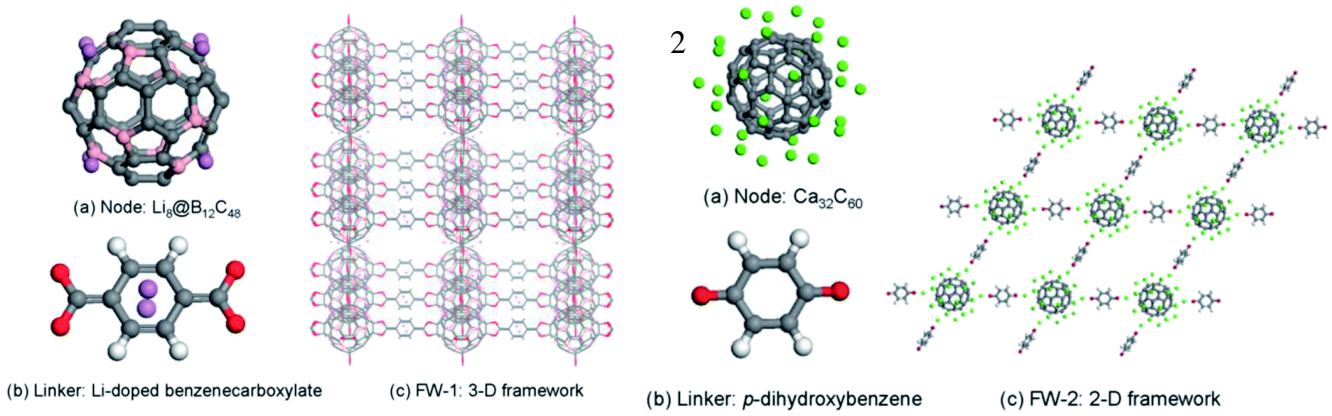

Figure 2.3: 1a) $Li_8@C_{48}B_{12}$. 1b) Li-doped benzenedicarboxylate. c) 3-D organic framework constructed by 1a and 1b. 2a) $Ca_{32}C_{60}$. 2b) *p*-dihydroxybenzene. C) 2-D film constructed by 2a and 2b. Reproduced with permission from ref32.

2.1.3 Fullerene and MOFs

Different attempts have been made to incorporate fullerenes in extended structures. The first one included the encapsulation of fullerenes inside MOFs and the second one included the use of fullerenes as linkers in the construction of MOFs. Both strategies will be described below.

2.1.3.1 Fullerenes inside MOFs

One of the strategies to optimize the pore-size of MOFs and hydrogen volumetric density is to insert a molecule within the large-pores of the framework. In addition to reducing the free diameter of the pores, such guests may provide additional adsorptive sites. The guest molecule should not block the adsorptive sites on the framework, and it must be well-anchored or have very low vapor pressure to prevent its desorption along with hydrogen.[44] There have been a few MOFs reported that incorporate C_{60} molecules as pillars between layers or trapped in pores or cavities. [69-71]

MOF-177, shown in figure 2.4, can absorb sixteen C_{60} molecules in the unit cell at 300 K and 1 bar (figure 2.3). The C_{60} inclusion leads to a decrease in the free volume of the MOF to 0.61 cm^3g^{-1} from 1.54 cm^3g^{-1}. It was shown that the inclusion of C_{60} increases H_2 uptake at low pressure compared with pure MOF-177 at 77 and 300K. However due to the lower pore size of

C_{60}@MOF-177, the H_2 storage capacity at high pressure is lower than for MOF-177. Although it was expected that the C_{60} molecules would be positioned in the center of the pores to minimize dead volumes for H_2 storage, C_{60} attractively interacted with MOF-177 and another C_{60}, blocking the existing adsorptive site of the MOF-177. The H_2 uptake of the impregnated MOF at 300K is not enough to meet the DOE target of 6.0 wt%, indicating that the impregnation might not be an effective alternative for practical hydrogen storage.[37]

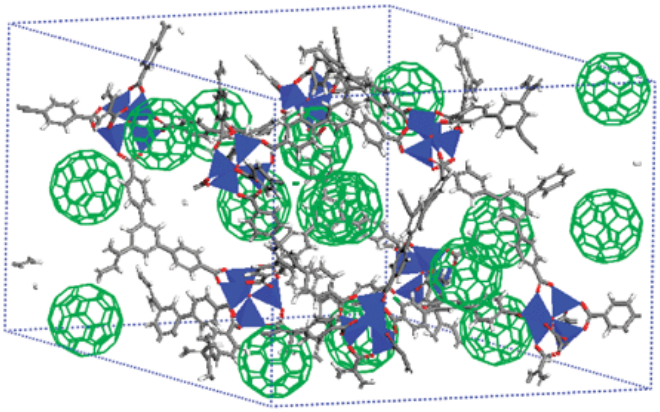

Figure 2.4: A C_{60}-impregnated MOF-177 structure. Copyright Royal Society of Chemistry. Appendix 3.

2.1.3.2 Fullerene-based MOFs

To date, there are no reports of a 3D-fullerene based porous structure. In 2014, Ping et al reported the first 2D-fullerene based MOF where a fullerene derivative with four coplanar nitrogen atoms reacted with $Cd(NO_3)_2$ H_2O to form an extended network, figure 2.5. However, intercalation of the monomeric fullerene derivative between the layers lead to a non-porous structure.[72]

On the other hand, two *hexakis*-adducts with twelve glycolic acid or 3-hydroxypropionic acid side chains attached to its malonate units, see figure 2.6, were incorporated as organic connectivity centers in a 3D framework by coordination with Zn; however, neither framework proved stable upon solvent removal and therefore no permanent porosity was obtained for these materials.[73]

The successful crystallization of different polymers and the formation of a 2D-fullerene based MOFs suggest that fullerene linkers can be successfully incorporated as integral building blocks in complex supramolecular structures. The design and synthesis of fullerene based MOFs for hydrogen storage applications is described in the next section (Results and discussion).

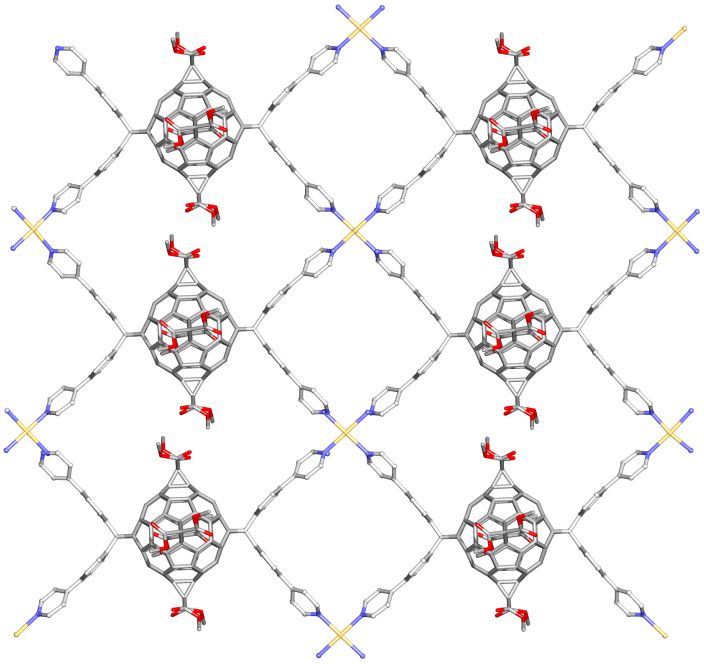

Figure 2.5: Crystal structure of a 2D fullerene-based MOF.

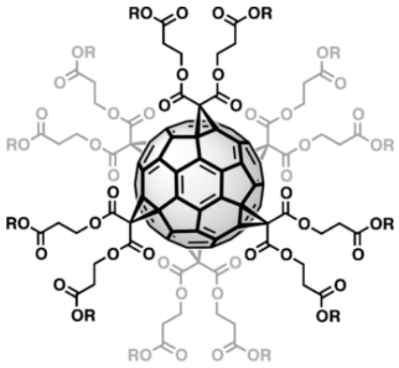

Figure 2.6: Fullerene *hexakis*-adduct for the construction of MOFs.

2.2 Results And Discussion

As mentioned before, we can synthesize fullerenes with addends in a *trans*-**1** position relative to each other. With this strategy in mind and considering that most of the linkers used in the construction of MOFs include pyridines or carboxylic acids, we designed four different fullerene derivatives, figure 2.7. The synthesis and characterization for each fullerene derivative is explained in the experimental section.

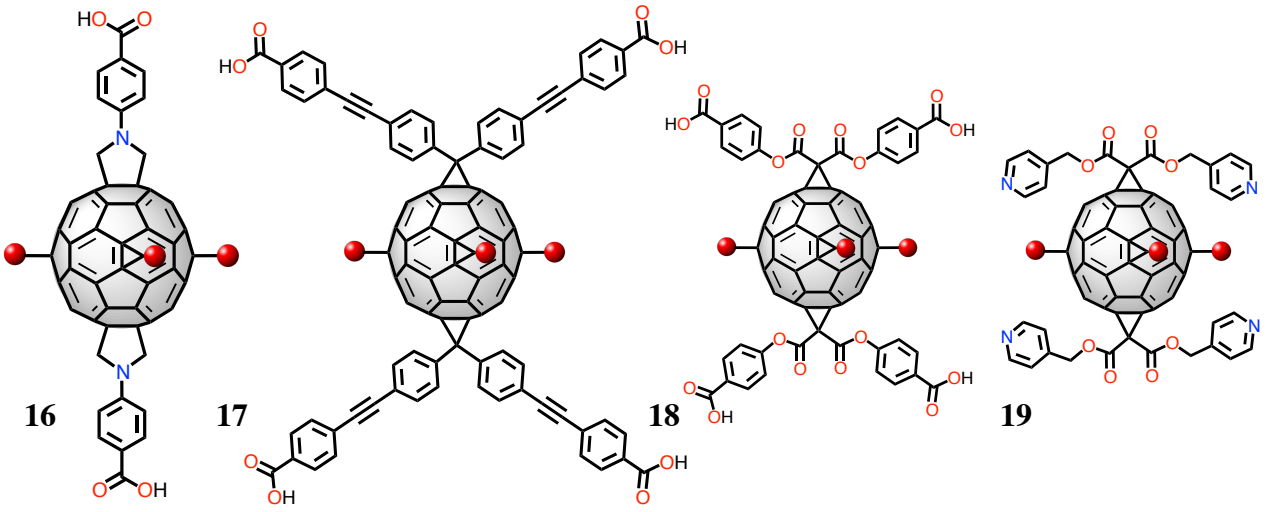

Figure 2.7: Fullerene *hexakis*-adducts for the construction of MOFs. The malonate groups are represented with red balls.

DFT calculations were performed to compare the orientation and distribution of the four carboxylic acids in compound **17** with the orientation of the carboxylic acids in the commonly used tetra-COOH porphyrin. As shown in figure 2.8, although the angles between the carboxylic acids differ, their orientation is exactly the same in both porphyrin and fullerene derivative. Hence, we expect that compound **17** would behave similarly to the porphyrin, forming 3D frameworks in the presence of a bi-pyridine linker. [38]

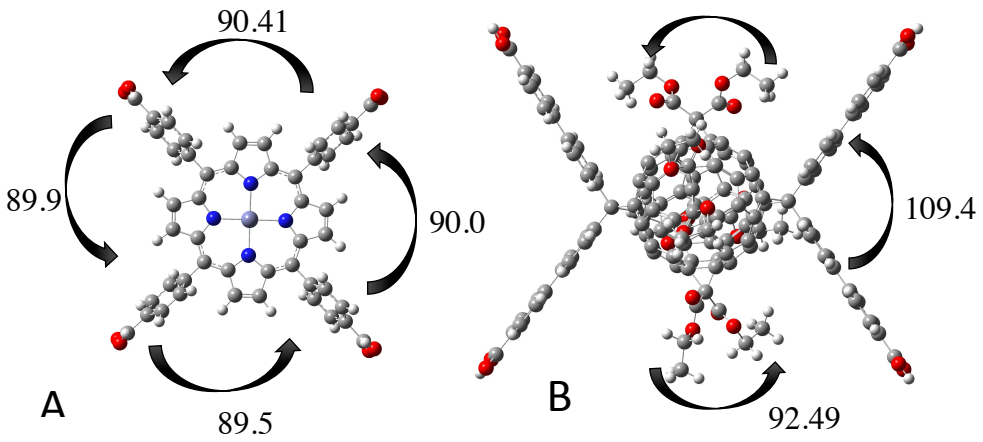

Figure 2.8: Optimized geometries by DFT calculations of a) tetra-COOH porphyrin and b) compound 17. The arrows show the angles between the carboxylic acids which are located in a triangle.

Structures **17** and **18** can be used as the struts due to the presence of four carboxylic acids in a rectangular position, figure 2.9. As shown in figure 2.2, tetracarboxylic acid compounds can be incorporated into 3D-structures when a bipyridine pillar is used. Figure 2.8 shows the calculated 3D-MOF when compound **18** and Bodipy (**20**) react in the presence of Zinc. A similar 3D-MOF can be formed when **17** reacts with bodipy in the presence of Zn(II), figure 2.10.

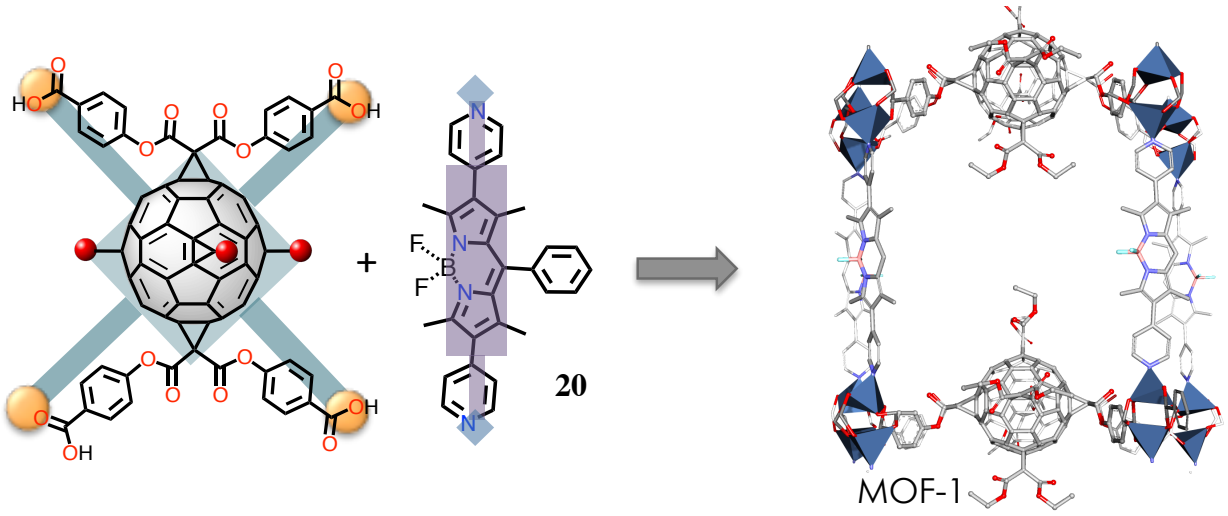

Figure 2.9: Synthesis of MOF-1. The MOF structure was calculated using molecular mechanics.

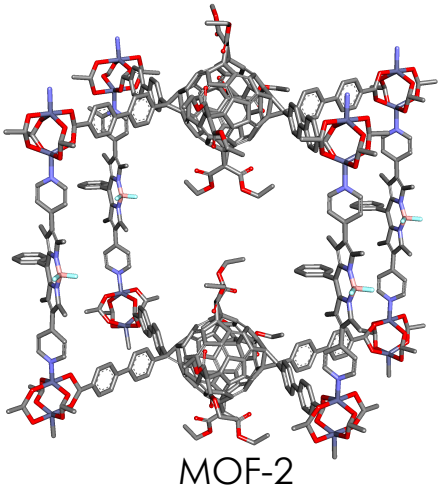

Figure 2.10: Computed structure of MOF-2 using molecular mechanics. Color code: O, red; C, grey; N, blue.

Compound **16** will be used as the only linker in the same way as terepthalic acid was used in the construction of MOF-5 as shown in figure 2.2-a. The resulting structure is a cubic extended network, figure 2.11. Finally, compound **19** can be used as the bipyridine pillar, figure 2.12, and the commercially available tetracarboxylic acid porphyrin can be used as the struts.

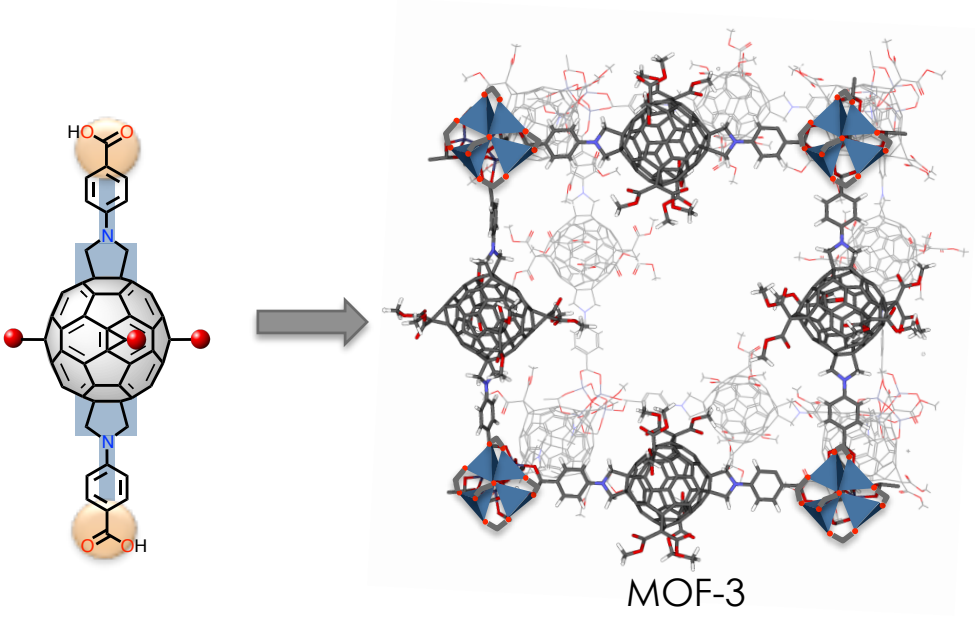

Figure 2.11: Computed structure of MOF-3 using molecular mechanics. Zinc atoms are shown in blue tetrahedrons. Color code: O, red; C, grey; N, blue.

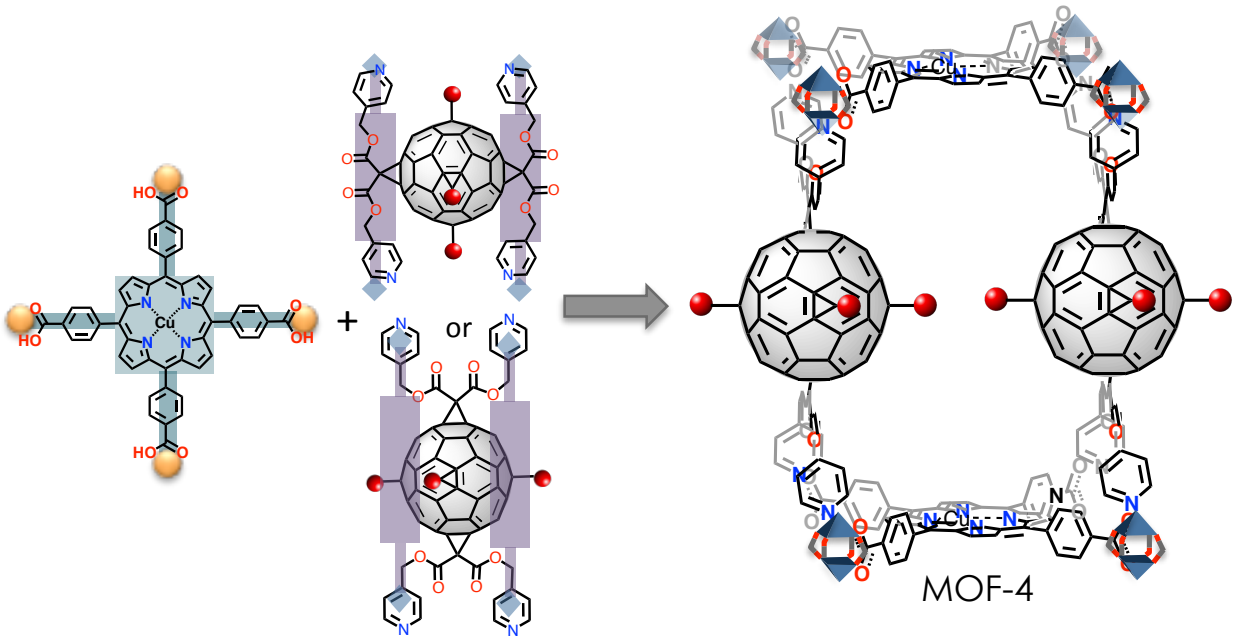

Figure 2.12: Computed structure of MOF-4 using molecular mechanics. Zinc atoms are shown in blue tetrahedrons. Color code: O, red; C, grey; N, blue.

The four compounds in figure 2.7 were successfully synthesized, purified and characterized (for details please see the synthetic section). For the synthesis of compound **16**, we used a 1,3-dipolar cycloaddition reaction. The *penta*-adduct was synthesized and purified first to limit the number of resulting isomers.[74] Several attempts have been made to incorporate **16** as a linker in a 3D-MOF; however, we have not been able to obtain an air-stable single crystal. Both solvothermal and slow diffusion methods have been explored. In the solvothermal method, we have used both N,N-Diethylformamide (DEF) and N,N-dimethylformamide (DMF) as solvents, varying the temperature from 80° – 120° and modifying the ramping and cooling times. For the slow diffusion method, triethylamine (TEA) is layered on top of a solution containing the compound in DEF, DMF or *ortho*-dichlorobenzene (o-DCB). A yellow powder was formed by slow diffusion of TEA on 2 mL of DEF (2 mg of **16**). The powder was not soluble in DMF, DEF, o-DCB, dichloromethane, tetrahydrofuran or methanol, suggesting that an extended

network was formed. Figure 2.13 shows the Fourier Transform Infrared (FT-IR) spectrum of the yellow powder and the starting materials (C_{60}-tetramalonate and *trans*-**1** hexakis adduct). Some of the characteristic bands shown in the IR spectrum of the *trans*-**1** fullerene derivative - Blue line in figure 2.13- include the peak for the C=O stretch of the malonates (1750 cm^{-1}) and the C-H aromatic stretching. In comparison with the starting material, the IR spectrum of the yellow powder exhibits broad signals, which is a common phenomenon for porous materials. Additionally, the CO stretching frequency decreases to 1580 cm^{-1} from 1750 cm- due to the redistribution of the electron density around the CO bond caused by the presence of the metal. The IR spectrum of the yellow powder shows a broad band at 3300 cm^{-1} due to hydrogen bonding of the solvent inside the pores of the MOF. After evacuation of the solvent from the yellow powder (the sample was left under vacuum at 180°) the broad band at 3300 cm^{-1} disappeared. These results provide additional evidence that the yellow powder corresponds to an extended fullerene network.

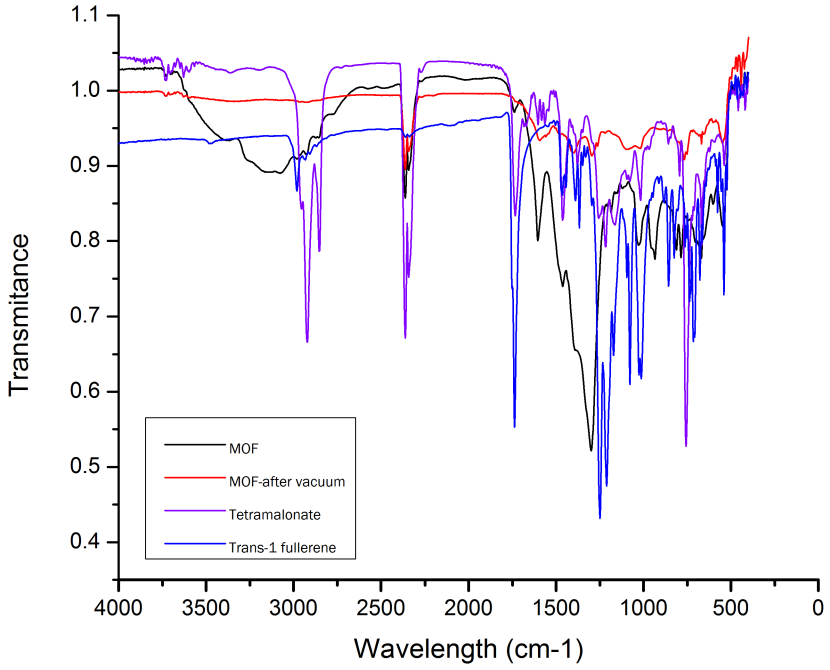

Figure 2.13: ATR-IR spectrum. Black line –yellow powder (MOF); red line-MOF after evacuation under vacuum; purple line – C_{60} tetramalonate; blue line – compound 16.

Brown and purple crystals were obtained when Cu(II)meso-tetra(4-carboxyphenyl)porphine was reacted with $Zn(NO_3)_2$ in DMF followed by the addition of compound **19** and HNO_3, see figure 2.14. The unit cell of the purple crystals corresponded to the unit cell of the porphyrin and the brown crystals were very small and decomposed when left standing at room temperature.

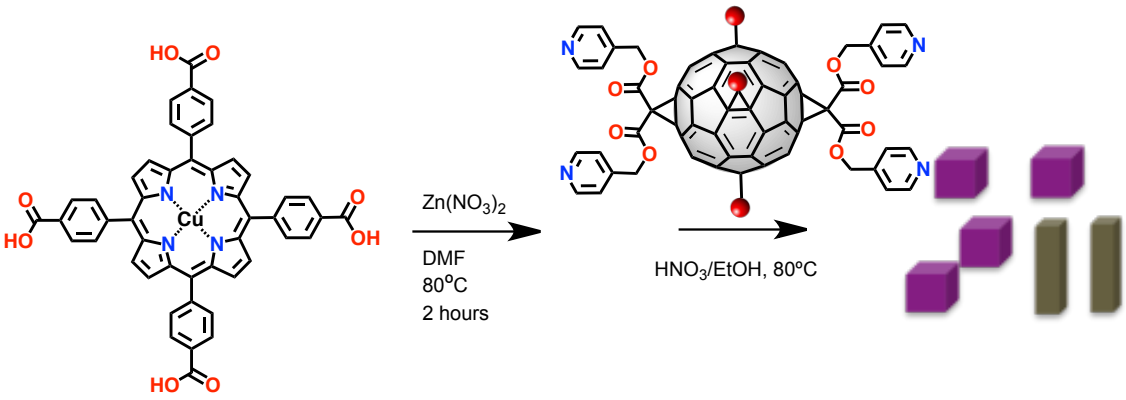

Figure 2.14: Synthetic scheme for MOF-4.

2.3 Future Work

We will complete the characterization of the yellow powder obtained in the synthesis of MOF-3, figure 2.11, using thermogravimmetric analysis (TGA) and powder X-ray diffraction (PXRD). We also established a collaboration with the NanoUp group in Spain where they will attempt the crystallization of the MOFs and we will synthesize the fullerene linkers. The NanoUp group has a lot of experience in working with limited quantities of new ligands for the synthesis of MOFs. For the synthesis of MOF-4, figure 2.12, we will substitute the nitric acid with acetic acid as the strength of the acid affects the crystallization process. Additionally, the equivalents of the Zinc salt also play an important role in the crystallization process. As a result, we designed different experiments that will be carried on using two different solvents -DEF and DMF, the equivalents of the Zn salt will vary from 4 to 12, and we will used acetic acid and different temperatures - 75 , 95 and 115° . We are currently synthesizing enough amount of compounds **16** and **17** to start the complexation trials using Zinc as the metal.

We started the synthesis of MOFs with Zn(II) as it is a well known bimetallic unit (M_2)

and there are different reports on the synthesis of supramolecular architectures with this motif. MOFs containing M_2 (Zn(II), Cu(II)) paddlewheel motifs lack structural stability upon redox changes and show chemically irreversible electrochemical behavior. However, these M_2 units can be replaced by more complex M^*_2 units such as Cr_2, Mo_2, W_2 and Ru_2 resulting in materials with different properties. The next chapter will describe the importance of the M^*_2 units and their incorporation in fullerene-based supramolecular architectures.

2.4 EXPERIMENTAL SECTION

2.4.1 Instrumentation

^{1}H and ^{13}C-NMR spectra were recorded on a JEOL ECA 600 NMR spectrometer at room temperature using $CDCl_3$ or THF-d_8 as solvent. UV-vis spectra were collected at room temperature using a Varian UV-vis-NIR Cary 5000 spectrophotometer. Mass spectra were obtained using a Bruker microFlex MALDI-TOF spectrometer on reflector positive or negative mode. Electrochemical experiments were performed with a CHI-660A electrochemical workstation. IR spectra were collected with a FT-IR Tensor II spectrometer using Attenuated Total Reflectance (ATR).

2.4.2 Synthesis of compound 16

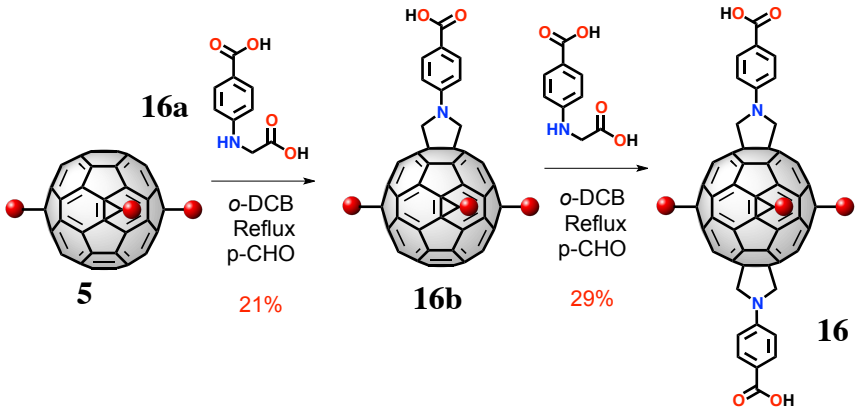

Synthesis of compound 16a:

The synthesis of compound **16a** is described under the experimental section of chapter 4.

Synthesis of compound 16b:

The general procedure for a 1,3-dipolar cycloadditon was followed. Compound **5** (100 mg, 0.07 mmol) was added to a flask along with p-formaldehyde (0.7mmol) and COOH-glycine (25 mg, 0.11 mmol). The mixture was dissolved in anhydrous o-DCB and left under reflux for 4 hours. The reaction was followed by TLC, when an orange or yellow spot appeared the reaction was stopped. The solvent was removed under reduced pressure. The product was purified by silica gel column using DCM and 10%MeOH as the mobile phase. A red oil was obtained. The oil was washed with ether. ^{1}H-NMR (400 MHz, $CDCl_3$) = δ7.23 (d, J = 8.8 Hz, 2H), 6.12 (d, J = 8.9 Hz, 2H), 3.67 -3.49 (m, 20H), 0.62-0.49 (m, 24H); MALDI-TOF MS: calcd. 1512.325[M^+], found 1512.566[M^+]

Synthesis of compound 16:

The general procedure for a 1,3-dipolar cycloadditon was followed. Compound **16b** (20 mg, 0.07 mmol) was added to a flask along with *p*-formaldehyde (0.17mmol) and COOH-glycine (5 mg, 0.11 mmol). The mixture was dissolved in anhydrous o-DCB and left under reflux for 24 hours. The solvent was removed under reduced pressure. The product was purified by silica gel column using DCM and 10%MeOH as the mobile phase. A yellow powder was obtained. ^{1}H-NMR (400 MHz, $CDCl_3$) =δ7.95 (d, J = 9.0 Hz, 4H), 6.66 (d, J = 9.0 Hz, 4H), 4.54-4.20 (m, 20H), 1.39-1.31 (m, 24H); ^{13}C-NMR (600 MHz, $CDCl_3$) = 171.59, 163.80, 155.87, 153.84, 146.16, 145.97, 143.43, 143.12, 138.60, 138.20, 132.32, 132.05, 115.66, 110.68, 67.75, 62.95, 51.82, 40.06, 30.24;MALDI-TOF MS: calcd. 1678.431[M^+], found 1676.315[M^+-2H]. The signals for the protons of the pyrrolidine ring overlap with the signals of the methylenes in the malonate groups.

2.4.3 Synthesis of compound 17

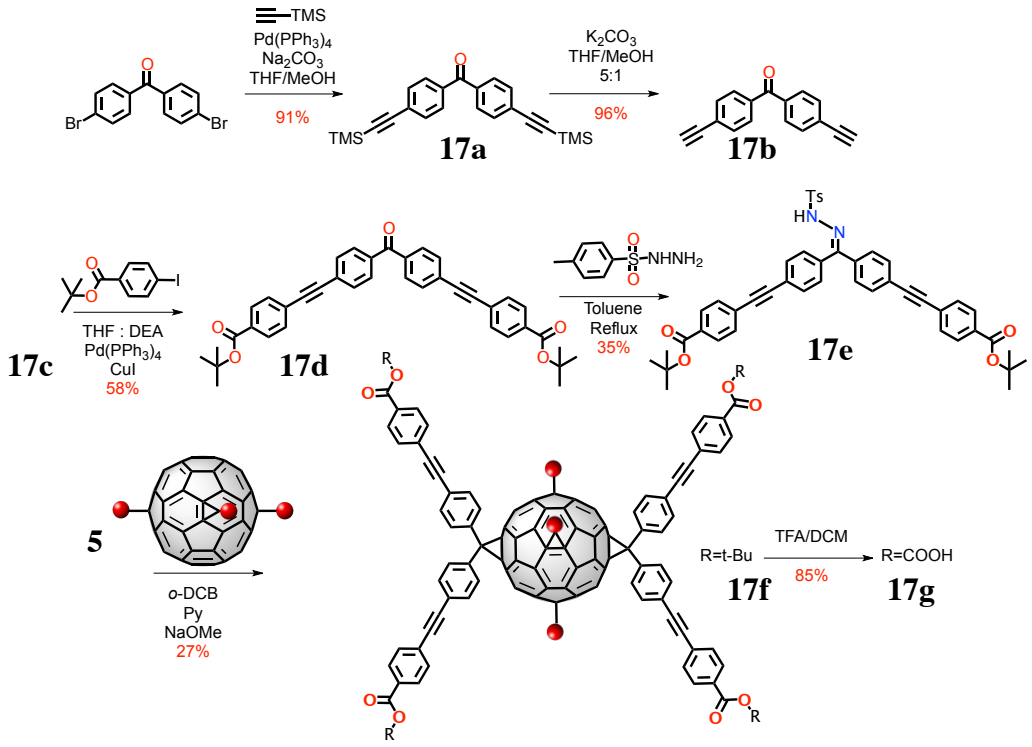

Synthesis of compound 17a:

4,4'-Dibromobenzophenone (680 mg, 2.0 mmol), triphenylphosphine (100 mg, 0.3 mmol), Copper Iodide (50 mg) and tris(dibenzylideneacetone)dipalladium(0) (5%mmol) were added into a round bottom flask. 15 mL of TEA were added followed by degasification of the solution for 30 min. The reaction was left under reflux for 1 hour. Trimethylsilylacetylene (2.0mL, 28 mmol) was added drop wise and the reaction was left under reflux for 4 hours. The solvent was removed and the product was extracted with DCM. The product was purified using silica gel column chromatography and DCM as the mobile phase(716 mg, 91% yield). ^{1}H-NMR (600 MHz, $CDCl_3$) = δ 7.99 (d, J = 8.3 Hz, 2H), 7.81 (d, J= 8.3 Hz, 2H), 7.67 (d, J = 8.2 Hz, 2H), 7.60 (d, J = 8.3 Hz, 2H), 5.30 (s, 18H)

Synthesis of compound 17b:

TMS-benzophenone (400 mg, 1.0 mmol) was dissolved in THF (50 mL) followed by the addition of 10 mL of MeOH. While stirring, potassium carbonate (147 mg, 20 mmol) was added.

The solution was stirred for 1 hour. The solution was filtered and the solvent was removed under vaccuum. The product was purified using column chromatography using DCM as the solvent. ^{1}H-NMR (400 MHz, $CDCl_3$) = δ 7.77 (d, J = 8.4 Hz, 4H), 7.63 (d, J = 8.4 Hz, 4H), 3.28 (s, 2H).

Synthesis of compound 17D:

Compound **17b** (100 mg, 0.4 mmol) and compound **17c** (304 mg, 1.0 mmol) were dissolved in anhydrous THF. The solution was degassed for 30 min followed by the addition of 1 mL of diethyl amine, 40 mg (5%mmol) of $Pd(PPh_3)_4$ and CuI (50mg). The reaction was refluxed under a nitrogen atmosphere overnight. The product was extracted with DCM and ammonium chloride. Compound **17d** was purified by column chromatography using DCM and Hexanes (5:1) as the mobile phase (58% yield). ^{1}H-NMR (600 MHz, $CDCl_3$) = δ 7.99 (d, 4H), 7.81 (d, 4H), 7.66 (d, 4H), 7.60 (d, 4H), 1.60 (s, 18H); MALDI-TOF MS: calcd. 582.68[M^+], found 586.191[M+H]$^+$

Synthesis of compound 17e:

A mixture of compound **17d** (20 mg, 0.03mmol) , *p*-toluene-sulfonyl hydrazide (1.2 eq), and MeOH:Toluene was stirred and refluxed overnight under an inert atmosphere using toluene as the solvent. The mixture was left without heating for one day and then cooled to -15ºC. White crystals were obtained (35% yield) and the subsequent synthesis of compound **17g** was done without further purification.

Synthesis of compound 16g:

Compound **16f** was dissolved in 2mL of dry pyridine in a three-necked flask. Under inert atmosphere, NaOMe (1.2 mg, 0.02 mmol) was added and the mixture was stirred during 15 minutes. A solution of **5** in anhydrous 1,2-dichlorobenzene was added, and the reaction mixture was stirred at 70°C during 24 hours. After removal of the solvent, the product was purified using DCM as the mobile phase. A yellow powder was obtained. MALDI-TOF MS: calcd. 1692.182

[M(pentaadduct)-2t-Bu]$^+$, found 1692.351 [M(pentaadduct)-2t-Bu]$^+$

2.4.4 Synthesis of compound 18

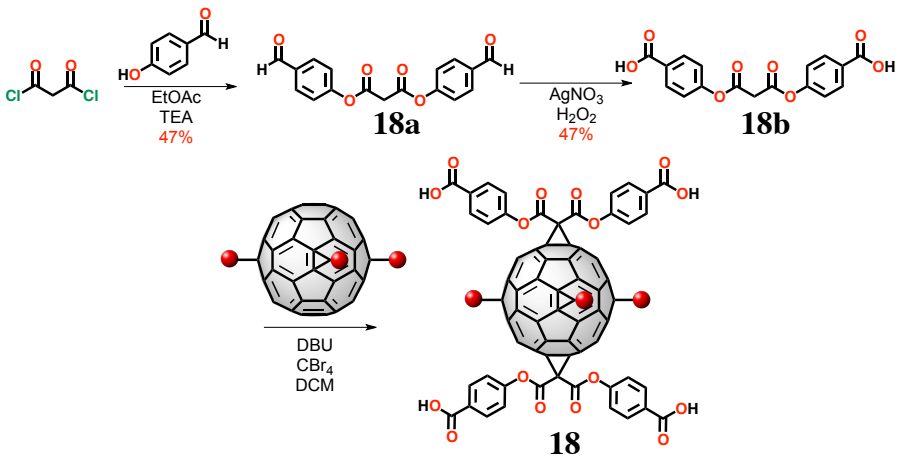

Synthesis of compound 18a:

Compound **18a** was prepared by refluxing *p*-hydroxybenzaldehyde (900mg, 5 mmol) and malonyl chloride (0.13 mL, 1 mmol) in degassed ethyl acetate for 24 hours. Compound **18a** was purified by silica gel column using DCM and THF as the mobile phase (10% THF). A yellow oil was obtained (47% yield). ^{1}H-NMR (400 MHz, $CDCl_3$) = δ 10.02 (s, 2H), 7.96 (d, J = 8.6 Hz, 4H), 7.36 (d, J = 8.5 Hz, 4H), 3.94 (s, 2H).

Synthesis of compound 18b:

Compound **17b** was dissolved in acetonitrile followed by the addition of 10 mol% $AgNO_3$ and 5 equivalents of 30% H_2O_2. The reaction was stirred at 50°C for 24 hours. After extraction with ether a white solid was collected and used without further purification.

Synthesis of compound 18c:

To a solution of compound **6** in DCM, CBr_4 (2.2 eq.), compound **18b** (2.2 eq.) and 1,8-dizabicyclo[5.4.0]undec-7-ene(DBU, 4 eq.) were added. The reaction mixture was allowed to stir at room temperature overnight. The solvent was dried under vacuum followed by the purification of compound **17c** by silica gel column using DCM and hexanes as the eluent (20:1).

A yellow solid was collected.

2.4.4 Synthesis of compound 19

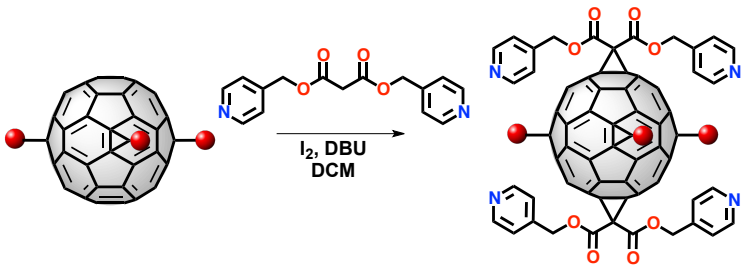

To a solution of 100.0 mg (0.074 mmol) of **6**, 41.5 mg (0.163 mmol) of I_2, and 46.5 mg (0.162 mmol) of bis-(pyrindin-4-ylmethyl)malonate[75] in 50 mL of CH_2Cl_2, 44 µL (0.294 mmol) of 1,8-diazabicyclo[5.4.0]undec-7-ene (DBU) were added. The reaction mixture was allowed to stir at room temperature overnight. The solvent was then removed under reduced pressure and the mixture was purified by silica gel column chromatography to get a light yellow solid (48.6 mg, 34% yield). ^{1}H-NMR ($CDCl_3$): δ = 8.56 (s, 8H), 7.18 (d, 8H, J = 6 Hz), 5.26 (s, 8H), 4.37 (q, 8H, J = 7.2 Hz), 4.33 (q, 8H, J = 7.2 Hz), 1.35 (t, 12H, J = 7.2 Hz), 1.33 ppm (t, 12H, J = 7.2 Hz). 13C{1H} NMR (CDCl3, 25 °C): δ = 163.81, 163.47, 150.24, 146.07, 145.95, 145.84, 143.31, 141.36, 141.31, 140.71, 122.54, 69.31, 69.16, 68.94, 66.68, 63.21, 63.13, 45.67, 45.54, 44.54, 14.22, 14.20 ppm. MALDI-TOF MS: [M+] 1920.40. UV-vis (CH_2Cl_2): λmax/nm = 271 , 281, 317, 334 and 388.

2.4.5 Synthesis of BODIPY

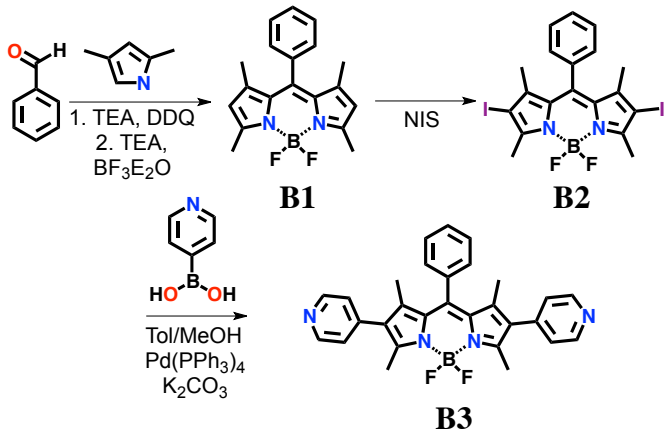

Synthesis of compound B1:

Benzaldehyde (508 μL, 5 mmol), 2,4-dimethylpyrrole (1.03 mL, 10 mmol) and DCM (250 mL) where added to a 500 mL round bottom flask. The reaction mixture was degassed for 30 minutes and TFA (5 drops) were added. The solution was stirred overnight under inert atmosphere. DDQ was added and the reaction was stirred for another hour. After extraction with $NaHCO_3$, the organic layer was collected and dried over $MgSO_4$. The solvent was removed and the product was purified using column chromatography with a micture of hexanes and DCM (1:2) as the eluent. A dark orange solid was collected (73% yield).

Synthesis of compound B2:

With ice bath cooling, compound **b1 (**168.5 mg, 0.054 mmol) was dissolved in anhydrous DCM (30 mL), followed by the addition of N-iodo succinimide (900 mg, 0.217 mmol) drop wise. The reaction was stirred during 12 hours. The product was purified by silica gel column chromatography using DCM:Hexanes as the eluent. ^{1}H-NMR (600 MHz, $CDCl_3$)= δ 8.64 (d, J = 5.5 Hz, 4H), 7.53 (d, J = 7.4 Hz, 2H), 7.35 (d, J = 6.5 Hz, 2H), 7.10 (d, J = 5.7 Hz, 4H), 2.57 (s, 6H), 1.57 (s, 6H).

2.4.4 Synthesis of MOFs

Synthesis of MOF-3

Compound **16** and $Zn(NO_3)_2$ were dissolved in DEF. The vial was heated up in the oven for 10 hours at 80°C. A slight change of color was observed but no solid was formed. We repeated the reaction at 100°C. A brown solid was formed. After washing the solid with anhydrous DMF and anhydrous DCM yellow crystals were collected. The diffraction of the crystals was too weak for X-Ray analysis.

We also tried a slow diffusion method. Triethylamine was layered on top of a solution of compound **16** in DEF. After three days a yellow powder was obtained and characterized using IR spectrometry.

Synthesis of MOF-4

A solid mixture of porphyrin and $Zn(NO_3)_2$ was dissolved in DMF in a 1 dram vial. The vial was sonicated for 5 min and placed in an oven at 80°C for 2 hours. While the solution was warm, compound **19** and an aliquot (1 mL) of HNO_3 in EtOH (0.03M) were added. The resulting suspension was heated in the oven at 80°C for 12 hours. We varied the solvents and temperatures: we used both DEF and DMF at 80 and 90. Additionally, we used different equivalents of the zinc salt.

Chapter 3: Fullerene-based Bimetallic Assemblies

3.1 Introduction

Compounds containing bimetallic units, M_2, displaying paddlewheel motifs are well known (especially Zn_2 and Cu_2), but MOFs containing stable, electrochemically active and reversible bimetallic centers M^*_2 are relatively scarce and their physical and chemical properties are not well studied.[76] These systems have the potential of having interesting physicochemical properties in addition to gas adsorption, such as multiple reversible electron transfers, magnetic behavior and catalytic activity. M^*_2 units in paddlewheel motifs (i.e. M = Cr, Mo, W, Ru, among others) possess very rich electrochemical properties.[77-81] These complexes are known to have interesting electronic structures that provide the possibility of multiple bonding between the metal atoms. Depending upon the specific electronic configuration of the metal atoms, these bimetallic units may show a range of bond orders between the metal atoms spanning from single to quadruple bonds. These multiply bonded electronic structures provide remarkable chemical and electrochemical stability that allows them to maintain structural integrity upon removal and addition of electrons, and show reversible electrochemical behavior.[77]

The introduction of metal-metal bonded species into supramolecular architectures can be controlled by designing the metallic units with a hierarchy of ligand labilities. Common ligands employed in the synthesis of dimolybdenum units include formamidinates, acetates and acetonitrile. N.N'-di-*p*-anisylformamidinate (Danif, figure 3.1) is commonly used in bi- metallic assemblies because the protons from the methoxy groups facilitate the analysis of the reactions by ^{1}H-NMR.

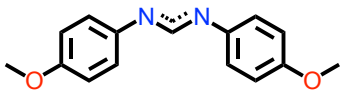

Figure 3.1: N,N'-di-*p*-anisylformamidinate (Danif).

The order of increasing lability is Danif<RCO_2^-<CH_3CN. By modifying the equivalents of the reagents different dimolybdenum units can be designed starting from dimolybdenum tetra-acetate ($Mo_2(O_2CCH_3)_4$ as shown in figure 3.2.[82]

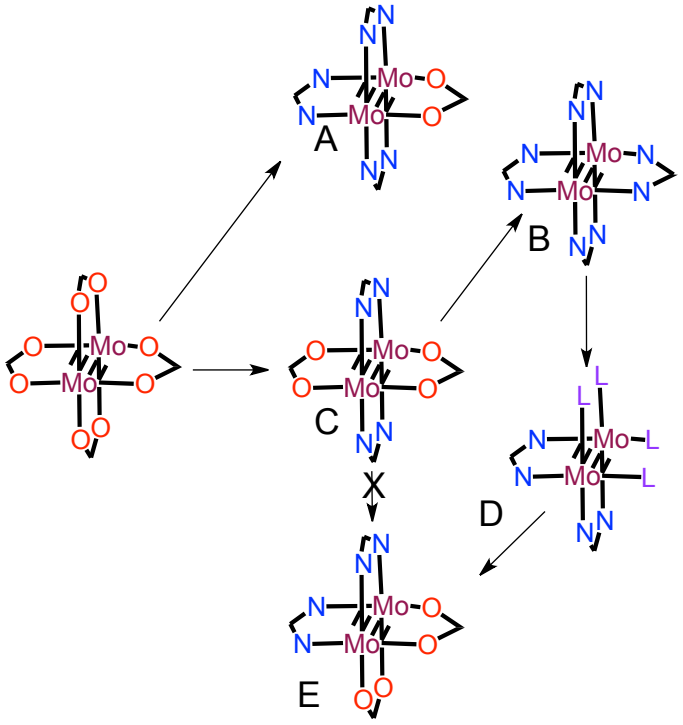

Figure 3.2: Synthetic strategy for the assembly of different bimetallic Mo units.

3.2 Results And Discussion

Before synthesizing a fullerene extended network containing M^*_2 units, we started the synthesis of discrete units of fullerene derivatives. We used the synthetic strategy described before (figure 3.2), starting from $(Mo_2(O_2CCH_3)_4$ to synthesize discrete units of fullerene derivatives, ranging from one to four fullerenes in the bimetallic assembly, see figure 3.3. For example, starting from compound **22**, $(Mo_2(O_2CCH_3)_4$, we can synthesize the bimetallic assembly **C** followed by substitution of the acetates with a fullerene carboxylate ligand, **21**, resulting in structure **23**. We are particularly interested in the study of the electronic coupling between the bimetallic unit and the fullerene cage, and between two different fullerene cages

through the bimetallic unit.

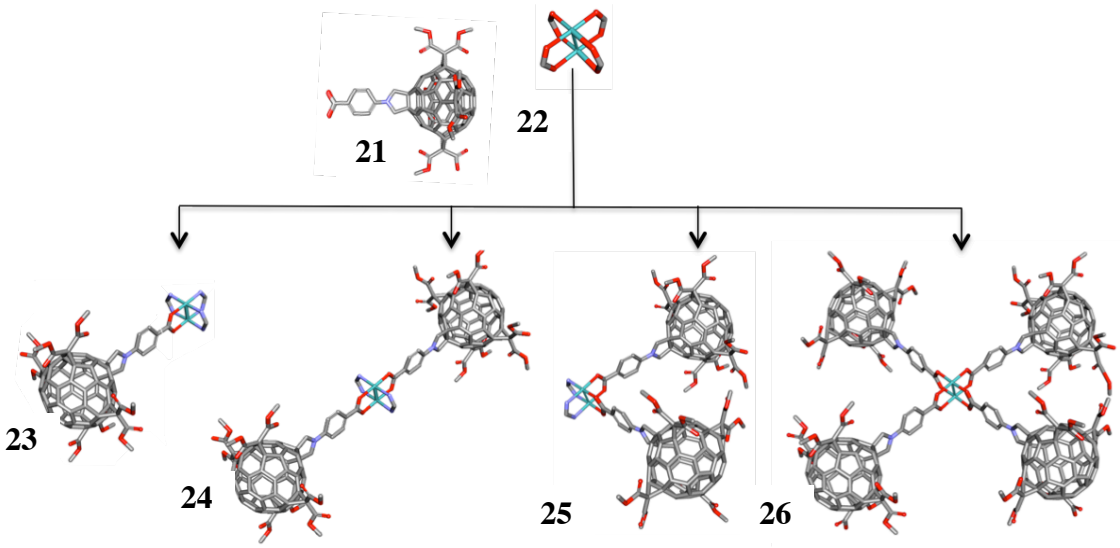

Figure 3.3: Discrete molecular systems of fullerene derivatives with secondary building units.

We decided to start with the synthesis of compound **29**, figure 3.4. The reaction was done under an inert atmosphere to prevent the decomposition of the dimetallic unit and to avoid the formation of tetradanif (**B,** figure 3.2). As carboxylates can be replaced by formamidinates, the presence of oxygen accelerates the conversion of the trisdanif (Bimetallic assembly **A**, figure 3.2 to tetradanif (Bimetallic assembly **B**) lowering the reaction yield. A red powder was obtained from the reaction shown in figure 3.4.

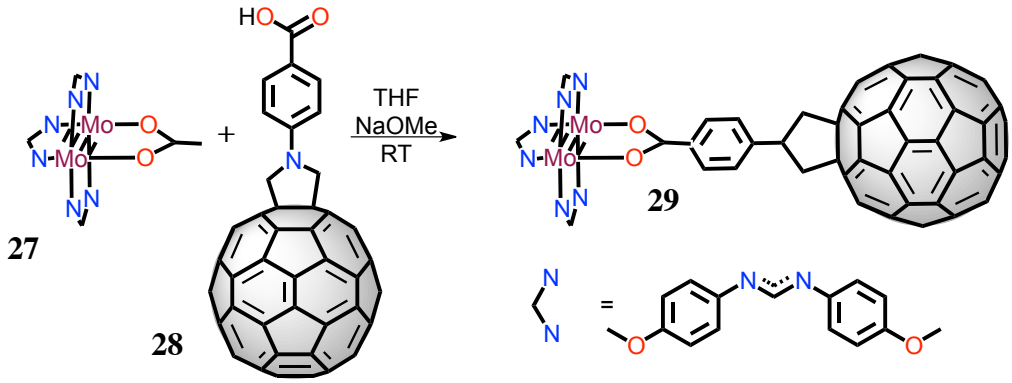

Figure 3.4: Discrete molecular systems of fullerene derivatives with secondary building units.

Using ^{1}H-NMR, figure 3.5, we were able to identify different resonances that correspond to compound **29**. There are two singlets at 8.38 ppm and 8.0 ppm that correspond to the protons of the formamidinate. Additionally, there are two singlets at 3.79 ppm and 3.61ppm that correspond to the methoxy protons of the Danifs. The signal at 3.90 ppm corresponds to the protons from the pyrrolidine of the fullerene derivative. Although there are two multipltes (7.41 ppm and 7.17 ppm) that could not be assigned to compound **29**, they are not from Danif nor from Tetradanif suggesting that all the starting material was consumed and those signals correspond to an impurity.

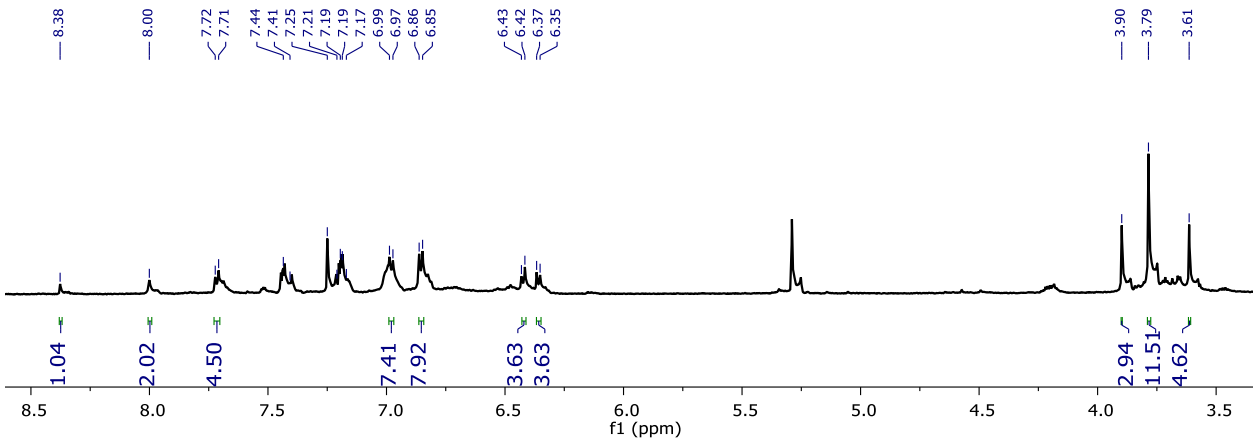

Figure 3.5:^{1}H-NMR of compound **29**.

In the MALDI-MS spectrum of the reaction crude we were able to identify the molecular peak of the desired product (1840). The isotopic distribution of the peak at 1840.872 corresponds to the computed isotopic distribution of compound **19** as shown in figure 3.6.

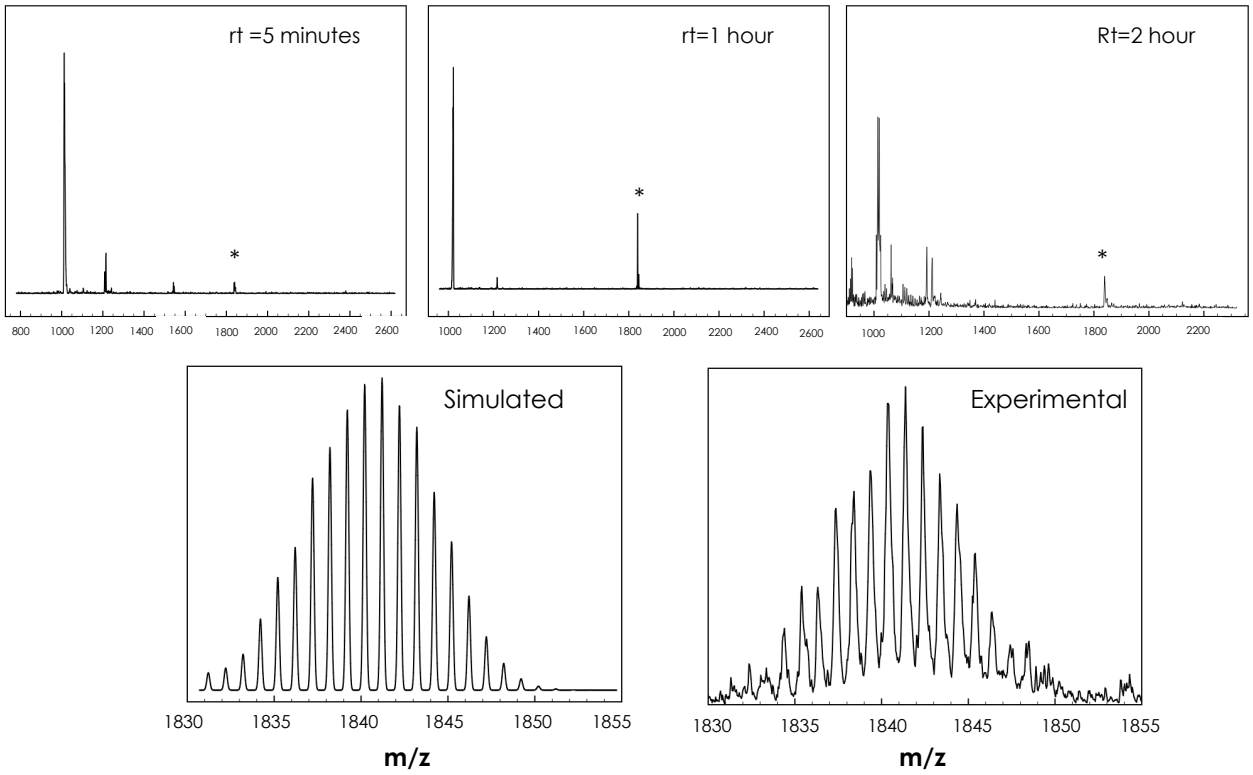

Figure 3.6: MALDI-TOF spectrum of the reaction crude after 5 minutes, 1 hour and 2 hours. The calculated and experimental isotopic distributions for the products are shown on the bottom part of the figure.

The UV-spectra for compounds **27**, **28** and **29** are shown in figure 3.7. The UV-spectrum for compound **27** shows the characteristic band for fullerenes *mono*-adducts at 430 nm. For both compounds, **28** and **29,** the UV-spectrum shows the $\delta \rightarrow \delta^*$ transitions at 445 nm and 420 nm, respectively.

After purification of the red powder by column chromatography, three different fractions were collected, F1, F2 and F3. The MALDI-TOF MS spectrum of each fraction shows a peak at 1840; however, the spectra for F2 and F3 show peaks corresponding to higher masses than 1840 which may correspond to the formation of molybdenum dimers or to compounds that result from the attack of one danif on the fullerene cage, see figure 3.8. Red crystals were obtained from F1, however, the diffraction of the crystal was too weak to resolve the structure.

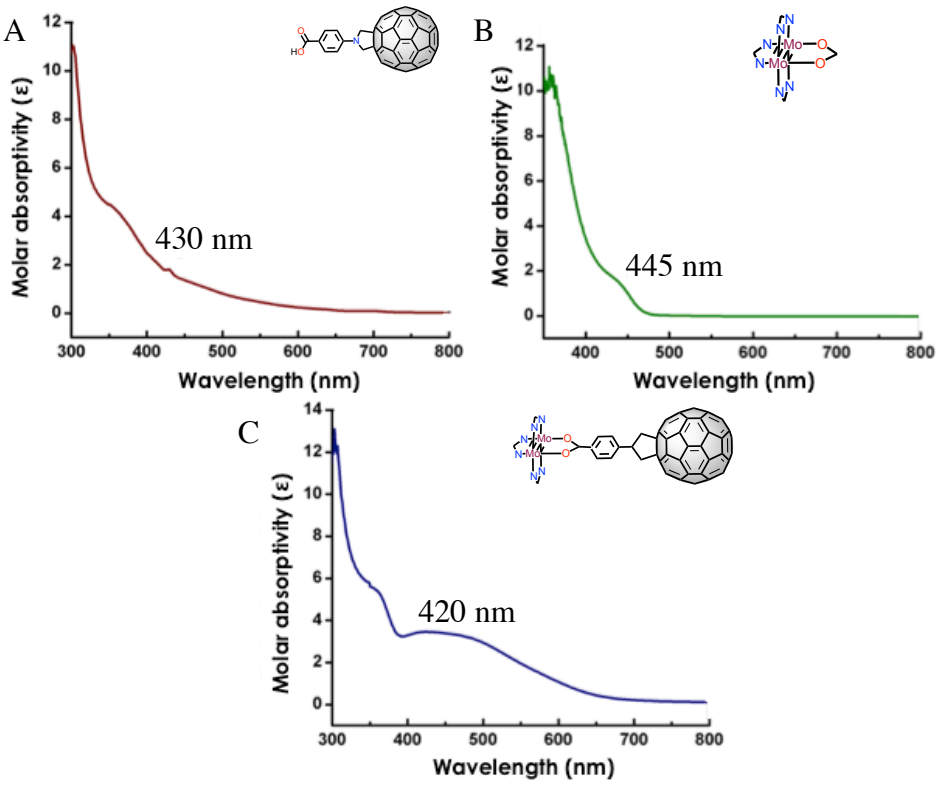

Figure 3.7: UV-vis spectra of a) compound **28**, b) compound **27** and c) compound **29.**

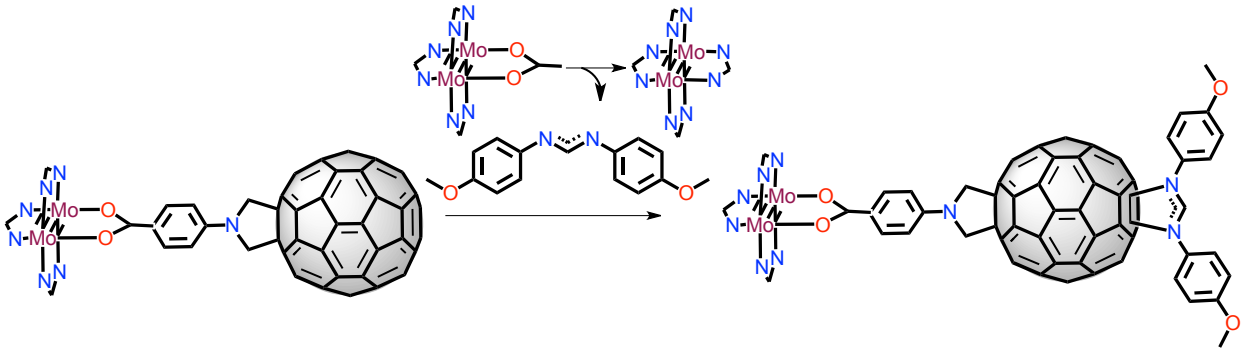

Figure 3.8: Danif attack to the fullerene cage of the bimetallic complex.

3.3 Future Work

We will finish the characterization - electrochemistry, UV-spectrum, NMR- and crystallization of compound **29**. Additionally we will synthesize compounds **23**, **24** and **25**. We plan to change the fullerene mono carboxylate for the fullerene *trans*-**1** dicarboxylate (**16**) to form extended networks as shown in figure 3.9.

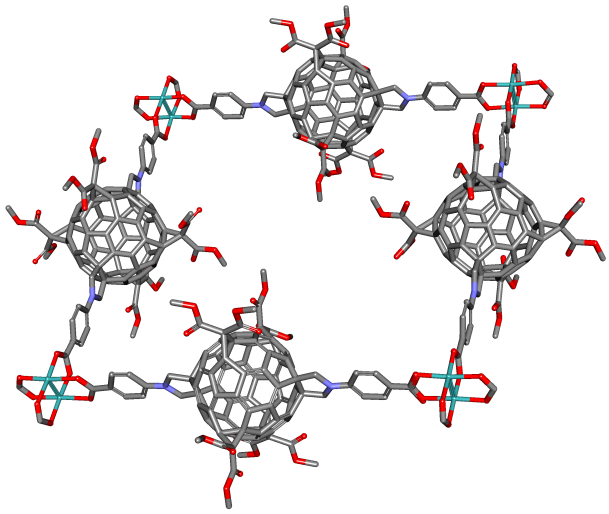

Figure 3.9: Dimolibdenum-fullerene extended network.

Metals are not only used to form fullerene based supramolecular architectures, dimetallic units, metal clusters or single metals can be encapsulated inside different fullerene cages, constituting what is known as endometallofullerenes (EMFs). On the other hand, metals can also be attached to the fullerene cage as exohedral clusters to modify the properties of the pristine fullerenes. Both endohedral metallofullerenes and exohedral clusters on fullerenes will be described in chapter 5 and chapter 6, respectively.

3.4 Experimental Section

Synthesis of compound 28.

The general procedure for a 1,3-dipolar cycloaddition was followed. C_{60} (50 mg, 0.07 mmol) was added to a three-neck flask along with **16a** (75 mg, 0.2 mmol). The mixture was dissolved in *o*-DCB and sonicated for 5 minutes. The solution was left under reflux for 4 hours. ^{1}H-NMR (400 MHz, THF-d_8) = 10.64 (s, 1H), 8.12 (d, J = 8.2 Hz, 2H), 7.46 (d, J = 7.4 Hz, 2H), 3.28 (s, 4H); MALDI-TOF MS: calcd. 883.124[M^+], found 883.108[M^+] For further experimental details please see the experimental section in chapter 4.

Chapter 4: 1,3-Dipolar Cycloadditions to Fullerenes

4.1. INTRODUCTION

Compound **28** (figure 3.4) was synthesized via an unconventional 1,3-dipolar-cycloaddition reaction. In this chapter we review the different methodologies for the synthesis of N-fulleropyrrolidines and we present an unprecedented synthetic pathway.

4.1. 1. 1,3-dipolar cycloaddition

As mentioned before, the functionalization of C_{60} is a well-established field that began in 1990, as soon as macroscopic quantities of the fullerenes became available.[6] Multiple strategies can be and have been used to add different groups. One of the most common reactions for the functionalization of fullerenes is the 1,3-dipolar cycloaddition due to its versatility and relatively good yields.[83-85] Among the fullerene derivatives synthesized via 1,3-dipolar cycloaddition reactions, fulleropyrrolidines have gained special attention due to their potential application in the synthesis of new materials, construction of supramolecular architectures (as explained in chapters 2 and 3) and potential biologically active compounds.[86] Pioneering work on the functionalization of fullerenes was done by Prato and coworkers through the reaction of fullerene (C_{60}) with azomethine ylides generated in situ to form fulleropyrrolidines.[83] Typically, an aldehyde/ketone reacts with a α-amino acid and C_{60} under reflux in toluene or *o*-dichlorobenzene (o-DCB). The latter methodology presents different limitations: its application is limited to either natural amino acids or to those that can be easily synthesized, the control of the chirality in the final product, the insolubility of amino acids in low polarity solvents where fullerenes can be dissolved and the yield of the reaction commonly ranges from 25-45%.[87-88]

After Prato and co-workers first reported the formation of fulleropyrrolidines, different pathways and methodologies have been extensively studied.[83, 87, 89-97] Different strategies have been used to increase the yields of the reactions, decrease the reaction times, avoid decomposition of different species, increase the stereoselectivity of the reactions, avoid the use

of harmful reagents and increase the environmental friendliness of the synthetic methodologies. Masooni *et al* recently reported the synthesis of N-benzyl fulleropyrrolidines under microwave and solvent free conditions. The reactions showed a decrease in the decomposition rates of the substrates and products, high yields and enhanced reaction rates and environmental friendliness.[92] Commonly, when microwave irradiation is used to synthesize N-fulleropyrrolidines, besides the amino acid, an aldehyde is used. In the search for simplification of the synthetic methodologies and higher reaction yields, direct reactions between different amino acids and C_{60} have been explored. Gan's group has explored direct reactions between C_{60} and different α-amino acid esters induced by photoirradiation or in the presence of different iodo reagents under ultra-sonication reactions.[98-99] The synthesis of fulleropyrrolidines can also be achieved by direct thermal reactions between α-amino acids and amino acid esters in the absence of aldehyde.[93-94, 100] In this case the aldehyde is generated in-situ through and uncommon C-N bond cleavage. The aldehyde reacts with either the amino acid or the amino acid ester to form the ylide, followed by a 1,3-dipolar cycloaddition.[93, 98]

Compared to the extensive application of amino acids and their derivatives in 1,3-dipolar cycloadditions, to our knowledge there are no reports of direct thermal reactions between N-substituted imidinoacetic acids and C_{60}. Herein we report the direct thermal reaction between both N-pyridine imidinoacetic acid and N-(4-carboxyphenyl)-imidinoacetic acid with C_{60} in the absence of aldehydes to synthesize N-fulleropyrrolidines (figure 4.1). We compare the reaction yields obtained under standard 1,3-dipolar cycloaddition conditions to the yields obtained under the proposed new synthetic conditions. Moreover, we have gained mechanistic insights about these reactions deduced from isolated intermediates.

4.2 Results And Discussion

We functionalized C_{60} with both pyridine and carboxylic acid containing addends (See figure 4.1) via a conventional 1,3-dipolar cycloaddition for potential application in the

construction of supramolecular architectures; it is well known that both pyridines and carboxylic acids can easily form complexes with different metals as Cu(II) and Zn(II).

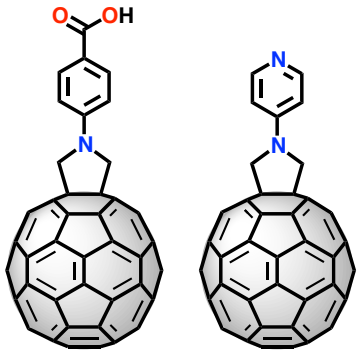

28 **30**

Figure 4.1. Chemical structures of C60-monoadducts synthesized via 1,3-dipolar cycloaddition with terminal carboxylic acid and pyridine groups.

N-substituted glycines easily react with paraformaldehyde, followed by decarboxylation to form an ylide. The ylide reacts with the C_{60} cage via a 1,3-dipolar cycloaddition. The synthesis of the N-substituted glycines **6** and **7** was achieved via a condensation reaction between the corresponding amine (**3a** and **3b)** and ethyl bromoacetate in *N.N*-Dimethylformamide (DMF), followed by the hydrolysis of the ethers (**4** and **5**) with hydrochloric acid using dioxane as the solvent, see scheme 1. The identity of compounds **6** and **7** were confirmed using ^{13}C-NMR and ^{1}H-NMR (see SI, Figure 1). Surprisingly, compounds **5a** and **5b** were byproducts in the synthesis of compounds **4a** and **4b,** respectively**.** The N-substituted imidinoacetic acids, **8** and **9,** were obtained in a similar way as the N-substituted glycines **6** and **7,** through the hydrolysis of the corresponding ester, **5a** and **5b.**

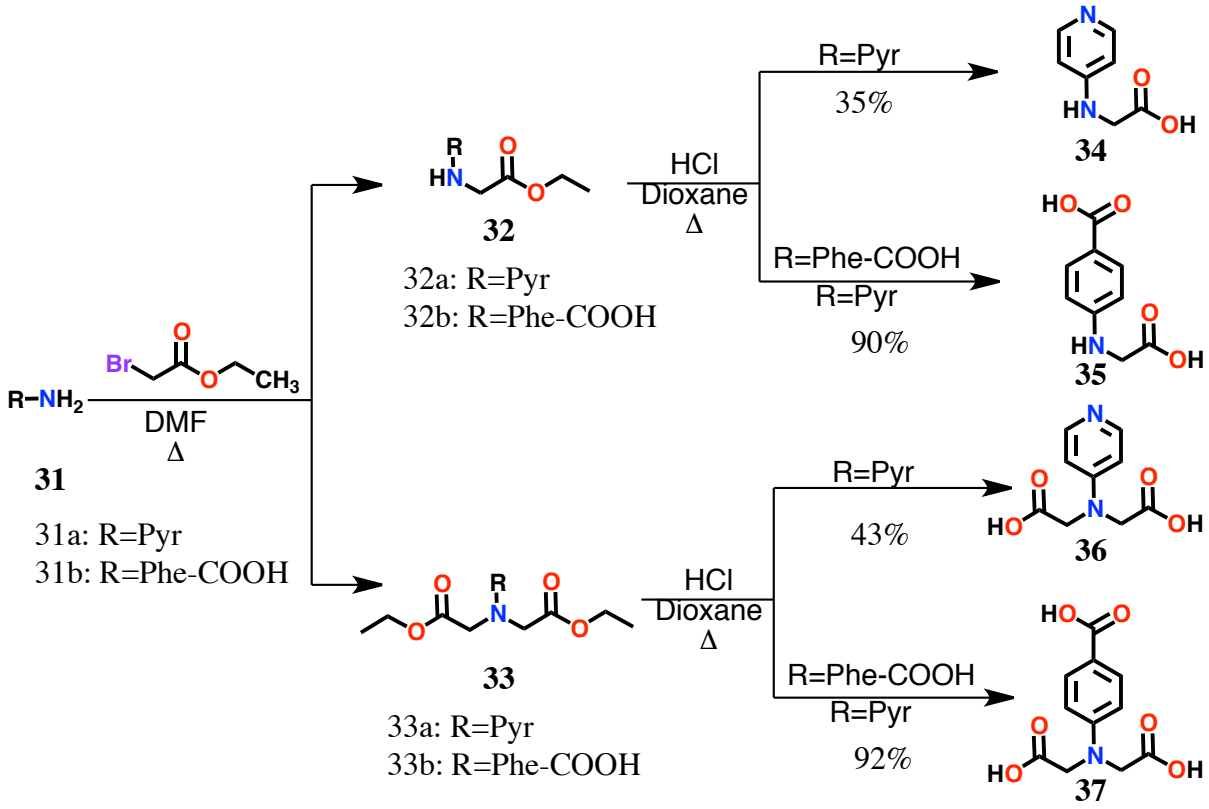

Figure 4.2. **.** Syntheses of N-substituted glycines **34**-**37** through reactions of primary amines **31a** and **31b** with ethyl bromoacetate followed by the hydrolysis of compounds **32** or **33.**

As shown in table 4.1, we modified the reaction conditions to enhance the synthesis of both compounds **32a** and **32b**, or compounds **33a** and **33b.** When 1.5 equivalents of ethyl bromoacetate reacted with compound **31a** for 4 hours, compound **32a** was obtained in a 67% yield (Table 4.1, entry 1) while compound **33a** was obtained in a 21% yield (Table 4.1, entry 4). The yield of compound **33a** was higher (82% - Table 4.1, entry 6) when 4 equivalents of ethyl bromoacetate instead of 1.5 equivalents were reacted with compound **31a** and the reaction was allowed to proceed for a longer time (24 hours). In a similar way, we modified the conditions to either enhance the synthesis of compound **32a** or compound **33a.** The identity of compounds **32a, 32b, 33a,** and **33b** was confirmed by ^{13}C-NMR and ^{1}H-NMR, see the experimental section.

Table 4.1. Conditions and product yields for the reactions between primary amines, 3a and 3b, and ethylbromoacetate.

Entry	Amine	Product	Equivalents[a]	Time [h]	Yield [%]
1	**31a**	**32a**	1.5	4	67
2	**31a**	**32a**	2.0	4	42
3	**31a**	**32a**	4.0	24	10
4	**31a**	**33a**	1.5	4	21
5	**31a**	**33a**	2.0	4	43
6	**31a**	**33a**	4.0	24	82
7	**31b**	**32b**	1.5	4	72
8	**31b**	**32b**	2.0	4	48
9	**31b**	**32b**	4.0	24	7
10	**31b**	**33b**	1.5	4	12
11	**31b**	**33b**	2.0	4	45
12	**31b**	**33b**	4.0	24	90

[a] Equivalents of ethyl bromoacetate with respect to the primary amine.

For the conventional synthesis of N-fulleropyrrolidines **30** and **28** (figure 4.3)**,** the N-substituted glycine (compound **34** or **35**) and C_{60} were dissolved in 1,2-Dichlorobenzene (*o*-DCB) and sonicated for 10 min. Paraformaldehyde was added to the mixture and the reaction was left under reflux, see Scheme 4.3. The reaction was monitored using thin layer chromatography (TLC) and was stopped when poly-adducts were identified by TLC. Compound **1** is a reported compound and its identity was confirmed by comparing its spectral data with those reported previously. As for the new compound **2,** its structure was fully characterized by MALDI-TOF spectrometry, ^{1}H-NMR, ^{13}C-NMR and UV-vis spectra (See experimental section). The UV-vis spectrum shows a band at 430 nm typical of C_{60}-monoadducts (figure 3.7a). The ^{1}H-NMR spectrum shows two doublets at 8.04 and 6.96 ppm that correspond to the aromatic protons. Additionally, the ^{1}H-NMR shows that compound **2** is symmetric and the addition occurs on a 6,6-bond as there is only one singlet at 3.23 ppm that integrates for the four protons of the pyrrolidine ring. The cyclic voltammogram, figure 4.3, shows six irreversible reductions.

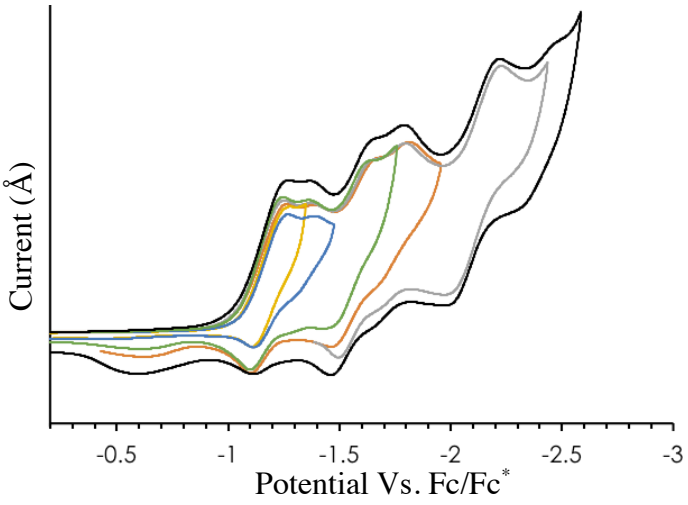

Figure 4.3. Cyclic voltammogram of compound 28 in o-dichlorobenzene (0.05 M (n-Bu)4NPF6; scan rate 100 mV/s for CV)

We used different equivalents of N-substituted glycines, **34** and **35**, in the reaction with C_{60} to yield N-fulleropyrrolidines **30** and **28** (See Table 4.2)**.** The reaction yields in the synthesis of N-(4-carboxyphenyl)-fulleropyrrolidine (**28**) were higher than the yields observed for N-pyridine fulleropyrrolidine (**30**) due mainly to the solubility of the compounds because N-(4-carboxy)imidinoacetic acid (**35**) is slightly more soluble in *o*-DCB than N-pyridine imidinoacetic acid (**34**)**.** The reaction yield for the synthesis of N-pyridine fulleropyrrolidine (**30**) increased as we added more equivalents of the N-Pyridine glycine (**34** – Table 2.4, entries 1-3). The maximum yield of 28% was achieved when three equivalents of compound **34** were added; see entry 3 in table 2.4. As entries 4 and 5 in table 2.4 show, when 4 and 5 equivalents of compound **34** were added, the yields were 21% and 25%, respectively. This suggests that once more than three equivalents of compound **34** are added either the solution is saturated or the formation of *poly*-adducts is favored. In the synthesis of N-(4-carboxyphenyl)-fulleropyrrolidine (**28**) under standard 1,3-dipolar cycloaddition conditions a similar trend was observed. As we increased the number of equivalents of N-(4-carboxyphenyl)-glycine (**35**), the yields of the reaction increased (Table 2, entries 6-10). As table 2 shows, higher yields were obtained for the synthesis of

compound **35** than for the synthesis of compound **34** due to the solubility of both N-substituted-glycines (**34** and **35**) and their different electronic properties. Opposite to what happened with the synthesis of N-pyridine fulleropyrrolidine, when more than 3 equivalents of N-(4-carboxyphnyl)-imidinoacetic acid (**35)** were added to the reaction mixture, high yields were obtained for the reaction, 86% and 90%. These yields are higher than the ones that are commonly reported for 1,3-dipolar cycloaddition which range from 25% to 45%.

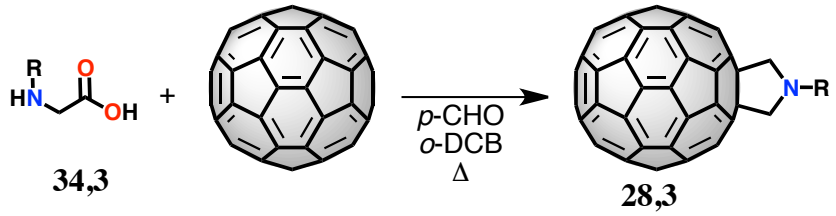

34,3 **28,3**

34: R=Pyr
35: R=Phe-COOH

28: R=Pyr
30: R=Phe-COOH

Figure 4.4. Synthesis of N-substituted fulleropyrrolidines **28** and **30** through a 1,3-dipolar cycloaddition in the presence of paraformaldehyde.

Table 4.2. Reaction conditions and product yields for the reactions between compounds **34** or **35** with C_{60}. Paraformaldehyde was added to the reactions.

Entry	Glycine	Product	Equivalents[a]	Time [min][b]	Yield [%]
1	**34**	**28**	1	200	16
2	**34**	**28**	2	200	24
3	**34**	**28**	3	200	28
4	**34**	**28**	4	200	21
5	**34**	**28**	5	200	25
6	**35**	**30**	1	20	34
7	**35**	**30**	2	20	47
8	**35**	**30**	3	20	48
9	**35**	**30**	4	30	86
10	**35**	**30**	5	30	90

[a] Equivalents of glycine with respect to C_{60}.
[b] Time when the first poly-adducts were observed by TLC.

Both N-pyridine fulleropyrrolidine, **28,** and N-(4-carboxyphenyl)-fulleropyrrolidine, **30,** were also synthesized using an unprecedented methodology where N-pyridine imidinoacetic acid (**36**) or N-(4-carboxyphenyl)-imidinoacetic acid (**37**) reacted directly with C_{60} using *o*-DCB as the solvent (see figure 4.5). The results, summarized in table 3, are similar to the ones obtained when C_{60} reacted with N-substituted glycines (**6** and **7**) with the addition of paraformaldehyde. Overall, the reaction yields for the synthesis of compound **30** are higher than the reaction yields for compound **28**. Interestingly, in the case of N-pyridine fulleropyrrolidine (**30**) the yields where directly proportional to the equivalents of N-pyridine imidinoacetic acid (**36**) that were added to the mixture (Table 4.3, entries 1-5), opposite to what happened when N-pyridine glycine (**34**) reacted with C_{60}, where the reaction mixture was saturated after three equivalents of compound **34** were added. This suggests that the substitution of the N-H group for an N-COOH group in compound **34** improved the solubility of the pyridine compound increasing the reaction yield from 25% (Table 4.2, entry 5) to 35% (Table 4.3, entry 5) when five equivalents of the pyridine-containing compound were added (Figure 4.6).

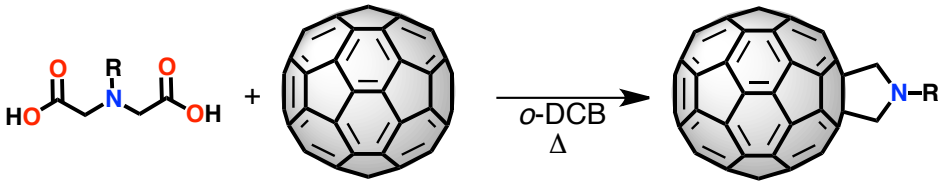

34,35

34: R=Pyr
35: R=Phe-COOH

28,30

28: R=Pyr
30: R=Phe-COOH

Figure 4.5. Synthesis of N-substituted fulleropyrrolidines **28** and **30** through a 1,3-dipolar cycloaddition in the absence of paraformaldehyde.

Table 4.3. Reaction conditions and product yields for the reactions between compounds **36** or **37** with C_{60} without the addition of paraformaldehyde.

Entry	Glycine	Product	Equivalents[a]	Time [min][b]	Yield [%]
1	**36**	**28**	1	260	16
2	**36**	**28**	2	260	17
3	**36**	**28**	3	260	28
4	**36**	**28**	4	260	26
5	**36**	**28**	5	260	35
6	**37**	**30**	1	200	66
7	**37**	**30**	2	200	68
8	**37**	**30**	3	200	75
9	**37**	**30**	4	200	65
10	**37**	**30**	5	200	95

[a] Equivalents of glycine with respect to C_{60}.
[b] Time when poly-adducts were observed by TLC.

Similar reaction yields were obtained for N-pyridine fulleropyrrolidine (**28**) and N-(4-carboxyphenyl)-fulleropyrrolidine (**30**) with both synthetic methodologies where C_{60} reacted with either an N-substituted-glycine or an N-substituted-imidinoacetic acid in the presence or absence of paraformaldehyde. Figure 4.6 shows a comparison of the reaction yields for the conventional 1,3-dipolar cycloaddition method and for the 1,3-dipolar cycloaddition reaction using a N-substituted-imidinoacetic acid as the starting material. The red and blue bars represent the reactions for the synthesis of compound **28** and compound **30,** respectively. The lighter bars show the yields for the reaction of the N-substituted glycine with C_{60} in the presence of paraformaldehyde and the darker bars represent the yield for the reaction between the N-substituted imidinoacetic acid and C_{60} in the absence of paraformaldehyde. The reaction yields when 1 equivalent of either N-pyridine glycine (**35**) or N-pyridine imidinoacetic acid (**37**) was added to the reaction mixture for the synthesis of compound **28** are the same, as the light and dark bars show in Figure 4.6. For the synthesis of compound **30,** the yield of the reaction was higher when C_{60} reacted with 1 equivalent of the N-(4-carboxyphenyl)-imidinoacetic acid (**36**) in the absence of paraformaldehyde than when C_{60} reacted with 1 equivalent of the N-(4-

carboxyphenyl)-glycine (compound **34**) as the dark and light blue bars show in figure 4.6. A similar behavior was observed when 3 equivalents of either the N-substituted-glycine or N-substituted-imidinoacetic acid were added to the reaction for the synthesis of compound **28** or **30.** The only two examples where the reaction yields in the synthesis of N-fulleropyrrolidines, compound **28** or **30,** were higher using the conventional methodology for 1,3-dipolar cycloaddition were (see figure 4.6): when two equivalents of the N-pyridine imidinoacetic acid (**36**) or of N-pyridine glycine (**34**) were used for the synthesis of compound **28,** and when four equivalents of N-(4-carboxyphenyl)-imidinoacetic acid (compound **37**) or of N-(4-carboxyphenyl)-glycine (**35**) were used for the synthesis of the N-(4-carboxyphenyl-fulleropyrrolidine, **30.** Our results show that with the new synthetic methodology different N-fulleropyrrolidines can be synthesized with comparable or higher yields than the conventional 1,3-dipolar-cycloaddition reactions. Additionally, the synthesis of N-fulleropyrrolidines by a direct thermal reaction between C_{60} and an N-imidinoacetic acid does not require the addition of paraformaldehyde, a reagent that represents a risk for the environment and the researcher.

Entries 1-5 in table 4.1 show that the reaction time for the synthesis of N-pyridine fulleropyrrolidine (**28**) under standard conditions was 200 minutes, which is 60 minutes faster than the reaction time when compound **28** was synthesized using N-(pyridine)-imidinoacetic acid, **36** (entries 1-5 in table 4.2). For the synthesis of N-(4-carboxyphenyl)-fulleropyrrolidine (**30**) the difference in the reaction times for both synthetic methodologies is higher than 60 minutes: the reaction time under standard conditions was around 20 minutes (entries 1-5 in table 4.1) while under non-standard conditions it was 200 minutes. Our results suggest that when N-imidinoacetic acids react directly with C_{60} the presence of an extra basic group besides the nitrogen from the N-imidinoacetic acid (e.g. pyridine) enhances the reaction. Hence, the first step of the proposed mechanism involves the deprotonation of one of the carboxylic acid groups (figure 4.7) followed by the cyclization to form a 4-substituted-2,6-morpholinedione, intermediate **IV**. It is known that cyclic anhydrides with 5- and 6-membered rings can be synthesized by heating the appropriate diacid. Additionally, N-methylimidinoacetic acid form 4-

methylmorpholine-2,6-dione when heated. When triethylamine is added to the reaction mixture, the temperature of the reaction is lower, the product is formed faster and the yield is higher. [101-102] We thus conjecture that the formation of the ylide involves the formation of intermediate **IV.**

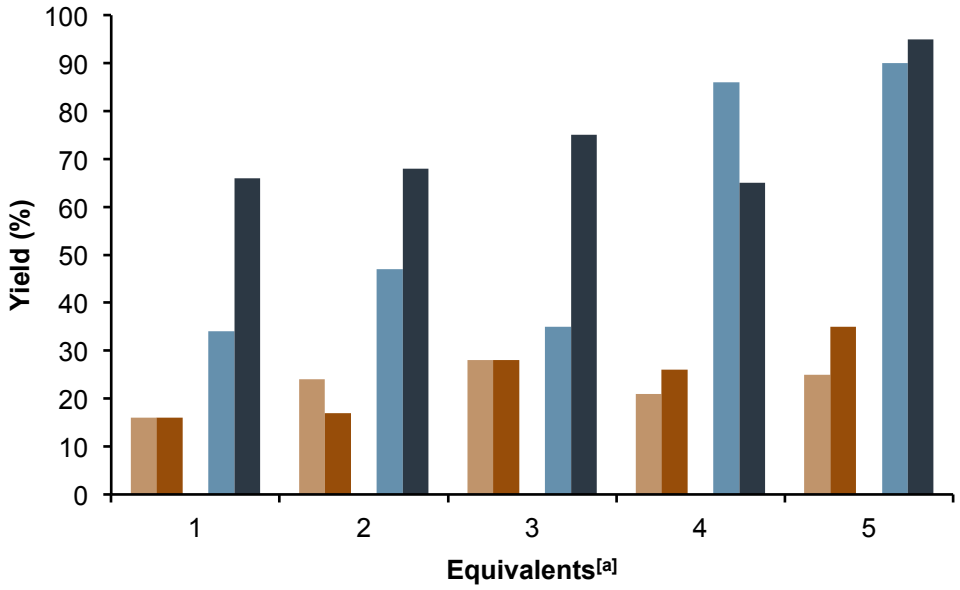

[a] Equivalents of N-substituted glycine, compounds **34** and **36,** (lighter bars) and N-substituted-imidinoacetic acids, compound **35** and **37** (darker bars).

Figure 4.6. Comparison between the reaction yields for the synthesis of N-fulleropyrrolidines, compounds **1** and **2**. The blue bars represent the different methodologies for the synthesis of N-pyridine fulleropyrrolidine (**1**), the lighter bars show the yield when the reaction was done under standard conditions and the darker bars represent the yields when the reaction was done using N-pyridine imidinoacetic acid (**8**). The red bars represents the two different methodologies used for the synthesis of N-(4-carboxyphenyl)-fulleropyrrolidine (**2**), the lighter bars show the yield of the reaction when it was done using the N-(4-carboxyphenyl)-glycine (**7**) and paraformaldehyde. The darker red bars represent the yield of the reaction when it was done using N-(4-carboxyphenyl)-imidinoacetic acid (**9**) as the starting material.

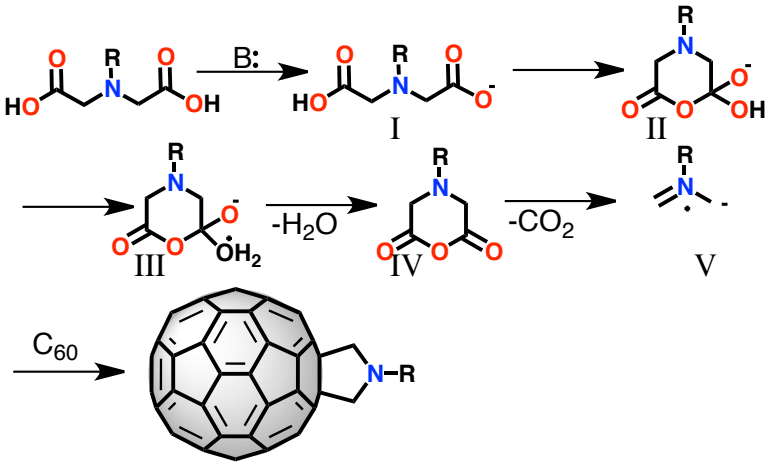

Figure 4.7: Synthesis of N-substituted fulleropyrrolidines **28** and **30** through a 1,3-dipolar cycloaddition in the absence of paraformaldehyde.

Up to now, fulleropyrrolidines have been mainly synthesized via the 1,3-dipolar cycloaddition reactions of azomethine ylides with fullerenes. [87-93, 95-98, 100, 103-108] One of the methods to generate azomethines ylides is the decarboxylation of oxazolidinones.[103] Similar to oxazolidinones, morpholinediones can undergo decarboxylation that results in the formation of the ylides, intermediate **V** in scheme 3. Finally, the ylide reacts with the fullerene cage via a 1,3-dipolar cycloaddition.

To further explore the formation of intermediate **IV** and the effect of pyridine on the reaction mixture, we heated up compound **37** in *o*-DCB in the presence and absence of pyridine as shown in figure 4.8. As expected, the yield of the reaction was higher when pyridine was added to the reaction, similar to what happened for the synthesis of 4-methylmorpholine-2,6-dione when triethylamine was added.[101-102] The reaction was followed by TLC using DCM:1%MeOH as the mobile phase; the Rf of the compound was higher than that for compound **37.** Compound **38** was characterized using ^{1}H-NMR and ^{13}C-NMR (see SI). The ^{1}H-NMR spectrum shows two doublets at 7.97 and 6.66 ppm that correspond to the aromatic protons in the phenyl ring. Additionally, the singlet at 3.06 ppm corresponds to the protons of the methylene.

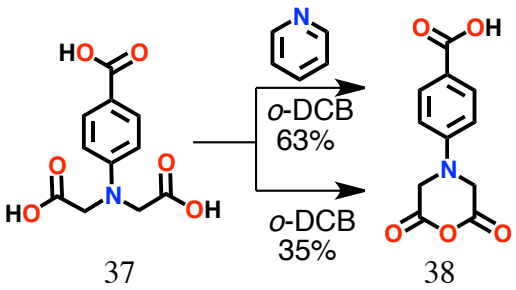

Figure 4.8: Synthesis of 4-(4-carboxyphenyl)-morpholine-2,6-dione under reflux in the presence and absence of paraformaldehyde.

As the addition of pyridine increased the reaction yield of the formation of intermediary **IV**, we hypothesized that the addition of the base to the thermal reaction between N-(4-carboxyphenyl)-imidinoacetic acid (**37**) and C_{60} (figure 4.5) would produce compound **30** in the same or higher yields than the ones shown in table 4.3 with shorter reaction times. As table 4.4 shows, 5 equivalents of compound **37** reacted with C_{60} in the presence of 1-5 equivalents of pyridine. We followed the reaction by TLC and stopped it when we identified *poly*-adducts. The highest yield for the reaction was obtained when five equivalents of pyridine were added to the reaction mixture (Table 4.4, entry 5). Although the reaction time was shorter when pyridine was added to the reaction, the yields were lower when compared to the ones presented in table 4.3. The latter suggests that as the formation of the intermediate is enhanced, its availability to form *poly* adducts is higher, therefore the synthesis of poly adducts occurs faster, limiting the synthesis of *mono*-adducts.

Table 4.4. Reaction conditions and product yields for the reaction between compound **37** and C_{60} with the addition of pyridine.

Entry	Glycine	Product	Equivalents[a]	Time [min]	Yield [%]
1	**37**	**30**	1	120	58
2	**37**	**30**	2	120	52
3	**37**	**30**	3	120	30
4	**37**	**30**	4	120	26
5	**37**	**30**	5	120	92

4.3 CONCLUSIONS

In summary, N-fulleropyrrolidines were effectively prepared by a direct thermal reaction between C_{60} and N-substituted imidinoacetic acids. Although the studied 1,3-dipolar cycloadditions proceed faster under standard conditions, the yields are higher when the reactions are done without the addition of paraformaldehyde using N-substituted imidinoacetic acids. Our results show that one of the key intermediates in the formation of N-fulleropyrrolidines between an N-substituted-imidinoacetic acid and C_{60} is a 4-substituted-2,6-morpholinedione. The reaction between the latter intermediate and C_{60} can be further explored to establish new methodologies for the synthesis of N-fulleropyrrolidines. The successful synthesis of symmetrical N-fulleropyrrolidines without the addition of paraformaldehyde not only provides an environmentally friendly method but it also provides the opportunity to design and synthesize a whole variety of compounds for different potential applications.

4.4 EXPERIMENTAL SECTION

4.4.1 Synthesis

Synthesis of compounds 32b and 33b

Compound **31b** was dissolved in DMF followed by the addition of ethyl bromoacetate. The reaction was left under reflux and it was followed by TLC. The product was purified using flash chromatography with Toluene:EtOAc (4:1) as the eluent. The firs peak collected corresponded to compound **32b** and the second peak corresponded to compound **33b.** Compound **32b -** ^{1}H-NMR (400 MHz, $CDCl_3$)= δ 7.95 (d, J = 8.7 Hz, 2H), 6.59 (d, J = 8.7 Hz, 2H), 4.83 (s, 1H), 4.28 (q, J = 7.1 Hz, 2H), 3.96 (d, J = 1.5 Hz, 2H), 1.32 (t, J = 7.1 Hz, 3H). Compound **33b** - ^{1}H-NMR (400 MHz, $CDCl_3$) = δ 7.99 (d, J = 8.8 Hz, 2H), 6.63 (d, J = 8.8 Hz, 2H), 4.26 (dd, J = 14.2, 7.1 Hz, 4H), 4.21 (s, 4H), 1.31 (t, J = 7.1 Hz, 6H). ^{13}C-NMR (101 MHz, $CDCl_3$=) δ 171.83, 170.00, 152.04, 132.23, 118.35, 111.42, 77.35, 77.03, 76.72, 61.54, 53.36, 14.22.

Synthesis of compounds 35 and 37

A solution of compound **32b** or **33b** was dissolved in a solution of Dioxane/HCl (1:1). The mixture was left under reflux overnight. The solution was then allowed to cool to room temperature until the product crystallized as a light yellow powder. The solid was collected by filtration. Compound **32b -** ^{1}H-NMR (400 MHz, THF) = δ 11.01 (s, 2H), 7.81 (d, J = 8.8 Hz, 2H), 6.61 (d, J = 8.8 Hz, 2H), 3.93 (d, J = 5.2 Hz, 2H). ^{13}C-NMR (101 MHz, THF)=δ 170.88, 166.53, 151.61, 130.91, 118.92, 110.94, 44.16.

Synthesis of compounds 32a and 33a

Compound **31b** together with ethyl bromoacetate was dissolved in DMF. The reaction was left under reflux and was followed by TLC. After completion of the reaction, the product was purified by column chromatography using THF:MeOH as the mobile phase. The first fraction corresponded to compound **33a** and the second fraction corresponded to compound **32a.** Compound **33a -** MALDI-TOF MS: calcd. 266.131[M^+], found 267.566[M^+]. Compound **32a -** MALDI-TOF MS: calcd. 180.093[M^+], found 181.083[M^+].

Synthesis of compounds 34 and 36

A solution of compound **32a** or **33a** was dissolved in a solution of Dioxane/HCl (1:1). The mixture was refluxed overnight. After removal of the solvent, the product was recrystallized from water. The compound was washed with THF and filtered. The solid was left under vacuum overnight. Compound **34 -** ^{1}H-NMR (400 MHz, DMF)=δ 9.49 (s, 1H), 8.76 (s, 2H), 8.37 (d, J = 6.8 Hz, 2H), 7.18 (d, J = 6.8 Hz, 2H), 5.32 (s, 2H). Compound **36 -** MALDI-TOF MS: calcd. 210.063[M^+], found 212.313[M^++ 2H].

Synthesis of compound 28

C_{60} was added to a three-neck flask along with **35** and paraformaldehyde, or along with **37** when we did not use paraformaldehyde. The mixture was dissolved in *o*-DCB and sonicated for 5 minutes. The solution was refluxed until poly-adducts were observed by TLC. ^{1}H-NMR (400 MHz, THF-d_8) = 10.64 (s, 1H), 8.12 (d, J = 8.2 Hz, 2H), 7.46 (d, J = 7.4 Hz, 2H), 3.28 (s, 4H); MALDI-TOF MS: calcd. 883.124[M^+], found 883.108[M^+]

Synthesis of compounds 30

C_{60} was added to a three-neck flask along with **34** and paraformaldehyde, or along with **36** when we did not use paraformaldehyde. The mixture was dissolved in *o*-DCB and sonicated for 5 minutes. The solution was refluxed until poly-adducts were observed by TLC. MALDI-TOF MS: calcd. 840.069 [M^+], found 840.915[M^+]

Chapter 5: Isolation And Characterization Of The Dimetallofullerene $Lu_2@C_{3v}(8)$-C_{82}

5.1 INTRODUCTION

Endohedral fullerenes are fullerene cages with incarcerated species such as, metal clusters, ions or atoms inside the carbon cage (figure 5.1).[109] They can be divided in three groups depending on the encapsulated species: mono-EMFs, di-EMFs and metallocluster-EMFs. Endohedral fullerenes have gained a lot of attention mainly because of their rich electronic properties that make them potential candidates in catalysis, in photovoltaics and biomedicine. The structural, chemical and electronic properties of EMFs are different to those of empty fullerenes due to electron transfer from the metal atoms in the inside of the fullerene to the carbon cages. Understanding the electron transfer from the inside to the carbon cage has lead to extended studies of the electrochemical properties of endohedral fullerenes.[109] Numerous electrochemical studies of EMFs show the diversity of their redox behavior. Many endohedral fullerenes exhibit electrochemically irreversible but chemically reversible reductions. Despite the numerous electrochemical studies the charge transfer mechanisms of endohedral fullerenes still remain poorly understood.[110-111] In this chapter we describe the isolation and characterization of the dimetallofullerene $Lu_2@C_{3v}(8)$-C_{82}.

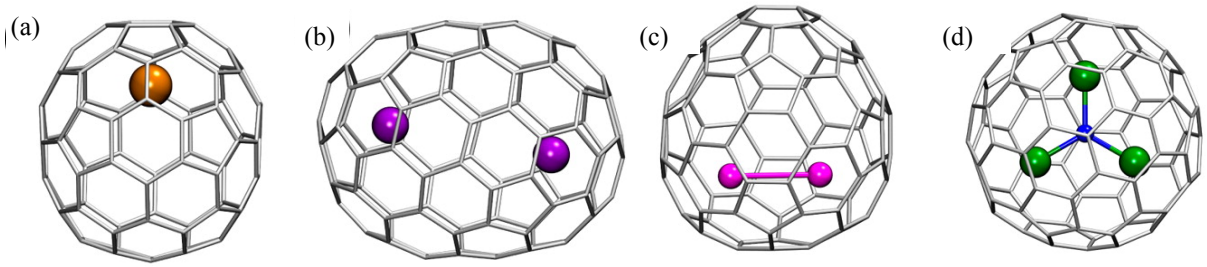

Figure 5.1. Endometallofullerenes. a) $La@C_{82}$-C_{2v} b)$La_2@C_{100}$ c)$Sc_2@C_{82}$ d)$M_3N@C_{80}$

5.1.2 Dimetallofullerenes and carbide fullerenes

Originally, di-EMFs were considered to exist in the form $M_2@C_{2n}$. However, after the identification of the first carbide clusters, it is well known that M_2C_n may exist either as classical di-EMFs – $M_2@C_{2n}$, or as their *corresponding* carbide species $M_2C_2@C_{2n-2}$.[112] The identification

of EMFs as metal carbides or pure metallofullerenes cannot be done using common techniques as mass spectrometry. As a consequence, the family of di-EMFs with an unambiguously determined molecular structure is very limited and detailed electrochemical studies have been performed only for a few di-EMFs which include $M_2@C_{72,78,80}$ (M=Ce and La) and their derivatives.[113-117]

The stability of the di-EMF and the corresponding carbide species depends on the identity of the metal, the location of the LUMO, and the size and symmetry of the cage. Theoretical studies of M_2C_{100} (M=La, Y, Sc) show that in all cases $M_2@D_5(285913)$-C_{100} are the lowest energy species. However, under high temperatures the most stable isomers are the metal-carbide endohedral fullerenes.[112] A similar behavior is observed in the case of Gd_2C_{94}. Although $Gd_2@C_2(153480)$-C_{94} posseses the lowest energy, at high temperatures its molar fraction is extremely low. At higher temperatures, the carbide cluster fullerene species, $Gd_2C_2@D_3(126408)$-C_{92}, $Gd_2C_2@C_1(126390)$-C_{92}, and $Gd_2C_2@C_2(126387)$-C_{92} are stable, suggesting that carbide fullerenes rather than di-EMFs could be easily isolated experimentally.[118]

Electrochemical studies performed on $M_2@C_{82}$ show that most di-EMFs are good electron acceptors as their first reduction potentials range from -0.31to -0.50V and most of them exhibit rather low electrochemical band gaps (less than 1V).[119] Depending on the size and symmetry of the fullerene cage there can be either anodic or catodic shifts in the potentials. $La_2@D_2(10611)$-C_{72} is harder to reduce than $La_2@I_h(7)$-C_{80} by 0.37V, while $La_2@D_{3h}(5)$-C_{78} has an intermediate reduction potential.[109]

$Lu_2@C_{82}$ has been previously identified in MALDI-MS spectra of arcing soots.[120-123] The ultraviolet photolectron spectra (UPS) of $Lu_2@C_{2v}$-C_{82} shows an onset energy of 0.64 eV and it is stated that the metallic cluster donates four electrons to the carbon cage.[123] Moreover, the stability and electronic properties of different isomers of $Lu_2@C_{82}$ have been calculated and the results show that depending on the symmetry of the cage, the number of electrons transferred may vary. $Lu_2@C_{3v}(8)$-C_{82} and $Lu_2@C_s(6)$-C_{82} prefer the hexaanion form while $Lu_2@C_{2v}(9)$-C_{82} prefers the tetraanion form. To date, there are no reports that unambiguously assign Lu_2C_{82} to the

bimetallic endohedral specie or to the corresponding carbide. Additionally, there are no studies on the electrochemistry or photophysical properties of Lu_2C_{82}.

On this chapter we report the preparation and isolation of Lu_2C_{82}, whose structure was determined by a combination of mass spectrometry, electrochemistry, UV-vis absorption spectroscopy and computational studies. We also studied the stability of both the di-EMF $Lu_2@C_{82}$ and the carbide $Lu_2C_2@C_{80}$. Interestingly, in the case of Lu_2C_{82}, both computational and experimental results show that the di-EMFs is more stable than the corresponding carbide compounds.

4.2 RESULTS AND DISCUSSION

The soot containing Lu_2C_{82} was produced by arc discharge vaporization of a Lu_2O_3 packed graphite rod. After extraction with CS_2, the carbon soot was injected into the HPLC for the first stage separation, see Figure 5.2.

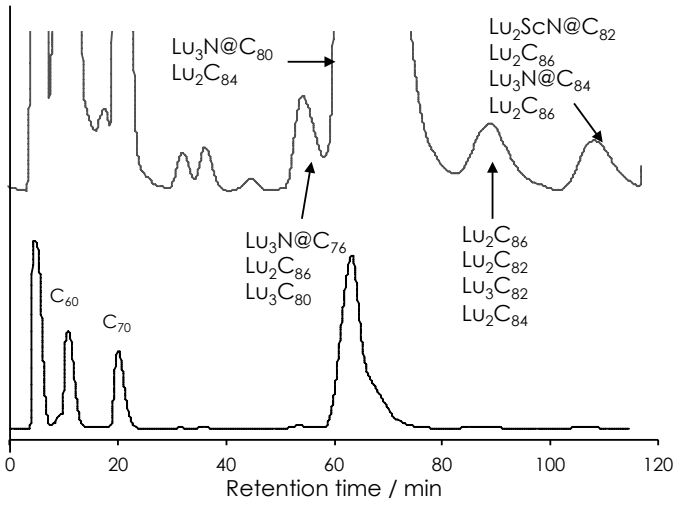

Figure 5.2: HPLC profile of the CS_2 extract containing lutetium EMFs. The top HPLC profile is an expansion of the chromatograms shown in the bottom of the figure. The experiment was done using a 5PBB column, with a flow rate of 5mL/min using toluene as the eluent.

The fraction containing $Lu_3N@C_{80}$ and Lu_2C_{84} was injected for a second stage separation. Only one of the two fractions collected (F1- Figure 5.3) contained pure Lu_2C_{82}.

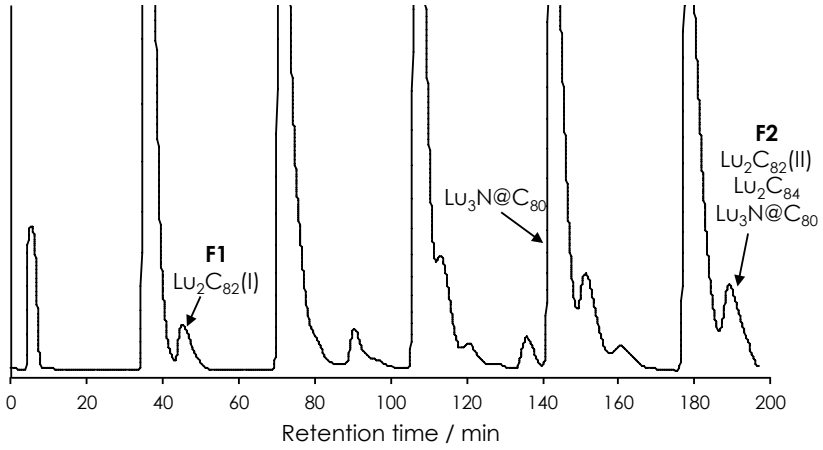

Figure 5.3: HPLC profile of the largest fraction collected from the first step separation. The experiment was done using a Buckyprep column, with a flow rate of 5mL/min using toluene as the eluent.

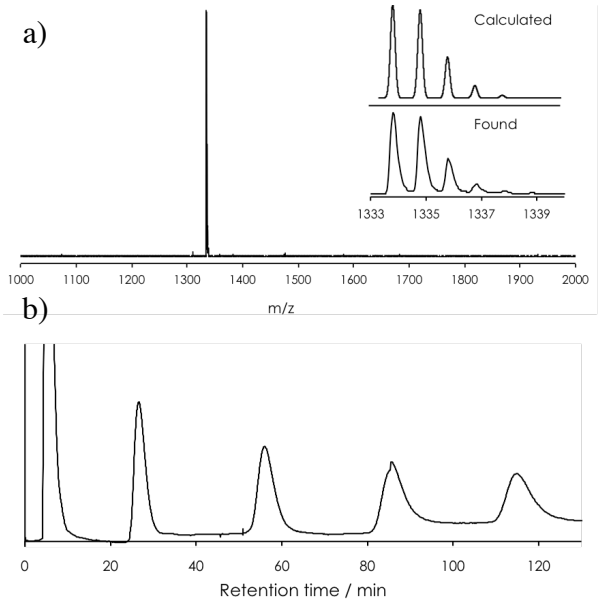

Figure 5.4: a) MALDI-TOF spectrum of Lu2C82. b) Recycling HPLC chromatogram of Lu2C82. The experiment was done using a Buckyprep column, with a flow rate of 1.4 mL/min using toluene as the eluent.

The purity of Lu_2C_{82} was confirmed by HPLC (Figure 5.2). The MALDI-TOF spectrum shows only a peak at m/z=1333.772 which corresponds to Lu_2C_{82}. As shown in Figure 5.4 the observed isotopic distribution agrees with the calculated one. Both computational studies and experimental results are combined to determine the structure and electronic properties of Lu_2C_{82}. In contrast to most empty fullerene cages, endohedral fullerenes do not always obey the isolated pentagon rule (IPR) that requires each pentagon to be surrounded exclusively by hexagons. Thus, for computational studies both cases need to be considered: the IPR and non-IPR cages. It has been shown that both terms (steric and coulomb repulsion) determine the stability of the $C_{2n}^{4-/6-}$ anions. This stability is related to the separation of pentagons which can be measured by the IPSI (Inverse Pentagon Separation Index) rule. The cages with lower IPSI values are the thermodynamically more stable ones.[124] Geometry optimization of C_{82} and C_{80} in their hexa and tetra- anionic states were carried out. The energies and IPSI values were computed for each case followed by the selection of those isomers that show low IPSI values. For example, in the case of C_{82}, isomers 4, 6, 9, 8 and 5 have the lower IPSI values for the hexaanion. However, comparison of the energies obtained for the hexaanions to the energies obtained for the tetraanions show that isomers 8 and 9 are more likely to transfer 4 electrons from the metals to the carbon cage, as a consequence, for isomers 8 and 9 the tetraanion form of the C_{82} cage was used. Once we identified the most stable isomers for each case, we calculated the carbide and dimetallic species using the selected cages.

Table 1 shows the relative energies for the most stable isomer of $Lu_2@C_{82}$ and $Lu_2C_2@C_{80}$. In the case of $Lu_2@C_{82}$, we consider isomer 8, 6 and 9 for the calculations with relative energies (12.3, 16.9 and 0.0 Kcal/mol, respectively). The most stable isomer of $Lu_2@C_{82}$ is followed by isomer 4 with a large gap in relative energy, 42.7 Kcal/mol. This value is large enough to exclude other isomers from further calculations. In the case of $Lu_2C_2@C_{80}$, the calculations fail to converge for isomers 5 and 3 which where the next most stable ones. The

results show that the isomers for Lu_2C_{82} are more stable than those of $Lu_2C_2@C_{80}$ suggesting that the isolated Lu_2C_{82}(I) corresponds to the di-EMF and not to its corresponding carbide.

Table 5.1: Computed energies for the most stable isomers of $Lu_2@C_{82}$ and $Lu_2C_2@C_{80}$

$Lu_2@C_{82}$		$Lu_2C_2@C_{80}$	
Isomer	E / Kcal mol^{-1}	Isomer	E / Kcal mol^{-1}
8	-16666.7	7	-16629.4
6	-16665.2	6	-16637.5

The visible-NIR spectrum (Figure 5.5) shows a clear absorption band at 900 nm which is characteristic of C_{82}(8) cages[119, 125 9,14] providing additional evidence that Lu_2C_2(I) corresponds to $Lu_2@C_{82,}$ in particular, to isomer 8. The optical band gap of 1.18eV is calculated from the absorption onset from the UV-spectrum, 1053.75 nm.

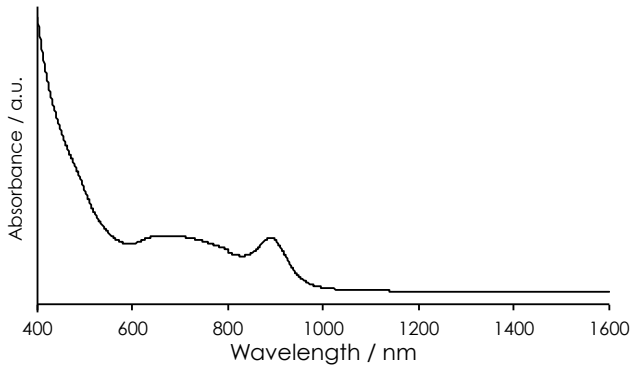

Figure 5.5: UV spectrum of Lu_2C_{82} in $CS_{2.}$

The electronic properties of Lu_2C_{82} are further studied by cyclic voltammetry (figure 5.6). The compound exhibits three irreversible reductions (-1.12, -1.61 and -1.78 V) and one reversible oxidation (+0.48), with a high electrochemical band gap compared to other diEMFs. The first reduction potential resembles that of $Sc_2C_2@C_{3v}$(8)-C_{82}; however, Lu_2C_{82} presents a

higher oxidation potential with a lower HOMO level which has an impact on the donor properties of Lu_2C_{82}.

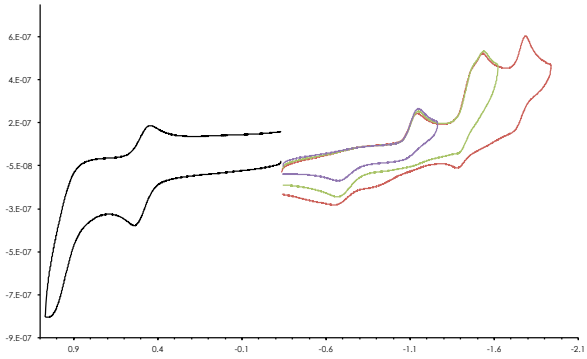

Figure 5.6. Cyclic voltammogram of Lu2C82 in o-dichlorobenzene (0.05 M (n-Bu)4NPF6; scan rate 100 mV/s for CV).

The rather large electrochemical gap is characteristic of the cage when the cage accepts four electrons from the cluster which is supported by DFT calculations, where the tetraanion form of $Lu_2@C_{3v}(8)$-C_{82} has a lower energy than the hexaanion form. It is also known that the C_{82}-$C_{3v}(8)$ isomer is suitable for a four electron transfer due to the low-energy LUMO and LUMO+1 and the higher LUMO +1/LUMO +2 gap.[126] By comparing the UPS spectrum of $Lu_2@C_{2v}$-C_{82} with the one of $Lu@C_{82}$, $Tb@C_{82}$ and $Er@C_{82}$; Hino and co-workers suggest that the electronic configuration of $Lu_2@C_{2v}$-C_{82} is $(Lu^{3+})_2@C_{82}(6)$ showing that the symmetry of the cage has an impact on the electronic properties of the diEMF as previously reported for different diEMF as $La_2@D_{5h}(6)$-C_{80} and $La_2@I_h(7)$-C_{80}.

A charge transfer of 4 electrons to the carbon cage implies that both Lu atoms are in a +2 oxidation state. The lower oxidation state indicates that there is not a complete charge transfer from the metal to the carbon cage, hence the electrons are either localized or they form an intermetallic bond between the two Lu atoms.[127] In the case of $Lu_2@C_{82}$, the large HOMO-LUMO gaps found for the molecule both experimentally and theoretically, is a consequence of a low energy Lu-Lu MO bonding, suggesting that both Lu atoms form a bond. Moreover, the

computed band gap and HOMO LUMO levels of $Lu_2@C_{82}(8)$ are comparable to the values found experimentally, see table 5.2, providing final evidence of the structural identity of Lu_2C_{82}. Interestingly, the case of Lu_2C_{82} is unique as the diEMF is not only more stable than the carbide form but it was easier to isolate and characterize experimentally. Our experimental results in conjunction with theoretical calculations prove the existence of the divalent state of the metal atoms in $Lu_2@C_{82}$.

Table 5.2: HOMO-LUMO levels for isomers 6 and 8 of $Lu_2@C_{82.}$

	Isomer 8	Isomer 6	$Lu_2C_{82}(I)$
HOMO / eV	-5.517	-5.512	-4.74
LUMO / eV	-4.555	-4.906	-3.39
Band Gap / eV	0.964	0.606	1.35

6.3 CONCLUSIONS

For the first time Lu_2C_{82} was isolated and characterized by mass spectrometry, UV-vis NIR and cyclic voltammetry. The experimental results in conjunction with DFT studies unambiguously assign the di-EMF to $Lu_2@C_{3v}(8)$-C_{82} instead of the corresponding carbide. Together, experimental and computational studies show that $Lu_2@C_{82}$ has a high electrochemical bandgap common to C_{82} cages that accept four electrons.

6.4 EXPERIMENTAL METHODS

UV-vis spectra were collected at room temperature using a Varian UV-Vis-NIR Cary 5000 spectrophotometer and CS_2 as the solvent. Mass spectra were obtained using a Bruker microFlex MALDI-TOF spectrometer on reflector positive or negative mode. Electrochemical experiments were performed with a CHI-660A electrochemical workstation in *o*-dichlorobenzene. A conventional three-electrode cell was used: a glassy carbon working electrode, a platinum counter electrode and a silver reference electrode. $(n\text{-}Bu)_4NPF_6$ (0.05M) was used as the supporting electrolyte.

Chapter 6: Exohedral Metallic Clusters On C_{60}

6.1 INTRODUCTION

In previous chapters we described the exohedral functionalization of fullerenes with organic addends. However, as mentioned in chapter 1, fullerenes can also be exohedrally functionalized with inorganic complexes. The content of this chapter was adapted from the paper: *Synthesis and characterization of bis- triruthenium cluster derivatives of an all equatorial [60]fullerene tetramalonate*.[128]

6.1.1 Exohedral complexes on C_{60}

Exohedral metal–C_{60} complexes exhibit unique physicochemical properties which can be tuned by the selection of the metal cluster centers.[129-132] This is important in the study of the reactivity and electrochemical properties of exohedral metal–C_{60} complexes, as it might result in the development of new nanomaterials.[133]

[60]Fullerene is a three-dimensional polyene that offers a variety of possible binding modes for metal centers. For example, several organometallic clusters use the μ_3-η^2,η^2,η^2-C_{60} binding motif. Park et al. reported three tilted isomers of $[Os_3(CO)_6(PMe_3)_3](\mu_3$-$\eta^2$,$\eta^2$,$\eta^2$-$C_{60})$ $[Re_3(\mu$-$H)_3(CO)_9]$ as the 1 : 2 adducts of C_{60} and metal cluster moieties, but the parallel isomer was not observed. Functionalized C_{60} derivatives possess different reactivities from pristine C_{60}, and some of them may be suitable to form parallel complexes. We used the orthogonal transposition method to synthesize a C_{60}-metal complex. Here, we report that compound **39** reacts with triruthenium clusters to form the first parallel-form of the C_{60}–metal cluster complex.

C_{60} reacts with $Ru_3(CO)_{12}$ in refluxing chlorobenzene to afford the face-capping complex $Ru_3(CO)_9(\mu_3$-η^2,η^2,η^2-$C_{60})$ in very low yield.[134] In contrast, when compound **39** reacts with $Ru_3(CO)_{12}$ in refluxing chlorobenzene, the monoadduct complex $Ru_3(CO)_9\{\mu_3$-η^2,η^2,η^2-$C_{60}[C(COOC_2H)_2]_4\}$ (**40**; 21%), and two *bis*-adduct complexes, arbitrarily assigned to *parallel*-$[Ru_3(CO)_9]_2\{\mu_3$-η^2,η^2,η^2-$C_{60}[C(COOC_2H_5)_2]_4\}$, and to *tilted*-$[Ru_3(CO)_9]_2\{\mu_3$-$\eta^2$,$\eta^2$,$\eta^2$-

$C_{60}[C(COOC_2H_5)_2]_4\}$ (*parallel*-3, *tilted*-3; 12%) were formed in 27 minutes. The results are summarized in figure 6.1. This reaction also proceeded in refluxing toluene and o-dichlorobenzene, but the yields of compound **40**, *parallel*-3, and *tilted*-3 were lower.

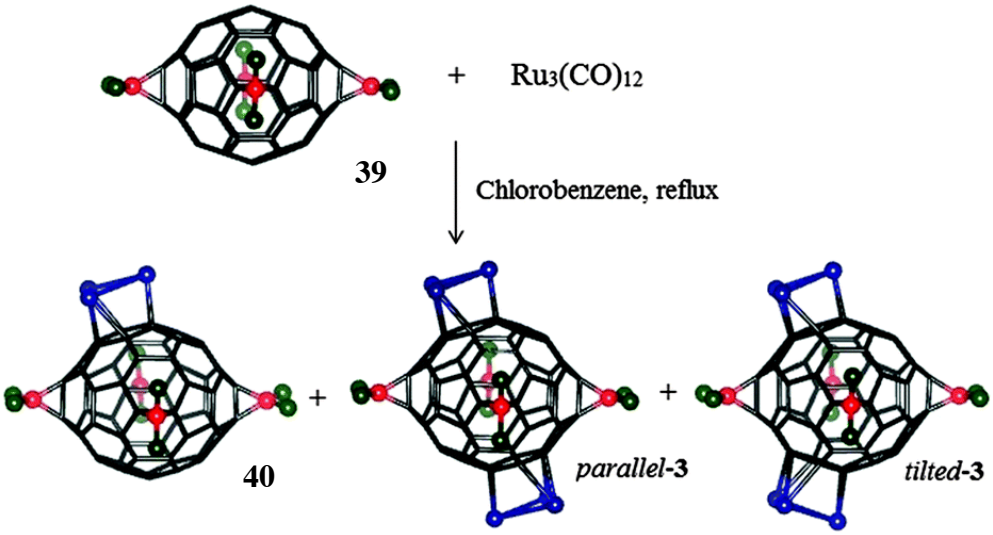

Figure 6.1: Reaction of 39 with Ru3(CO)12. The ethyl formate groups (COOC2H5) are denoted by green balls and the Ru(CO)3 groups are denoted by blue balls.

Compound **40** is an air-stable red solid. The IR spectrum displays several absorption peaks in the range 2073–1980 cm^{-1} for the terminal carbonyl stretches. The ^{1}H-NMR spectrum (figure 6.2) displays multiplets at δ 4.49–4.42 ppm for the methylene protons of the equatorial ethyl malonate groups. Two sets of ABX_3 multiplets centered at δ 4.33 (δ A = 4.36, δ B = 4.29) and 4.21 ppm (δ A = 4.24, δ B = 4.19) for the diastereotopic methylene protons are observed. The ^{13}C resonances for the methylene carbons appear at δ 63.23, 63.20, 63.10 and 62.97 ppm.

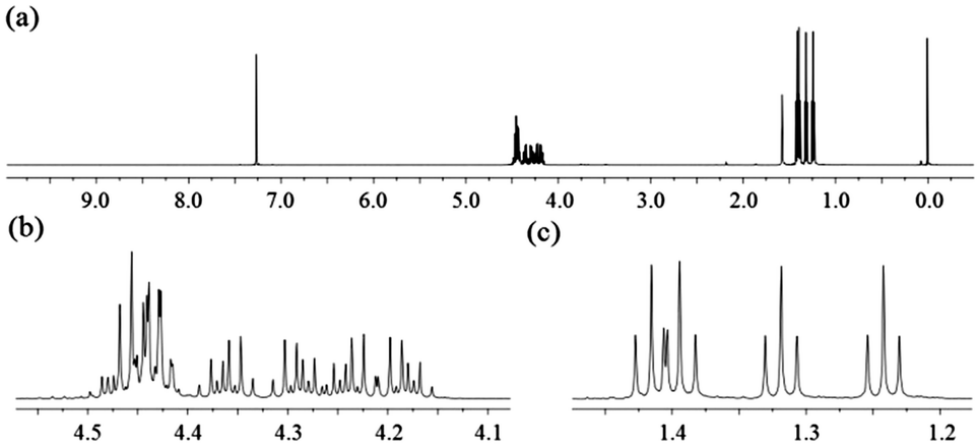

Figure 6.2: (a) 1H NMR spectrum of **40** (600 MHz, $CDCl_3$) and expanded parts: (b) 4.60–4.05 ppm, (c) 1.50–1.15 ppm

Four triplets at δ 1.42, 1.39, 1.32 and 1.24 ppm are observed for the methyl protons (figure 6.2). These features (the equivalency of the protons and carbons of the malonates) clearly indicate a C_s symmetry for **40**, possessing only one plane of symmetry passing through Ru2, C61 and C75 (figure 6.3) There are four different chemical environments for the methyl groups and these are clearly resolved. The integral ratio of the four signals is 1/1/1/1. (figure 6.3) The UV-visible absorption peaks of **40** in CH_2Cl_2 are located at λmax: 242, 283, 314, 466 and 570 nm. The absorptions between 240 and 410 nm are mainly due to $\pi \rightarrow \pi^*$ transitions of the fullerene cage.[135] The bands at ca. 466 and 570 nm could be attributed to the MLCT (metal to ligand charge transfer) transition of the Ru_3 cluster.[136]

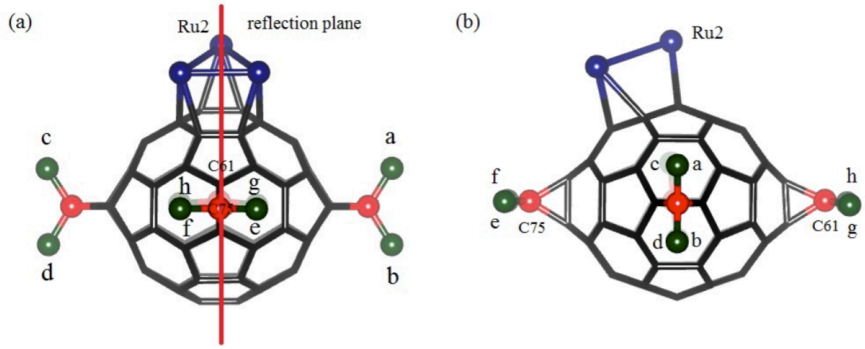

Figure 6.3: (a) Front and (b) side views of the **40** configuration. The ethyl formate groups ($COOC_2H_5$) are denoted by Green balls and the $Ru(CO)_3$ groups are denoted by blue balls.

The recycling HPLC profile for the $[Ru_3(CO)_9]_2\{\mu_3\text{-}\eta^2,\eta^2,\eta^2\text{-}C_{60}[C(COOC_2H_5)_2]_4\}$ mixture clearly shows two peaks in the first cycle, but they are less resolved in the second cycle (figure 6.4) This suggests that we have two isomeric forms, probably the *parallel*-3 and *tilted*-3, that interconvert at room temperature in toluene by changing the coordination sites of the triruthenium clusters on C_{60}.

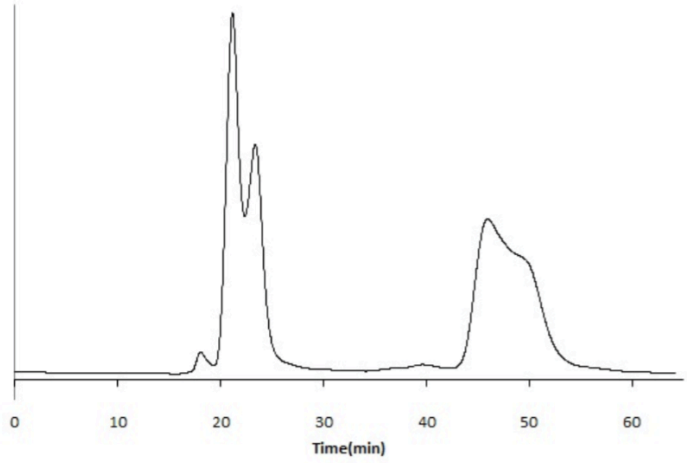

Figure 6.4: HPLC profile shows the first and second cycles in the purification. (Cosmosil Buckyprep column (20 mm x 250 mm), toluene as eluent and flow rate is 1mL/min.

We were unsuccessful in separating *parallel*-3 and *tilted*-3, using either preparative thin-layer chromatography or HPLC (high-performance liquid chromatography). This behavior is similar to the fluxional behavior reported for *cis*-**1**/*cis*-**2** $[Os_3(CO)_6(PMe_3)_3](\mu_3\text{-}\eta^2,\eta^2,\eta^2\text{-}C_{60})[Re_3(\mu\text{-}H)_3(CO)_9]$.[137] The isotope distribution for the molecular ion peaks at m/z 2434 matches a Ru_6 pattern, but its composition is $[1 + Ru_6(CO)_{17}]$. This indicates that a carbonyl group is lost from the compound in the gas-phase before its detection in the mass spectrometer.

Assuming that compounds *parallel*-3 and *tilted*-3 slowly interconvert on the NMR timescale, as suggested by the HPLC results, a total of five different methyl resonances would be anticipated in the ^{1}H-NMR spectrum: two for the *parallel*-arrangement and three for the *tilted*-arrangement, if there are no accidental overlaps. Figure 6.5c clearly shows four different methyl

resonances at δ 1.39 (relative intensity = 1), 1.31 (relative intensity = 2), 1.25 (relative intensity = 4) and 1.20 ppm (relative intensity = 1).

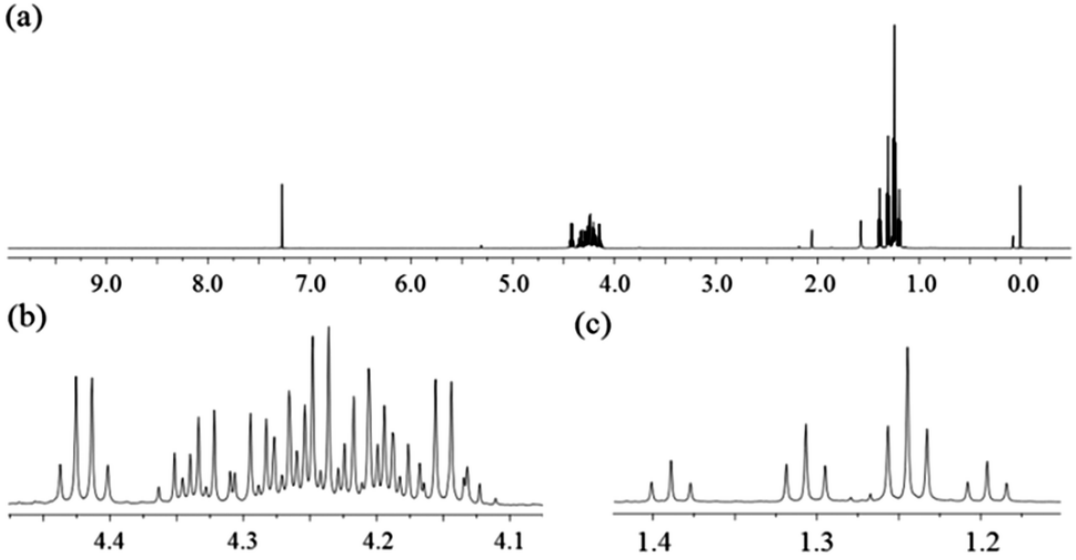

Figure 6.5: (a) ^{1}H-NMR spectrum of mixture *parallel*-3–*tilted*-3 (600 MHz, $CDCl_3$) and expanded parts: (b) 4.45–4.10 ppm, (c) 1.45–1.15 ppm.

Considering that the energy difference between these isomeric species is likely to be very small, see below, a 50 : 50 statistical distribution of isomers would be anticipated. Lowering the temperature to –20 °C (figure 6.6) resulted in the separation of two methyl resonances at 1.24 and 1.23 ppm, derived from the intense room temperature resonance observed at 1.25 ppm.

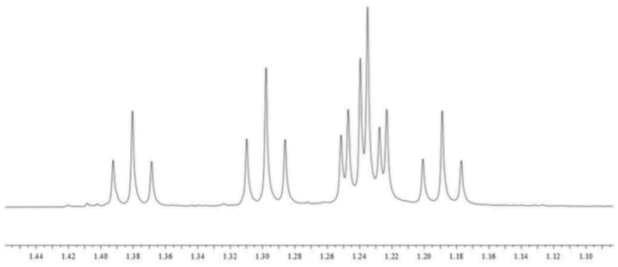

Figure 6.5: Expanded regio of the ^{1}H-NMR spectrum of the mixture *parallel*-3/*tilted*-3 (600 MHz, $CDCl_3$) at -20C.

This leads to the predicted observation of five different methyl resonances and provides additional evidence for the presence of the two slowly interconverting regioisomers in the sample. Upon lowering the temperature it was observed that the resonances at 1.39 and 1.20 ppm retained the same intensities relative to each other as observed at room temperature (1 : 1) but the one at 1.31 ppm was proportionally smaller (1.39 ppm to 1.31 ppm intensities of 1 : 1.5 versus 1 : 2 observed at 25 °C). Given that the environment for methyls 5 and 6 is expected to be very different from that for 7 and 8 (see figure 6.7 for *tilted*-3), we tentatively assign the resonances at 1.39 and 1.20 ppm to isomer *tilted*-3.

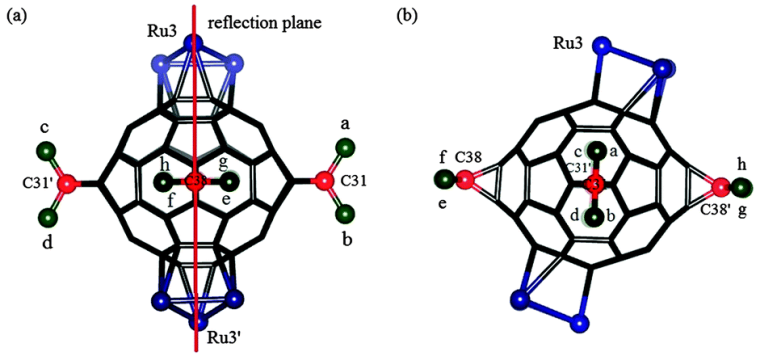

Figure 6.6: (a) Front and (b) side views of the *tilted*-3 isomer. The ethyl formate groups ($COOC_2H_5$) are denoted by green balls and the $Ru(CO)_3$ groups are denoted by blue balls.

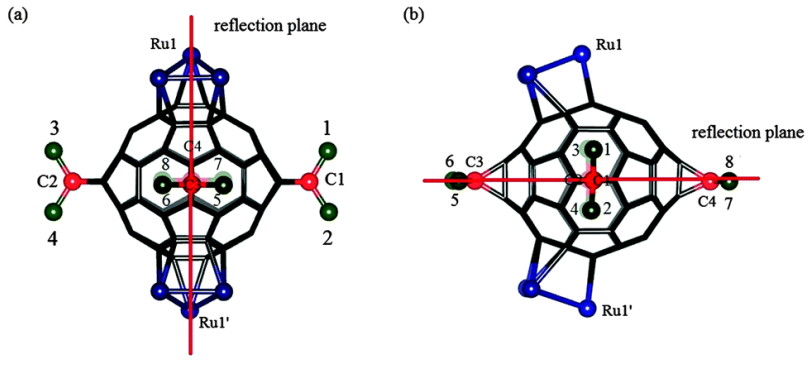

Figure 6.7: (a) Front and (b) side views of the *parallel*-3 isomer. The ethyl formate groups ($COOC_2H_5$) are denoted by green balls and the $Ru(CO)_3$ groups are denoted by blue balls.

Correspondingly, the methyl resonance at 1.31 ppm is assigned exclusively to *parallel*-3 (e, f, g and h in figure 6.7), and that at 1.25 ppm (at 25 °C) contains contributions from both *tilted*-3 and *parallel*-3. Based on these assignments, we measured the equilibrium constants (K_{eq} = *tilted*-3/*parallel*-3, by direct integration of the corresponding signals) as a function of temperature for the interconversion and obtained a value of the thermodynamic $\Delta H = -0.74$ kcal mol^{-1} from a van't Hoff plot. This indicates that there is a very small enthalpy difference between these isomers, with a slight preference for the tilted form. The observed resonances for the methylene hydrogens of the malonates are perfectly consistent with a 50 : 50 *parallel*-3 to *tilted*-3 ratio at room temperature. The ^{1}H-NMR (figure 6.5) and ^{13}C-NMR (Figure 6.6) provide evidence for the C_{2v} symmetry of *tilted*-3 and C_{2h} symmetry of *parallel*-3.

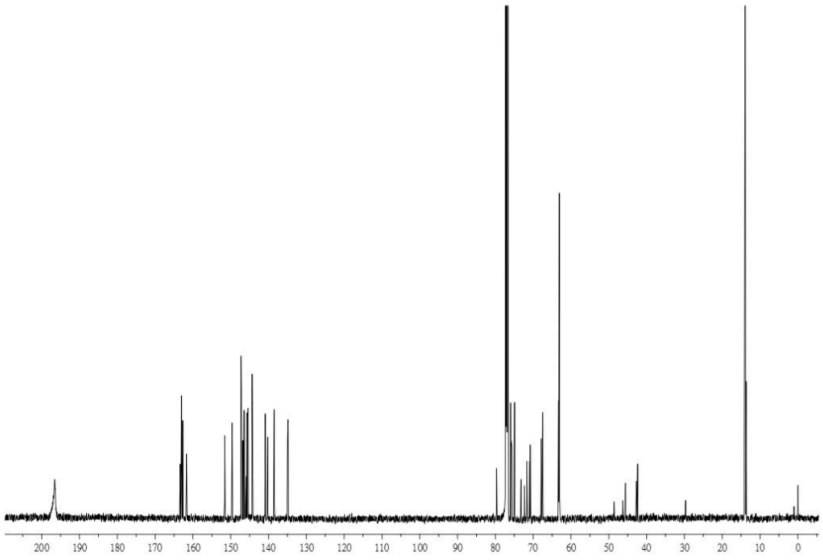

Figure 6.8: ^{13}C-NMR spectrum of mixture *parallel*-3/*tilted*-3.

Density functional theory (DFT) was used to optimize and compute the energies of compounds *parallel*-3 and *tilted*-3. The structures were optimized with the M06 functional and the 6-31G** basis set (def2-TZVP for Ru) using the Gaussian 09 code. The calculated energies for compounds *parallel*-3 and *tilted*-3 (−11.3817 kcal mol^{-1} and −11.3818 kcal mol^{-1}, respectively) are essentially identical, consistent with all observations. However, the fact that the interconverting isomeric forms exhibit time resolved resonances on the NMR timescale indicates

that a reasonably high activation energy must exist, consistent with the multiply bonded metallic clusters on the surface of C_{60} [the Ru-(η_2-C_{60}) bonding energy for $Ru_2(O_2C(3,5\text{-}CF_3)_2C_6H_3)_2(CO)_5(\eta^2\text{-}C_{60})$ has been estimated to be 46.6 kcal mol^{-1}].[138]

Compound **40** was crystallized by slow diffusion of methanol into a dichloromethane solution of the complex. The single-crystal X-ray diffraction study of **40** revealed two independent molecules in the asymmetric unit with no crystallographically imposed symmetry on either molecule. The structure of one of the two very similar molecules of 2 is shown in figure 6.9. The $Ru_3(CO)_9$ unit is placed above a hexagon on the fullerene surface with the ruthenium atoms situated over the three 6 : 6 ring junctions. The structure is similar to that of $Ru_3(CO)_9(\mu_3\text{-}\eta^2,\eta^2,\eta^2\text{-}C_{60})$ and $Ru_3(CO)_9(\mu_3\text{-}\eta^2,\eta^2,\eta^2\text{-}C_6H_6)$.[134 139]

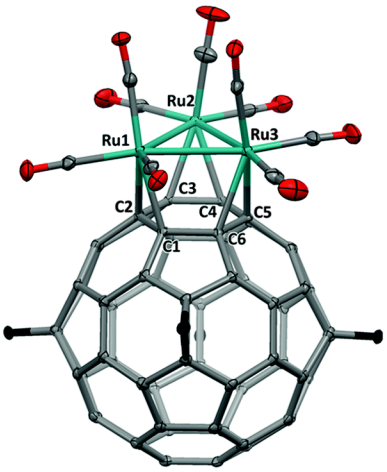

Figure 6.9: A drawing of **39** with 30% thermal ellipsoids and only the methano carbon atoms of the di(ethoxycarbonyl)methano addends shown as black ellipsoids

Crystals of *parallel*-3 were obtained by slow diffusion of methanol into a dichloromethane solution of a mixture of *parallel*-3–*tilted*-3. The X-ray diffraction study shows that there are two half-molecules in the asymmetric unit with the other half obtained by inversion through a center of symmetry. The two molecules are virtually identical in structure. A drawing of one of these is shown in figure 6.7. In both **40** and *parallel*-3, the average Ru–Ru distances

(2.877(3) and 2.876(3) in 2, 2.860(12) Å, and 2.869(7) Å in *parallel*-3), are similar and similar to that in $Ru_3(CO)_9(\mu_3\text{-}\eta^2,\eta^2,\eta^2\text{-}C_{60})$ (2.883(1) Å) and slightly longer than that in $Ru_3(CO)_{12}$ (2.787(1) Å). In both **40** and *parallel*-3, the Ru_3 triangles are almost parallel to the adjacent 6-membered ring (dihedral angle: 2, 1.29° and parallel-3, 1.30°). The occupancy of the $Ru_3(CO)_9$ groups is 0.95 and 0.94 in the two independent molecules; some of compound **40** appears to be substituted for *parallel*-3 in some sites.

6.3 CONCLUSIONS

In summary, *parallel*-3 and *tilted*-3 were synthesized from compound **39** and $Ru_3(CO)_{12}$ by refluxing in chlorobenzene, and these isomers interconvert slowly at room temperature. NMR measurements as a function of temperature allowed the determination of ΔH for the *parallel*-3 → *tilted*-3 isomerization. The experimental value obtained for the thermodynamic enthalpy difference (–0.74 kcal mol^{-1}) is in agreement with the nearly degenerate energies calculated using DFT. Compound *parallel*-3 is the first complex where the two face-capping trinuclear metallic clusters coordinate to C_{60} on opposite sites, in a parallel orientation.

6.4 EXPERIMENTAL SECTION

6.4.1 General methods

All reactions were conducted under an atmosphere of purified dinitrogen using standard Schlenk techniques. All chemicals were obtained from commercial sources and used without further purification. Infrared spectra were recorded on a Bruker Tensor27 IR spectrometer. The NMR spectra were recorded using a JEOL 600 NMR spectrometer. The UV−vis spectrum was recorded using a Cary 5000 UV−vis−NIR spectrophotometer. Matrix-assisted laser desorption ionization (MALDI) mass spectra were recorded on a Bruker Microflex LRF mass spectrometer.

6.4.2 Synthesis

Reaction of compound 39 and $Ru_3(CO)_{12}$

Compound **39** (20 mg, 0.015 mmol) and $Ru_3(CO)_{12}$ (21 mg, 0.033 mmol) were placed in an oven-dried 25 mL Schlenk flask, equipped with a condenser, under a nitrogen atmosphere. Chlorobenzene (10 mL0 was introduced into the flask via a syringe, and the solution was heated to reflux for 20 min. The solution was cooled to room temperature, dried under vacuum, and the residue was subjected to TLC, with dichloromethane as eluent. Compound **39** was recovered in 18% (3.5 mg). Isolation of the material forming a red band afforded two isomers *parallel*-$[Ru_3(CO)_9]_2\{\mu_3\text{-}\eta^2,\eta^2,\eta^2\text{-}C_{60}[C(COOC_2H_5)_2]_4\}$, *tilted*-$[Ru_3(CO)_9]_2\{\mu_3\text{-}\eta^2,\eta^2,\eta^2\text{-}C_{60}[C(COOC_2H_5)_2]_4\}$ (*parallel*-3, *tilted*-3; 11.7 mg, 21%) the second red band afforded $Ru_3(CO)_9\{\mu_3\text{-}\eta^2,\eta^2,\eta^2\text{-}C_{60}[C(COOC_2H_5)_2]_4\}$ (**40,** 8.7 mg, 12%).

Characterization of 40.

MS (MALDI) m/z 1894.94 ($M^+ - O$, ^{102}Ru); ATR-IR ν(CO) 2073 s, 2045sh, 2032 vs, 2010 sh, 1997 br, 1980 br cm^{-1}; ^{1}H-NMR ($CDCl_3$, 20 °C) δ 4.49–4.42 (m, 8H, OCH_2), 4.33 (m, 4H, ABX_3, d A = 4.36, d B = 4.29, JAX = JBX = 7.1Hz,JAB =10.7Hz),4.21(m,4H,ABX_3,d A=4.24,dB=4.19,JAX =JBX =7Hz, JAB = 10.9 Hz), 1.42 (t, 6H, JH–H = 6 Hz, CH_3), 1.39 (t, 6H, JH–H = 6 Hz, CH_2), 1.32 (t, 6H, JH–H =6 Hz, CH_2), 1.24 (t, 6H, JH–H = 6 Hz, CH_3); $^{13}C\{^1H\}$ NMR ($CDCl_3$, 25 °C) d 196.51 (C≡O), 163.73, 163.60, 163.06, 162.96 (C=O), 151.62, 150.72, 147.14, 146. 66, 146.47, 146.38, 145.80, 145.68, 145.38, 145.28, 145.18, 145.01, 144.58, 143.81, 1 43.70, 143.47, 143.41, 142.67, 142.19, 140.05, 140.00, 139.92, 135.66 (C_{60}), 77.92, 75.30, 70.97 (Ru-C_{60}), 72.51, 69.92, 69.81, 69.45, 66.24 (Malonate-C_{60}), 63.22, 63.18, 63.09, 62.96 (OCH_2), 46.69, 44.44, 42.93 (OC-C-CO), 14.12, 13.92, 13.90 (CH_3); UV-vis (CH_2Cl_2): λmax/nm (ε, 103 M^{-1} cm^{-1}) = 570 (6), 466 (18), 314 (76), 283 (102), 242 (166).

Characterization of parallel-3 and tilted-3.

Two isomers were present in the ^{1}H-NMR spectrum in a ratio of 1:1. MS (MALDI) m/z 2439.46 (M^{+} – CO, ^{102}Ru); ATR-IR ν(CO) 2070 s, 2045 sh, 2034 vs, 2004 sh, 1996 br 1982 br cm^{-1}; ^{1}H-NMR ($CDCl_3$, 20 °C) d 4.42 (q, 4H, OCH2, tilted-3), δ 4.31 (m, 8H, ABX_3, d A = 4.33, d B = 4.28, 8H, JAX = JBX = 7.1 Hz, JAB = 10.9 Hz, *parallel*-3), 4.27–4.17 (m, 16H, OCH_2, *parallel*-3/tilted-3), 4.15 (q, 4H, OCH_2, *tilted* -3), 1.39 (t, 6H, CH_3, JH-H = 7.1 Hz, *tilted* -3), 1.31 (t, 12H, CH_3, JH-H = 7.1 Hz, *parallel*-3), 1.25 (t, 24H, CH_3, JH-H = 7.1 Hz, *parallel*-3/*tilted*-3), 1.20 ppm (t, 6H, CH3, JH-H = 7.1 Hz, tilted-3); 13C{1H} NMR (CDCl3, 25 °C) d 196.56 (C ≡ O), 163.36,163.05, 162.99, 162.70, 161.70 (C = O), 151.60, 149.64, 147.30, 147.05, 146.81, 146.45, 146.38, 145.91, 145.72, 145.50, 145.41, 144.34, 141.01, 140.89 (C60), 79.70, 75.98, 75.86, 75.63, 74.93, 73.21, 72.33, 71.69, 70.91, 70.78, 70.69, 67.85, 67.49 (Ru-C_{60}, Malonate-C_{60}), 63.28, 63.19, 63.09 (OCH_2), 48.61, 46.34, 45.59, 42.70, 42.37 (OC-C-CO), 14.10, 13.91, 13.67 (CH_3)

6.4.2 Crystallographic Data

X-ray Crystallography and Data Collection of 40.

Compound **40** was crystallized by slow diffusion of methanol into a dichloromethane solution of the complex. Crystal data for **40**, $Ru_3(CO)_9\{\mu^3$- η_2,η_2,η_2-$C_{60}[C(COOC_2H_5)_2]_4$ (2) (CCDC 1039743). C97H40O25Ru3, M = 1908.50, red plate, 0.066×0.042×0.009 mm, λ = 0.8266 Å (synchrotron radiation at Beamline 11.3.1 at the Advanced Light Source, Lawrence Berkeley Laboratory), monoclinic, space group P21/c (no. 14), a = 22.5380(11), b = 34.0435(15), c = 18.4298(8) Å, β = 92.787(2)°, T = 100(2) K, V = 14124.0(11) Å3, Z = 8, 443665 reflections measured, 33679 unique (Rint = 0.0692), Bruker ApexII; 2θmax = 65.89°; min/max transmission = 0.691/ 0.747 (multi-scan absorption correction applied); direct and Patterson methods solution; full-matrix least squares based on F2 (SHELXT and SHELXL-2014); Final wR(F2) = 0.0839 (all data), conventional R1 = 0.0322 computed for 28087 reflections with I > 4σ (FO) and 0.0433 for all 33679 data, with 2267 parameters and 0 restraints.

X-ray Crystallography and Data Collection of parallel-3.

Crystals of *parallel*-3 were obtained by slow diffusion of methanol into a dichloromethane solution of the complex. Crystal data for parallel-3, [Ru3(CO)9]2{μ3-η2,η2,η2-C60[C(COOC2H5)2]4} (CCDC 1039742). C107H42Cl2O34Ru6, M = 2548.78, red plate, 0.207×0.078×0.062mm, λ = 0.71073 Å, triclinic, space group P-1 (no. 2), a = 16.3234(10), b = 16.3914(10), c = 18.3063(11) Å, α = 64.2930(8)°, β= 83.7400(9)°, γ = 83.3010(9)°, T = 90(2) K, V = 4373.8(5) Å3, Z = 2, 52962 reflections measured, 17896 unique (Rint = 0.0514), Bruker ApexII; 2θmax = 52.74°; min/max transmission = 0.6855/ 0.7456 (multi-scan absorption correction applied); direct and Patterson methods solution; full-matrix least squares based on F2 (SHELXT and SHELXL-2014); Final wR(F2) = 0.0903 (all data), conventional R1 = 0.0379 for 13187 reflections with I > 2σ (I) with 1369 parameters and 16 restraints. Formula given corresponds to full occupancy of the $Ru_3(CO)_9$. However, the group Ru1/Ru2/Ru3/O9-O17/C45-C53 refined to an occupancy of 0.9530(14) and the group Ru4/Ru5/Ru6/O26-O34/C98-C106 refined to an occupancy of 0.9400(14).

6.4.2 Plots

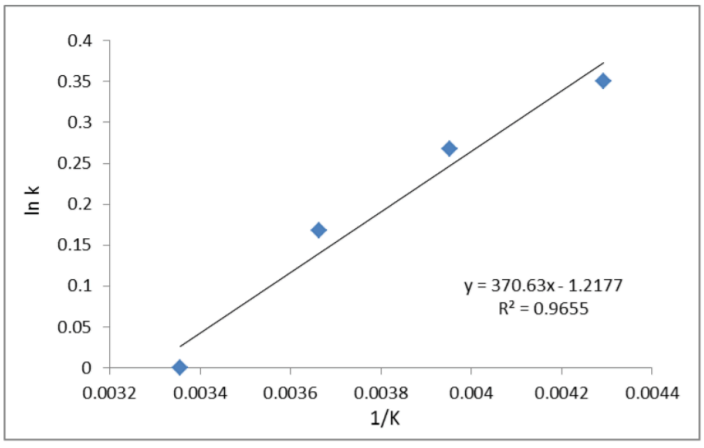

Figure 6.10: van't Hoff plot for the *tilted*-3 ↔ *parallel*-3 interconversion

References

1. Yan, W.; Seifermann, S. M.; Pierrat, P.; Brase, S., Synthesis of highly functionalized C60 fullerene derivatives and their applications in material and life sciences. *Organic & Biomolecular Chemistry* **2015,** *13* (1), 25-54.
2. Coro, J.; Suárez, M.; Silva, L. S. R.; Eguiluz, K. I. B.; Salazar-Banda, G. R., Fullerene applications in fuel cells: A review. *International Journal of Hydrogen Energy* **2016,** *41* (40), 17944-17959.
3. Ganesamoorthy, R.; Sathiyan, G.; Sakthivel, P., Review: Fullerene based acceptors for efficient bulk heterojunction organic solar cell applications. *Solar Energy Materials and Solar Cells* **2017,** *161*, 102-148.
4. Lai, Y.-Y.; Cheng, Y.-J.; Hsu, C.-S., Applications of functional fullerene materials in polymer solar cells. *Energy & Environmental Science* **2014,** *7* (6), 1866-1883.
5. Mohajeri, A.; Omidvar, A., Fullerene-based materials for solar cell applications: design of novel acceptors for efficient polymer solar cells - a DFT study. *Physical Chemistry Chemical Physics* **2015,** *17* (34), 22367-22376.
6. Kratschmer, W.; Lamb, L. D.; Fostiropoulos, K.; Huffman, D. R., Solid C60: a new form of carbon. *Nature* **1990,** *347* (6291), 354-358.
7. Pasimeni, L.; Hirsch, A.; Lamparth, I.; Herzog, A.; Maggini, M.; Prato, M.; Corvaja, C.; Scorrano, G., Use of Transient EPR Spectroscopy of Excited Triplet State for the Structural Assignment of Bisadducts of Fullerene C60. *Journal of the American Chemical Society* **1997,** *119* (52), 12896-12901.
8. Marchesan, S.; Da Ros, T.; Prato, M., Isolation and Characterization of Nine Tris-adducts of N-Methylfulleropyrrolidine Derivatives. *The Journal of Organic Chemistry* **2005,** *70* (12), 4706-4713.
9. Hirsch, A.; Lamparth, I.; Karfunkel, H. R., Fullerene Chemistry in Three Dimensions: Isolation of Seven Regioisomeric Bisadducts and Chiral Trisadducts of C60 and Di(ethoxycarbonyl)methylene. *Angewandte Chemie International Edition in English* **1994,** *33* (4), 437-438.
10. Isaacs, L.; Diederich, F.; Haldimann, R. F., Multiple Adducts of C60 by Tether-Directed Remote Functionalization and synthesis of soluble derivatives of new carbon allotropes Cn(60+5). *Helvetica Chimica Acta* **1997,** *80* (2), 317-342.
11. Ashton, P. R.; Diederich, F.; Gómez-López, M.; Nierengarten, J.-F.; Preece, J. A.; Raymo, F. M.; Stoddart, J. F., Self-Assembly of the First Fullerene-Containing [2]Catenane. *Angewandte Chemie International Edition in English* **1997,** *36* (13-14), 1448-1451.
12. Isaacs, L.; Haldimann, R. F.; Diederich, F., Tether-Directed Remote Functionalization of Buckminsterfullerene: Regiospecific Hexaadduct Formation. *Angewandte Chemie International Edition in English* **1994,** *33* (22), 2339-2342.
13. Sergeyev, S.; Diederich, F., Regio- and Stereoselective Tether-Directed Remote Functionalization of C60 with Derivatives of the Tröger Base. *Angewandte Chemie International Edition* **2004,** *43* (13), 1738-1740.
14. Kräutler, B.; Müller, T.; Maynollo, J.; Gruber, K.; Kratky, C.; Ochsenbein, P.; Schwarzenbach, D.; Bürgi, H.-B., A Topochemically Controlled, Regiospecific Fullerene

Bisfunctionalization. *Angewandte Chemie International Edition in English* **1996,** *35* (11), 1204-1206.
15. Duarte-Ruiz, A.; Wurst, K.; Kräutler, B., Regioselective `One-Pot' Synthesis of Antipodal Bis-adducts by Heating of Solid [5,6]Fullerene-C60-Ih and Anthracenes, Preliminary Communication. *Helvetica Chimica Acta* **2001,** *84* (8), 2167-2177.
16. Schwenninger, R.; Müller, T.; Kräutler, B., Concise Route to Symmetric Multiadducts of [60]Fullerene: Preparation of an Equatorial Tetraadduct by Orthogonal Transposition. *Journal of the American Chemical Society* **1997,** *119* (39), 9317-9318.
17. Kraft, A.; Beuerle, F., Metal–organic hybrid architectures built from functionalized fullerenes and metal ions or clusters. *Tetrahedron Letters* **2016,** *57* (42), 4651-4663.
18. Nagashima, H.; Nakaoka, A.; Saito, Y.; Kato, M.; Kawanishi, T.; Itoh, K., C60Pd: the first organometallic polymer of buckminsterfullerene. *Journal of the Chemical Society, Chemical Communications* **1992,** (4), 377-379.
19. Wohlers, M.; Herzog, B.; Belz, T.; Bauer, A.; Braun, T.; Rühle, T.; Schlögl, R., Ruthenium-C60 compounds: properties and catalytic potential. *Synthetic Metals* **1996,** *77* (1–3), 55-58.
20. Herbst, M. H.; Pinhal, N. M.; Demétrio, F. A. T.; Dias, G. H. M.; Vugman, N. V., Solid-state structural studies on amorphous platinum–fullerene[60] compounds [PtnC60] (n=1,2). *Journal of Non-Crystalline Solids* **2000,** *272* (2–3), 127-130.
21. Lee, K.; Song, H.; Kim, B.; Park, J. T.; Park, S.; Choi, M.-G., The First Fullerene–Metal Sandwich Complex: An Unusually Strong Electronic Communication between Two C60 Cages. *Journal of the American Chemical Society* **2002,** *124* (12), 2872-2873.
22. Konarev, D. V.; Khasanov, S. S.; Nakano, Y.; Otsuka, A.; Yamochi, H.; Saito, G.; Lyubovskaya, R. N., Linear Coordination Fullerene C60 Polymer [{Ni(Me3P)2}(μ-η2,η2-C60)]∞ Bridged by Zerovalent Nickel Atoms. *Inorganic Chemistry* **2014,** *53* (22), 11960-11965.
23. Habicher, T.; Nierengarten, J.-F.; Gramlich, V.; Diederich, F., PtII-Directed Self-Assembly of a Dinuclear Cyclophane Containing Two Fullerenes. *Angewandte Chemie International Edition* **1998,** *37* (13-14), 1916-1919.
24. Fan, J.; Wang, Y.; Blake, A. J.; Wilson, C.; Davies, E. S.; Khlobystov, A. N.; Schröder, M., Controlled Assembly of Silver(I)-Pyridylfullerene Networks. *Angewandte Chemie International Edition* **2007,** *46* (42), 8013-8016.
25. Pierrat, P.; Réthoré, C.; Muller, T.; Bräse, S., Design and Efficient Synthesis of Fullerene Bismalonates as Building Blocks for Metal Organic Frameworks and Organic Nanostructures. *Synlett* **2008,** *2008* (11), 1706-1710.
26. Rio, Y.; Sánchez-García, D.; Seitz, W.; Torres, T.; Sessler, J. L.; Guldi, D. M., A Bisfullerene–Bis(dipyrrinato)zinc Complex: Electronic Coupling and Charge Separation in an Easy-to-Assemble Synthetic System. *Chemistry – A European Journal* **2009,** *15* (16), 3956-3959.
27. Fu, K.; Henbest, K.; Zhang, Y. J.; Valentin, S.; Sun, Y.-P., Synthesis and optical properties of metal-centered dimeric fullerene macromolecules. *Journal of Photochemistry and Photobiology A: Chemistry* **2002,** *150* (1–3), 143-152.
28. Rio, Y.; Enderlin, G.; Bourgogne, C.; Nierengarten, J.-F.; Gisselbrecht, J.-P.; Gross, M.; Accorsi, G.; Armaroli, N., Ground and Excited State Electronic Interactions in a Bis(phenanthroline) Copper(I) Complex Sandwiched between Two Fullerene Subunits. *Inorganic Chemistry* **2003,** *42* (26), 8783-8793.

29. Cardinali, F.; Mamlouk, H.; Rio, Y.; Armaroli, N.; Nierengarten, J.-F., Fullerohelicates: a new class of fullerene-containing supermolecules. *Chemical Communications* **2004,** (14), 1582-1583.
30. Chancellor, C. J.; Olmstead, M. M.; Balch, A. L., Formation of Crystalline Polymers from the Reaction of Amine-Functionalized C60 with Silver Salts. *Inorganic Chemistry* **2009,** *48* (4), 1339-1345.
31. Aghabali, A.; Olmstead, M. M.; Balch, A. L., Zipping up fullerenes into polymers using rhodium(ii) acetate dimer and N(CH2CH2)2NC60 as building blocks. *Chemical Communications* **2014,** *50* (96), 15152-15155.
32. Peng, P.; Li, F.-F.; Bowles, F. L.; Neti, V. S. P. K.; J. Metta-Magana, A.; Olmstead, M. M.; Balch, A. L.; Echegoyen, L., High yield synthesis of a new fullerene linker and its use in the formation of a linear coordination polymer by silver complexation. *Chemical Communications* **2013,** *49* (31), 3209-3211.
33. Chen, C.-H.; Aghabali, A.; Metta-Magana, A. J.; Olmstead, M. M.; Balch, A. L.; Echegoyen, L., Synthesis and characterization of a trans-1 hexakis-fullerene linker that forms crystalline polymers with silver salts. *Dalton Transactions* **2015,** *44* (42), 18487-18491.
34. COMPLEXES OF 4,5-DIAZAFLUORENE AND 9,9′-BIS(4,5-DIAZAFLUORENYL) WITH NICKEL(II), COPPER(II) AND ZINC(II). *Journal of Coordination Chemistry* **2001,** *53* (4), 347-354.
35. Annibale, V. T.; Song, D., Coordination chemistry and applications of versatile 4,5-diazafluorene derivatives. *Dalton Transactions* **2016,** *45* (1), 32-49.
36. Gygi, D.; Bloch, E. D.; Mason, J. A.; Hudson, M. R.; Gonzalez, M. I.; Siegelman, R. L.; Darwish, T. A.; Queen, W. L.; Brown, C. M.; Long, J. R., Hydrogen Storage in the Expanded Pore Metal–Organic Frameworks M2(dobpdc) (M = Mg, Mn, Fe, Co, Ni, Zn). *Chemistry of Materials* **2016,** *28* (4), 1128-1138.
37. Han, S. S.; Mendoza-Cortes, J. L.; Goddard Iii, W. A., Recent advances on simulation and theory of hydrogen storage in metal-organic frameworks and covalent organic frameworks. *Chemical Society Reviews* **2009,** *38* (5), 1460-1476.
38. Lee, C. Y.; Farha, O. K.; Hong, B. J.; Sarjeant, A. A.; Nguyen, S. T.; Hupp, J. T., Light-Harvesting Metal–Organic Frameworks (MOFs): Efficient Strut-to-Strut Energy Transfer in Bodipy and Porphyrin-Based MOFs. *Journal of the American Chemical Society* **2011,** *133* (40), 15858-15861.
39. Ferey, G., Hybrid porous solids: past, present, future. *Chemical Society Reviews* **2008,** *37* (1), 191-214.
40. Tranchemontagne, D. J.; Mendoza-Cortes, J. L.; O'Keeffe, M.; Yaghi, O. M., Secondary building units, nets and bonding in the chemistry of metal-organic frameworks. *Chemical Society Reviews* **2009,** *38* (5), 1257-1283.
41. Morris, R. E.; Wheatley, P. S., Gas Storage in Nanoporous Materials. *Angewandte Chemie International Edition* **2008,** *47* (27), 4966-4981.
42. Müller-Buschbaum, K.; Beuerle, F.; Feldmann, C., MOF based luminescence tuning and chemical/physical sensing. *Microporous and Mesoporous Materials* **2015,** *216*, 171-199.
43. Corma, A.; García, H.; Llabrés i Xamena, F. X., Engineering Metal Organic Frameworks for Heterogeneous Catalysis. *Chemical Reviews* **2010,** *110* (8), 4606-4655.
44. Rowsell, J. L. C.; Yaghi, O. M., Strategies for Hydrogen Storage in Metal–Organic Frameworks. *Angewandte Chemie International Edition* **2005,** *44* (30), 4670-4679.

45. Li, H.; Eddaoudi, M.; O'Keeffe, M.; Yaghi, O. M., Design and synthesis of an exceptionally stable and highly porous metal-organic framework. *Nature* **1999,** *402* (6759), 276-279.
46. Rowsell, J. L. C.; Millward, A. R.; Park, K. S.; Yaghi, O. M., Hydrogen Sorption in Functionalized Metal–Organic Frameworks. *Journal of the American Chemical Society* **2004,** *126* (18), 5666-5667.
47. Wu, H.; Zhou, W.; Yildirim, T., Hydrogen Storage in a Prototypical Zeolitic Imidazolate Framework-8. *Journal of the American Chemical Society* **2007,** *129* (17), 5314-5315.
48. Kaye, S. S.; Dailly, A.; Yaghi, O. M.; Long, J. R., Impact of Preparation and Handling on the Hydrogen Storage Properties of Zn4O(1,4-benzenedicarboxylate)3 (MOF-5). *Journal of the American Chemical Society* **2007,** *129* (46), 14176-14177.
49. Li, Y.; Yang, R. T., Gas Adsorption and Storage in Metal–Organic Framework MOF-177. *Langmuir* **2007,** *23* (26), 12937-12944.
50. Dincă, M.; Long, J. R., Hydrogen Storage in Microporous Metal–Organic Frameworks with Exposed Metal Sites. *Angewandte Chemie International Edition* **2008,** *47* (36), 6766-6779.
51. Murray, L. J.; Dinca, M.; Long, J. R., Hydrogen storage in metal-organic frameworks. *Chemical Society Reviews* **2009,** *38* (5), 1294-1314.
52. Getman, R. B.; Bae, Y.-S.; Wilmer, C. E.; Snurr, R. Q., Review and Analysis of Molecular Simulations of Methane, Hydrogen, and Acetylene Storage in Metal–Organic Frameworks. *Chemical Reviews* **2012,** *112* (2), 703-723.
53. Suh, M. P.; Park, H. J.; Prasad, T. K.; Lim, D.-W., Hydrogen Storage in Metal–Organic Frameworks. *Chemical Reviews* **2012,** *112* (2), 782-835.
54. Rosi, N. L.; Eckert, J.; Eddaoudi, M.; Vodak, D. T.; Kim, J.; Keeffe, M.; Yaghi, O. M., Hydrogen Storage in Microporous Metal-Organic Frameworks. *Science* **2003,** *300* (5622), 1127.
55. A Computational Investigation of the Electronic Properties of Partially Hydrogenated Fullerenes C60Hn (n = 18, 20, 24, 36 and 48). *Fullerenes, Nanotubes and Carbon Nanostructures* **2015,** *23* (1), 40-48.
56. Hudson, B. S.; Braden, D. A.; Parker, S. F.; Prinzbach, H., The Vibrational Inelastic Neutron Scattering Spectrum of Dodecahedrane: Experiment and DFT Simulation. *Angewandte Chemie International Edition* **2000,** *39* (3), 514-516.
57. Attalla, M. I.; Vassallo, A. M.; Tattam, B. N.; Hanna, J. V., Preparation of hydrofullerenes by hydrogen radical induced hydrogenation. *The Journal of Physical Chemistry* **1993,** *97* (24), 6329-6331.
58. Nossal, J.; Saini, Rajesh K.; Alemany, Lawrence B.; Meier, M.; Billups, W. E., The Synthesis and Characterization of Fullerene Hydrides. *European Journal of Organic Chemistry* **2001,** *2001* (22), 4167-4180.
59. Dunlap, B. I.; Brenner, D. W.; Mintmire, J. W.; Mowrey, R. C.; White, C. T., Geometric and electronic structures of C60H60, C60F60, and C60H36. *The Journal of Physical Chemistry* **1991,** *95* (15), 5763-5768.
60. Guo, T.; Scuseria, G. E., Ab initio calculations of tetrahedral hydrogenated buckminsterfullerene. *Chemical Physics Letters* **1992,** *191* (6), 527-532.
61. Palit, D. K.; Mohan, H.; Mittal, J. P., Photophysical Properties of C60H18 and C60H36: A Laser Flash Photolysis and Pulse Radiolysis Study. *The Journal of Physical Chemistry A* **1998,** *102* (24), 4456-4461.

62. Vehviläinen, T. T.; Ganchenkova, M. G.; Oikkonen, L. E.; Nieminen, R. M., Hydrogen interaction with fullerenes: From C${}_{20}$ to graphene. *Physical Review B* **2011,** *84* (8), 085447.
63. Okamoto, Y., Ab Initio Investigation of Hydrogenation of C60. *The Journal of Physical Chemistry A* **2001,** *105* (32), 7634-7637.
64. Gao, Y.; Wu, X.; Zeng, X. C., Designs of fullerene-based frameworks for hydrogen storage. *Journal of Materials Chemistry A* **2014,** *2* (16), 5910-5914.
65. Sun, Q.; Jena, P.; Wang, Q.; Marquez, M., First-Principles Study of Hydrogen Storage on Li12C60. *Journal of the American Chemical Society* **2006,** *128* (30), 9741-9745.
66. Zhao, Y.; Kim, Y.-H.; Dillon, A. C.; Heben, M. J.; Zhang, S. B., Hydrogen Storage in Novel Organometallic Buckyballs. *Physical Review Letters* **2005,** *94* (15), 155504.
67. Kim, Y.-H.; Zhao, Y.; Williamson, A.; Heben, M. J.; Zhang, S. B., Nondissociative Adsorption of ${\mathrm{H}}_{2}$ Molecules in Light-Element-Doped Fullerenes. *Physical Review Letters* **2006,** *96* (1), 016102.
68. Yoon, M.; Yang, S.; Hicke, C.; Wang, E.; Geohegan, D.; Zhang, Z., Calcium as the Superior Coating Metal in Functionalization of Carbon Fullerenes for High-Capacity Hydrogen Storage. *Physical Review Letters* **2008,** *100* (20), 206806.
69. Sun, D.; Tham, F. S.; Reed, C. A.; Boyd, P. D. W., Extending supramolecular fullerene-porphyrin chemistry to pillared metal-organic frameworks. *Proceedings of the National Academy of Sciences* **2002,** *99* (8), 5088-5092.
70. Chae, H. K.; Siberio-Perez, D. Y.; Kim, J.; Go, Y.; Eddaoudi, M.; Matzger, A. J.; O'Keeffe, M.; Yaghi, O. M., A route to high surface area, porosity and inclusion of large molecules in crystals. *Nature* **2004,** *427* (6974), 523-527.
71. Constable, E. C.; Zhang, G.; Housecroft, C. E.; Zampese, J. A., Bucky-blocks: templating a coordination network with C60. *CrystEngComm* **2012,** *14* (5), 1770-1774.
72. Peng, P.; Li, F.-F.; Neti, V. S. P. K.; Metta-Magana, A. J.; Echegoyen, L., Design, Synthesis, and X-Ray Crystal Structure of a Fullerene-Linked Metal–Organic Framework. *Angewandte Chemie International Edition* **2014,** *53* (1), 160-163.
73. Kraft, A.; Roth, P.; Schmidt, D.; Stangl, J.; Müller-Buschbaum, K.; Beuerle, F., Three-Dimensional Metal–Fullerene Frameworks. *Chemistry – A European Journal* **2016,** *22* (17), 5982-5987.
74. Ortiz, A. L.; Rivera, D. M.; Athans, A. J.; Echegoyen, L., Regioselective Addition of N-(4-Thiocyanatophenyl)pyrrolidine Addends to Fullerenes. *European Journal of Organic Chemistry* **2009,** *2009* (20), 3396-3403.
75. Herranz, M. Á.; Diederich, F.; Echegoyen, L., Electrochemically Induced Retro-Cyclopropanation Reactions. *European Journal of Organic Chemistry* **2004,** *2004* (11), 2299-2316.
76. Wade, C. R.; Dinca, M., Investigation of the synthesis, activation, and isosteric heats of CO2 adsorption of the isostructural series of metal-organic frameworks M3(BTC)2 (M = Cr, Fe, Ni, Cu, Mo, Ru). *Dalton Transactions* **2012,** *41* (26), 7931-7938.
77. Ma, L.-F.; Han, M.-L.; Qin, J.-H.; Wang, L.-Y.; Du, M., MnII Coordination Polymers Based on Bi-, Tri-, and Tetranuclear and Polymeric Chain Building Units: Crystal Structures and Magnetic Properties. *Inorganic Chemistry* **2012,** *51* (17), 9431-9442.
78. Zhang, Q.; Cao, L.; Li, B.; Chen, L., Catalyzed activation of CO2 by a Lewis-base site in W-Cu-BTC hybrid metal organic frameworks. *Chemical Science* **2012,** *3* (9), 2708-2715.

79. Cotton, F. A.; Daniels, L. M.; Lin, C.; Murillo, C. A., Square and Triangular Arrays Based on Mo24+ and Rh24+ Units. *Journal of the American Chemical Society* **1999,** *121* (18), 4538-4539.
80. Zhao, D.; Timmons, D. J.; Yuan, D.; Zhou, H.-C., Tuning the Topology and Functionality of Metal–Organic Frameworks by Ligand Design. *Accounts of Chemical Research* **2011,** *44* (2), 123-133.
81. Yuan, D.; Zhao, D.; Timmons, D. J.; Zhou, H.-C., A stepwise transition from microporosity to mesoporosity in metal-organic frameworks by thermal treatment. *Chemical Science* **2011,** *2* (1), 103-106.
82. Cotton, F. A.; Liu, C. Y.; Murillo, C. A., Systematic Preparation of Mo24+ Building Blocks for Supramolecular Assemblies. *Inorganic Chemistry* **2004,** *43* (7), 2267-2276.
83. Shi, J. L.; Li, F. B.; Zhang, X. F.; Wu, J.; Zhang, H. Y.; Peng, J.; Liu, C. X.; Liu, L.; Wu, P.; Li, J. X., Synthesis and Functionalization of Symmetrical 2,5-Diaryl Fulleropyrrolidines: Ferric Perchlorate-Mediated One-Step Reaction of [60]Fullerene with Arylmethanamines. *J Org Chem* **2016,** *81* (5), 1769-77.
84. Delgado, J. L.; Martin, N.; de la Cruz, P.; Langa, F., Pyrazolinofullerenes: a less known type of highly versatile fullerene derivatives. *Chem Soc Rev* **2011,** *40* (11), 5232-41.
85. Ishida, H.; Itoh, K.; Ohno, M., 1,3-Dipolar cycloaddition reaction of [60]fullerene with thiocarbonyl ylide and synthetic application of the cycloadduct. *Tetrahedron* **2001,** *57* (9), 1737-1747.
86. Tat, F. T.; Zhou, Z.; MacMahon, S.; Song, F.; Rheingold, A. L.; Echegoyen, L.; Schuster, D. I.; Wilson, S. R., A New Fullerene Complexation Ligand: N-Pyridylfulleropyrrolidine. *The Journal of Organic Chemistry* **2004,** *69* (14), 4602-4606.
87. Troshin, P. A.; Peregudov, A. S.; Mühlbacher, D.; Lyubovskaya, R. N., An Efficient [2+3] Cycloaddition Approach to the Synthesis of Pyridyl-Appended Fullerene Ligands. *European Journal of Organic Chemistry* **2005,** *2005* (14), 3064-3074.
88. Troshin, P. A.; Kornev, A. B.; Peregudov, A. S.; Peregudova, S. M.; Lyubovskaya, R. N., Benzylamine imines as versatile precursors to azomethine and nitrile ylides in the [2 + 3] cycloaddition reactions with [60]fullerene. *Mendeleev Communications* **2007,** *17* (2), 116-118.
89. Maggini, M.; Karlsson, A.; Pasimeni, L.; Scorrano, G.; Prato, M.; Valli, L., Synthesis of N-acylated fulleropyrrolidines: New materials for the preparation of Langmuir-Blodgett films containing fullerenes. *Tetrahedron Letters* **1994,** *35* (18), 2985-2988.
90. Lian-He, S.; Guan-Wu, W.; Shi-Hui, W.; Hou-Ming, W.; Xia-Fei, L., 1,3-dipolar cycloaddition reaction of [60]fullerene and imines of α-amino acid esters: Formation of fullerene-fused proline derivatives. *Tetrahedron Letters* **1995,** *36* (22), 3871-3874.
91. Komori, A.; Kubota, M.; Ishida, T.; Niwa, H.; Nogami, T., Unusual reactions of C60 with aldehydes in the presence of aqueous ammonia. *Tetrahedron Letters* **1996,** *37* (23), 4031-4034.
92. Safaei-Ghomi, J.; Masoomi, R., Rapid microwave-assisted synthesis of N-benzyl fulleropyrrolidines under solvent free conditions. *RSC Adv*. **2015,** *5* (20), 15591-15596.
93. Zhu, S. E.; Cheng, X.; Li, Y. J.; Mai, C. K.; Huang, Y. S.; Wang, G. W.; Peng, R. F.; Jin, B.; Chu, S. J., Study on the thermal reactions of [60]fullerene with amino acids and amino acid esters. *Org Biomol Chem* **2012,** *10* (43), 8720-9.
94. Jin, B.; Peng, R.-F.; Shen, J.; Wang, G.-W.; Tan, B.-S.; Chu, S.-J., Direct Formation of Cycloadducts Between Fullerenes and Amino Acids Through Electron-Transfer Processes. *Synthetic Communications* **2012,** *42* (10), 1532-1541.

95. Lawson, G. E.; Kitaygorodskiy, A.; Ma, B.; Bunker, C. E.; Sun, Y.-P., Photoinduced inter- and intra-molecular electron transfer reactions of [60]fullerene and a tertiary amine. Formation of the cycloadduct N-ethyl-trans-2[prime or minute],5[prime or minute]-dimethylpyrrolidino[3[prime or minute],4[prime or minute]:1,2][60]fullerene. *Journal of the Chemical Society, Chemical Communications* **1995,** (21), 2225-2226.
96. Liou, K.-F.; Cheng, C.-H., Photoinduced reactions of tertiary amines with [60]fullerene; addition of an [small alpha]-C-H bond of amines to [60]fullerene. *Chemical Communications* **1996,** (12), 1423-1424.
97. Gan, L.; Jiang, J.; Zhang, W.; Su, Y.; Shi, Y.; Huang, C.; Pan, J.; Lü, M.; Wu, Y., Synthesis of Pyrrolidine Ring-Fused Fullerene Multicarboxylates by Photoreaction. *The Journal of Organic Chemistry* **1998,** *63* (13), 4240-4247.
98. Gan, L.; Zhou, D.; Luo, C.; Tan, H.; Huang, C.; Lü, M.; Pan, J.; Wu, Y., Synthesis of Fullerene Amino Acid Derivatives by Direct Interaction of Amino Acid Ester with C60. *The Journal of Organic Chemistry* **1996,** *61* (6), 1954-1961.
99. Zhang, X.; Gan, L.; Huang, S.; Shi, Y., Iodo-Controlled Selective Formation of Pyrrolidino[60]fullerene and Aziridino[60]fullerene from the Reaction between C60 and Amino Acid Esters. *The Journal of Organic Chemistry* **2004,** *69* (17), 5800-5802.
100. Jin, B.; Shen, J.; Peng, R.; Chen, C.; Chu, S., Reactions of [60]Fullerene with Halides and Amino Acids to Synthesize Fulleropyrrolidines. *European Journal of Organic Chemistry* **2014,** *2014* (28), 6252-6262.
101. Yamamoto, S. S., Junya; Fukase, Yoshiyuki; Tomata, Yoshihide; Sato, Ayumu; Ochida, Atsuko; Yonemori, Kazuko; Nakagawa, Hideyuki Preparation of indole and carbazole derivatives as inhibitors of retinoid-related orphan receptor γt (RORγt). 2013.
102. Burke, M. D. D., Graham R.; Knapp, David M.; Gillis, Eric P.; Klubnick, Jenna A. Methods for forming protected organoboronic acids. 2011.
103. Maggini, M.; Scorrano, G.; Prato, M., Addition of azomethine ylides to C60: synthesis, characterization, and functionalization of fullerene pyrrolidines. *Journal of the American Chemical Society* **1993,** *115* (21), 9798-9799.
104. Maggini, M.; Scorrano, G.; Bianco, A.; Toniolo, C.; Sijbesma, R. P.; Wudl, F.; Prato, M., Addition reactions of C60 leading to fulleroprolines. *Journal of the Chemical Society, Chemical Communications* **1994,** (3), 305-306.
105. Zhang, X.; Willems, M.; Foote, C. S., 1,3-Dipolar cycloaddition of N-benzyl azomethine ylide to C60: Formation of a C60-fused N-benzylpyrrolidine. *Tetrahedron Letters* **1993,** *34* (51), 8187-8188.
106. Wu, S.-H.; Sun, W.-Q.; Zhang, D.-W.; Shu, L.-H.; Wu, H.-M.; Xu, J.-F.; Lao, X.-F., 1,3-Dipolar cycloaddition of several azomethine ylides to [60]fullerene: synthesis of derivatives of 2[prime or minute],5[prime or minute]-dihydro-1[prime or minute]H-pyrrolo[3[prime or minute],4[prime or minute] : 1,2][60]fullerene 1. *Journal of the Chemical Society, Perkin Transactions 1* **1998,** (10), 1733-1738.
107. Zhou, D.; Tan, H.; Luo, C.; Gan, L.; Huang, C.; Pan, J.; Lü, M.; Wu, Y., Fullerene induced c-n bond breaking and formation: synthesis of fullerene pyrrolidine and methanofullerene sarcosine derivatives by photochemical addition of sarcosine ester to c60. *Tetrahedron Letters* **1995,** *36* (50), 9169-9172.
108. Tan, X.; Schuster, D. I.; Wilson, S. R., Resolution and absolute configuration of a C2-symmetric trans-2, 5-disubstituted fulleropyrrolidine. *Tetrahedron Letters* **1998,** *39* (24), 4187-4190.

109. Popov, A. A.; Yang, S.; Dunsch, L., Endohedral fullerenes. *Chem Rev* **2013,** *113* (8), 5989-6113.
110. Yang, S.; Zalibera, M.; Rapta, P.; Dunsch, L., Charge-Induced Reversible Rearrangement of Endohedral Fullerenes: Electrochemistry of Tridysprosium Nitride Clusterfullerenes Dy3N@C2n (2n=78, 80). *Chemistry – A European Journal* **2006,** *12* (30), 7848-7855.
111. Popov, A. A.; Avdoshenko, S. M.; Cuniberti, G.; Dunsch, L., Dimerization of Radical-Anions: Nitride Clusterfullerenes versus Empty Fullerenes. *The Journal of Physical Chemistry Letters* **2011,** *2* (13), 1592-1600.
112. Mu, L.; Bao, X.; Yang, S.; Kong, X., Dimetallofullerene M2@C100 or carbide cluster fullerene M2C2@C98 (M = La, Y, and Sc): which ones are more stable? *RSC Adv*. **2017,** *7* (26), 16149-16154.
113. Yamada, M.; Nakahodo, T.; Wakahara, T.; Tsuchiya, T.; Maeda, Y.; Akasaka, T.; Kako, M.; Yoza, K.; Horn, E.; Mizorogi, N.; Kobayashi, K.; Nagase, S., Positional Control of Encapsulated Atoms Inside a Fullerene Cage by Exohedral Addition. *Journal of the American Chemical Society* **2005,** *127* (42), 14570-14571.
114. Yamada, M.; Mizorogi, N.; Tsuchiya, T.; Akasaka, T.; Nagase, S., Synthesis and characterization of the D5h isomer of the endohedral dimetallofullerene Ce2@C80: two-dimensional circulation of encapsulated metal atoms inside a fullerene cage. *Chemistry* **2009,** *15* (37), 9486-93.
115. Lu, X.; Nikawa, H.; Nakahodo, T.; Tsuchiya, T.; Ishitsuka, M. O.; Maeda, Y.; Akasaka, T.; Toki, M.; Sawa, H.; Slanina, Z.; Mizorogi, N.; Nagase, S., Chemical Understanding of a Non-IPR Metallofullerene: Stabilization of Encaged Metals on Fused-Pentagon Bonds in La2@C72. *Journal of the American Chemical Society* **2008,** *130* (28), 9129-9136.
116. Cao, B.; Wakahara, T.; Tsuchiya, T.; Kondo, M.; Maeda, Y.; Aminur Rahman, G. M.; Akasaka, T.; Kobayashi, K.; Nagase, S.; Yamamoto, K., Isolation, Characterization, and Theoretical Study of La2@C78. *Journal of the American Chemical Society* **2004,** *126* (30), 9164-9165.
117. Yamada, M.; Wakahara, T.; Tsuchiya, T.; Maeda, Y.; Kako, M.; Akasaka, T.; Yoza, K.; Horn, E.; Mizorogi, N.; Nagase, S., Location of the metal atoms in Ce2@C78 and its bis-silylated derivative. *Chem Commun (Camb)* **2008,** (5), 558-60.
118. Guo, Y. J.; Yang, T.; Nagase, S.; Zhao, X., Carbide clusterfullerene Gd2C2@C92 vs dimetallofullerene Gd2@C94: a quantum chemical survey. *Inorg Chem* **2014,** *53* (4), 2012-21.
119. Kurihara, H.; Lu, X.; Iiduka, Y.; Mizorogi, N.; Slanina, Z.; Tsuchiya, T.; Nagase, S.; Akasaka, T., Sc2@C3v(8)-C82 vs. Sc2C2@C3v(8)-C82: drastic effect of C2 capture on the redox properties of scandium metallofullerenes. *Chem Commun (Camb)* **2012,** *48* (9), 1290-2.
120. Stevenson, S.; Thompson, H. R.; Arvola, K. D.; Ghiassi, K. B.; Olmstead, M. M.; Balch, A. L., Isolation of CeLu2 N@Ih -C80 through a Non-Chromatographic, Two-Step Chemical Process and Crystallographic Characterization of the Pyramidalized CeLu2 N within the Icosahedral Cage. *Chemistry* **2015,** *21* (29), 10362-8.
121. Ge, Z.; Duchamp, J. C.; Cai, T.; Gibson, H. W.; Dorn, H. C., Purification of Endohedral Trimetallic Nitride Fullerenes in a Single, Facile Step. *Journal of the American Chemical Society* **2005,** *127* (46), 16292-16298.
122. Maki, S.; Nishibori, E.; Terauchi, I.; Ishihara, M.; Aoyagi, S.; Sakata, M.; Takata, M.; Umemoto, H.; Inoue, T.; Shinohara, H., A structural diagnostics diagram for metallofullerenes encapsulating metal carbides and nitrides. *J Am Chem Soc* **2013,** *135* (2), 918-23.

123. Miyazaki, T.; Sumii, R.; Umemoto, H.; Okimoto, H.; Sugai, T.; Shinohara, H.; Hino, S., Ultraviolet photoelectron spectra of Lu atoms encapsulated C2v–C82 fullerenes. *Chemical Physics Letters* **2013,** *555*, 222-225.
124. Rodríguez-Fortea, A.; Alegret, N.; Balch, A. L.; Poblet, J. M., The maximum pentagon separation rule provides a guideline for the structures of endohedral metallofullerenes. *Nat Chem* **2010,** *2* (11), 955-961.
125. Wang, Y.; Morales-Martinez, R.; Zhang, X.; Yang, W.; Wang, Y.; Rodriguez-Fortea, A.; Poblet, J. M.; Feng, L.; Wang, S.; Chen, N., Unique Four-Electron Metal-to-Cage Charge Transfer of Th to a C82 Fullerene Cage: Complete Structural Characterization of Th@C3v(8)-C82. *J Am Chem Soc* **2017**.
126. Popov, A. A.; Avdoshenko, S. M.; Pendas, A. M.; Dunsch, L., Bonding between strongly repulsive metal atoms: an oxymoron made real in a confined space of endohedral metallofullerenes. *Chem Commun (Camb)* **2012,** *48* (65), 8031-50.
127. Samoylova, N. A.; Avdoshenko, S. M.; Krylov, D. S.; Thompson, H. R.; Kirkhorn, A. C.; Rosenkranz, M.; Schiemenz, S.; Ziegs, F.; Wolter, A. U. B.; Yang, S.; Stevenson, S.; Popov, A. A., Confining the spin between two metal atoms within the carbon cage: redox-active metal-metal bonds in dimetallofullerenes and their stable cation radicals. *Nanoscale* **2017**.
128. Chen, C.-H.; Aghabali, A.; Suarez, C.; Olmstead, M. M.; Balch, A. L.; Echegoyen, L., Synthesis and characterization of bis-triruthenium cluster derivatives of an all equatorial [60]fullerene tetramalonate. *Chemical Communications* **2015,** *51* (30), 6489-6492.
129. Chen, C.-H.; Lin, D.-Y.; Yeh, W.-Y., Regiospecific Coordination of Re3 Clusters with the Sumanene-Type Hexagons on Endohedral Metallofullerenes and Higher Fullerenes That Provides an Efficient Separation Method. *Chemistry – A European Journal* **2014,** *20* (19), 5768-5775.
130. Chen, C.-H.; Yeh, W.-Y.; Liu, Y.-H.; Lee, G.-H., [(μ-H)3Re3(CO)9(η2,η2,η2-Sc2C2@C3v(8)-C82)]: Face-Capping Cluster Complex of an Endohedral Fullerene. *Angewandte Chemie International Edition* **2012,** *51* (52), 13046-13049.
131. Ramírez-Monroy, A.; Swager, T. M., Metal Chelates Based on Isoxazoline[60]fullerenes. *Organometallics* **2011,** *30* (9), 2464-2467.
132. Lee, K.; Song, H.; Park, J. T., [60]Fullerene–Metal Cluster Complexes: Novel Bonding Modes and Electronic Communication. *Accounts of Chemical Research* **2003,** *36* (1), 78-86.
133. Cho, Y.-J.; Ahn, T. K.; Song, H.; Kim, K. S.; Lee, C. Y.; Seo, W. S.; Lee, K.; Kim, S. K.; Kim, D.; Park, J. T., Unusually High Performance Photovoltaic Cell Based on a [60]Fullerene Metal Cluster–Porphyrin Dyad SAM on an ITO Electrode. *Journal of the American Chemical Society* **2005,** *127* (8), 2380-2381.
134. Hsu, H.-F.; Shapley, J. R., Ru3(CO)9(μ3-η2,η2,η2-C60): A Cluster Face-Capping, Arene-Like Complex of C60. *Journal of the American Chemical Society* **1996,** *118* (38), 9192-9193.
135. Leach, S.; Vervloet, M.; Desprès, A.; Bréheret, E.; Hare, J. P.; John Dennis, T.; Kroto, H. W.; Taylor, R.; Walton, D. R. M., Electronic spectra and transitions of the fullerene C60. *Chemical Physics* **1992,** *160* (3), 451-466.
136. Lin, Y.-S.; Yeh, W.-Y., Unusual Coupling Reaction of C60 and Benzonitrile with Triosmium Carbonyls To Generate Fullerodiketimide Cluster Complexes. *Organometallics* **2014,** *33* (3), 731-735.
137. Park, B. K.; Lee, C. Y.; Jung, J.; Lim, J. H.; Han, Y.-K.; Hong, C. S.; Park, J. T., [Os3(CO)6(PMe3)3](μ3-η2:η2:η2-C60)[Re3(μ-H)3(CO)9]: A Fullerene[60] Coordinated to

Two Different Trinuclear Clusters. *Angewandte Chemie International Edition* **2007,** *46* (9), 1436-1439.
138. Rogachev, A. Y.; Sevryugina, Y.; Filatov, A. S.; Petrukhina, M. A., Corannulene vs. C60-fullerene in metal binding reactions: A direct DFT and X-ray structural comparison. *Dalton Transactions* **2007,** (35), 3871-3873.
139. Braga, D.; Grepioni, F.; Johnson, B. F. G.; Lewis, J.; Housecroft, C. E.; Martinelli, M., Static and dynamic structure of the ruthenium cluster Ru3(CO)9(.mu.3-.eta.2:.eta.2:.eta.2-C6H6) at room temperature and 193 K. *Organometallics* **1991,** *10* (5), 1260-1268.

Appendix

APPENDIX 1

ELSEVIER LICENSE
TERMS AND CONDITIONS

Jun 09, 2017

This Agreement between Catalina Suarez ("You") and Elsevier ("Elsevier") consists of your license details and the terms and conditions provided by Elsevier and Copyright Clearance Center.

License Number	4124840020765
License date	Jun 09, 2017
Licensed Content Publisher	Elsevier
Licensed Content Publication	Tetrahedron Letters
Licensed Content Title	Metal–organic hybrid architectures built from functionalized fullerenes and metal ions or clusters
Licensed Content Author	Andreas Kraft,Florian Beuerle
Licensed Content Date	Oct 19, 2016
Licensed Content Volume	57
Licensed Content Issue	42
Licensed Content Pages	13
Start Page	4651
End Page	4663
Type of Use	reuse in a thesis/dissertation
Portion	figures/tables/illustrations
Number of figures/tables/illustrations	5
Format	both print and electronic
Are you the author of this Elsevier article?	No
Will you be translating?	No
Order reference number	
Original figure numbers	figures 1a, 2, 3, 7, 8
Title of your thesis/dissertation	Design and regioselective synthesis of fullerene derivatives for metal-organic hybrid architectures
Expected completion date	Jun 2017
Estimated size (number of pages)	160
Elsevier VAT number	GB 494 6272 12
Requestor Location	Catalina Suarez

APPENDIX 2

ROYAL SOCIETY OF CHEMISTRY LICENSE TERMS AND CONDITIONS

Jun 09, 2017

This Agreement between Catalina Suarez ("You") and Royal Society of Chemistry ("Royal Society of Chemistry") consists of your license details and the terms and conditions provided by Royal Society of Chemistry and Copyright Clearance Center.

License Number	4124990096131
License date	Jun 09, 2017
Licensed Content Publisher	Royal Society of Chemistry
Licensed Content Publication	Chemical Communications (Cambridge)
Licensed Content Title	High yield synthesis of a new fullerene linker and its use in the formation of a linear coordination polymer by silver complexation
Licensed Content Author	Ping Peng,Fang-Fang Li,Faye L. Bowles,Venkata S. Pavan K. Neti,Alejandro J. Metta-Magana,Marilyn M. Olmstead,Alan L. Balch,Luis Echegoyen
Licensed Content Date	Feb 21, 2013
Licensed Content Volume	49
Licensed Content Issue	31
Type of Use	Thesis/Dissertation
Requestor type	academic/educational
Portion	figures/tables/images
Number of figures/tables/images	1
Format	print and electronic
Distribution quantity	1
Will you be translating?	no
Order reference number	
Title of the thesis/dissertation	Design and regioselective synthesis of fullerene derivatives for metal-organic hybrid architectures
Expected completion date	Jun 2017
Estimated size	160
Requestor Location	Catalina Suarez 4111 Westcity Ct EL PASO, TX 79902 United States Attn: Catalina Suarez

APPENDIX 3

ROYAL SOCIETY OF CHEMISTRY LICENSE TERMS AND CONDITIONS

Jun 10, 2017

This Agreement between Catalina Suarez ("You") and Royal Society of Chemistry ("Royal Society of Chemistry") consists of your license details and the terms and conditions provided by Royal Society of Chemistry and Copyright Clearance Center.

License Number	4125501454927
License date	Jun 10, 2017
Licensed Content Publisher	Royal Society of Chemistry
Licensed Content Publication	Chemical Society Reviews
Licensed Content Title	Recent advances on simulation and theory of hydrogen storage in metal–organic frameworks and covalent organic frameworks
Licensed Content Author	Sang Soo Han,José L. Mendoza-Cortés,William A. Goddard III
Licensed Content Date	Mar 24, 2009
Licensed Content Volume	38
Licensed Content Issue	5
Type of Use	Thesis/Dissertation
Requestor type	academic/educational
Portion	figures/tables/images
Number of figures/tables/images	1
Format	print and electronic
Distribution quantity	1
Will you be translating?	no
Order reference number	
Title of the thesis/dissertation	Design and regioselective synthesis of fullerene derivatives for metal-organic hybrid architectures
Expected completion date	Jun 2017
Estimated size	160
Requestor Location	Catalina Suarez 4111 Westcity Ct EL PASO, TX 79902 United States Attn: Catalina Suarez
Billing Type	Invoice

CRYSTAL STRUCTURE REPORT FOR COMPLEX 8

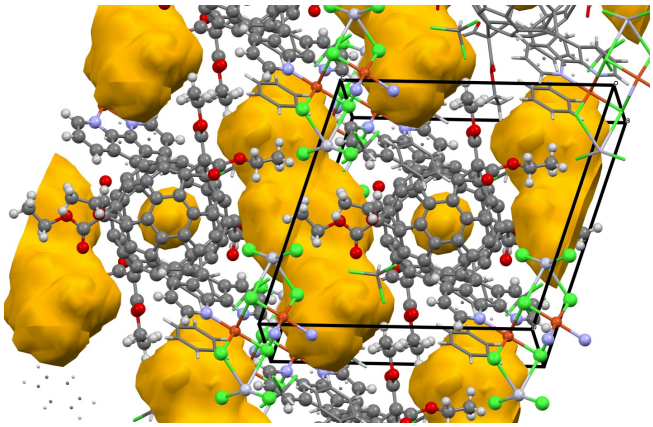

Due to a high disorder the squeeze method was applied, forming the voids showed in the figure. This void was 548 $Å^3$ with 125e^- (4 benzenes approx.), being this the 15% of the total volume.

A specimen of $C_{138}H_{80}Cl_{20}Cu_2Hg_2N_4O_{16}$ was used for the X-ray crystallographic analysis. The X-ray intensity data were measured on a Bruker SMART APEX CCD system equipped with a graphite monochromator and a MoKα fine-focus tube (λ = 0.71073 Å).

The total exposure time was 12.00 hours. The frames were integrated with the Bruker SAINT software package using a narrow-frame algorithm. The integration of the data using a triclinic unit cell yielded a total of 34090 reflections to a maximum θ angle of 25.63° (0.82 Å resolution), of which 13130 were independent (average redundancy 2.596, completeness = 99.4%, R_{int} = 2.09%, R_{sig} = 2.80%) and 11513 (87.68%) were greater than $2\sigma(F^2)$. The final cell constants of a = 14.5140(7) Å, b = 15.9151(8) Å, c = 16.7168(8) Å, α = 71.9440(10)°, β = 87.6690(10)°, γ = 72.2530(10)°, volume = 3490.4(3) $Å^3$, are based upon the refinement of the XYZ-centroids of 9893 reflections above 20 σ(I) with 4.374° < 2θ < 51.24°. Data were corrected for absorption effects using the multi-scan method (SADABS). The ratio of minimum to maximum apparent transmission was 0.905.

The structure was solved and refined using the Bruker SHELXTL Software Package, using the

space group P -1, with Z = 1 for the formula unit, $C_{138}H_{80}Cl_{20}Cu_2Hg_2N_4O_{16}$. The final anisotropic full-matrix least-squares refinement on F^2 with 880 variables converged at R1 = 4.54%, for the observed data and wR2 = 15.68% for all data. The goodness-of-fit was 1.259. The largest peak in the final difference electron density synthesis was 5.561 $e^-/Å^3$ and the largest hole was -1.862 $e^-/Å^3$ with an RMS deviation of 0.130 $e^-/Å^3$. On the basis of the final model, the calculated density was 1.564 g/cm^3 and F(000), 1622 e^-.

Table 1. Sample and crystal data for 1200LE.

Identification code	1200LE	
Chemical formula	$C_{138}H_{80}Cl_{20}Cu_2Hg_2N_4O_{16}$	
Formula weight	3287.32 g/mol	
Temperature	100(2) K	
Wavelength	0.71073 Å	
Crystal system	triclinic	
Space group	P -1	
Unit cell dimensions	a = 14.5140(7) Å	α = 71.9440(10)°
	b = 15.9151(8) Å	β = 87.6690(10)°
	c = 16.7168(8) Å	γ = 72.2530(10)°
Volume	3490.4(3) $Å^3$	
Z	1	
Density (calculated)	1.564 g/cm^3	
Absorption coefficient	2.938 mm^{-1}	
F(000)	1622	

Table 2. Data collection and structure refinement for 1200LE.

Diffractometer	Bruker SMART APEX CCD
Radiation source	fine-focus tube, MoKα
Theta range for data collection	1.28 to 25.63°
Index ranges	-17<=h<=15, -19<=k<=13, -20<=l<=20
Reflections collected	34090
Independent reflections	13130 [R(int) = 0.0209]
Coverage of independent reflections	99.4%
Absorption correction	multi-scan
Structure solution technique	direct methods

Structure solution program	SHELXS-97(Sheldrick 2008)	
Refinement method	Full-matrix least-squares on F^2	
Refinement program	SHELXL-2014/6 (Sheldrick, 2014)	
Function minimized	$\Sigma w(F_o^2 - F_c^2)^2$	
Data / restraints / parameters	13130 / 210 / 880	
Goodness-of-fit on F^2	1.259	
Δ/σ_{max}	0.001	
Final R indices	11513 data; I>2σ(I)	R1 = 0.0454, wR2 = 0.1516
	all data	R1 = 0.0514, wR2 = 0.1568
Weighting scheme	$w=1/[\sigma^2(F_o^2)+(0.1000P)^2+0.2500P]$ where $P=(F_o^2+2F_c^2)/3$	
Largest diff. peak and hole	5.561 and -1.862 eÅ^{-3}	
R.M.S. deviation from mean	0.130 eÅ^{-3}	

CRYSTAL STRUCTURE REPORT FOR POLYMER 13

A specimen of $C_{68}H_{39}Cl_{28}CuN_2O_8$ was used for the X-ray crystallographic analysis. The X-ray intensity data were measured on a Bruker SMART APEX CCD system equipped with a graphite monochromator and a MoKα fine-focus tube (λ = 0.71073 Å).

The total exposure time was 6.00 hours. The frames were integrated with the Bruker SAINT software package using a narrow-frame algorithm. The integration of the data using a triclinic unit cell yielded a total of 54202 reflections to a maximum θ angle of 30.70° (0.70 Å resolution), of which 23789 were independent (average redundancy 2.278, completeness = 90.6%, R_{int} = 2.10%, R_{sig} = 3.73%) and 16527 (69.47%) were greater than $2\sigma(F^2)$. The final cell constants of a = 15.1240(10) Å, b = 17.1318(11) Å, c = 18.4838(12) Å, α = 65.3580(10)°, β = 76.2870(10)°, γ = 81.3350(10)°, volume = 4221.7(5) Å^3, are based upon the refinement of the XYZ-centroids of 9398 reflections above 20 σ(I) with 4.826° < 2θ < 59.93°. Data were corrected

for absorption effects using the multi-scan method (SADABS). The ratio of minimum to maximum apparent transmission was 0.782.

The structure was solved and refined using the Bruker SHELXTL Software Package, using the space group P -1, with Z = 2 for the formula unit, $C_{68}H_{39}Cl_{28}CuN_2O_8$. The final anisotropic full-matrix least-squares refinement on F^2 with 859 variables converged at R1 = 22.95%, for the observed data and wR2 = 61.04% for all data. The goodness-of-fit was 2.727. The largest peak in the final difference electron density synthesis was 8.791 $e^-/Å^3$ and the largest hole was -2.863 $e^-/Å^3$ with an RMS deviation of 0.432 $e^-/Å^3$. On the basis of the final model, the calculated density was 1.627 g/cm^3 and F(000), 2060 e^-.

Table 1. Sample and crystal data for 1197LE.

Identification code	1197LE	
Chemical formula	$C_{68}H_{39}Cl_{28}CuN_2O_8$	
Formula weight	2068.15 g/mol	
Temperature	100(2) K	
Wavelength	0.71073 Å	
Crystal system	triclinic	
Space group	P -1	
Unit cell dimensions	a = 15.1240(10) Å	α = 65.3580(10)°
	b = 17.1318(11) Å	β = 76.2870(10)°
	c = 18.4838(12) Å	γ = 81.3350(10)°
Volume	4221.7(5) $Å^3$	
Z	2	
Density (calculated)	1.627 g/cm^3	
Absorption coefficient	1.197 mm^{-1}	
F(000)	2060	

Table 2. Data collection and structure refinement for 1197LE.

Diffractometer	Bruker SMART APEX CCD
Radiation source	fine-focus tube, MoKα
Theta range for data collection	1.31 to 30.70°

Index ranges	-20<=h<=21, -24<=k<=22, -26<=l<=21	
Reflections collected	54202	
Independent reflections	23789 [R(int) = 0.0210]	
Coverage of independent reflections	90.6%	
Absorption correction	multi-scan	
Structure solution technique	direct methods	
Structure solution program	SHELXS-97(Sheldrick 2008)	
Refinement method	Full-matrix least-squares on F^2	
Refinement program	SHELXL-2014/6 (Sheldrick, 2014)	
Function minimized	$\Sigma w(F_o^2 - F_c^2)^2$	
Data / restraints / parameters	23789 / 149 / 859	
Goodness-of-fit on F^2	2.727	
Δ/σ_{max}	1.519	
Final R indices	16527 data; I>2σ(I)	R1 = 0.2295, wR2 = 0.5754
	all data	R1 = 0.2612, wR2 = 0.6104
Weighting scheme	$w=1/[\sigma^2(F_o^2)+(0.2000P)^2]$ where $P=(F_o^2+2F_c^2)/3$	
Largest diff. peak and hole	8.791 and -2.863 eÅ^{-3}	
R.M.S. deviation from mean	0.432 eÅ^{-3}	

CRYSTAL STRUCTURE REPORT FOR POLYMER 14

A specimen of $C_{125.10}H_{67.10}Cl_{29.30}CuN_4O_{16}$ was used for the X-ray crystallographic analysis. The X-ray intensity data were measured on a Bruker SMART APEX CCD system equipped with a graphite monochromator and a MoKα fine-focus tube (λ = 0.71073 Å).

The total exposure time was 18.01 hours. The frames were integrated with the Bruker SAINT software package using a narrow-frame algorithm. The integration of the data using a triclinic unit cell yielded a total of 14385 reflections to a maximum θ angle of 27.21° (0.78 Å resolution), of which 14385 were independent (average redundancy 1.000, completeness = 93.7%, R_{int} = 0.00%, R_{sig} = 29.85%) and 5089 (35.38%) were greater than $2\sigma(F^2)$. The final cell

constants of a = 15.113(11) Å, b = 15.658(11) Å, c = 16.500(12) Å, α = 95.428(12)°, β = 114.382(11)°, γ = 100.312(11)°, volume = 3436.(4) $Å^3$, are based upon the refinement of the XYZ-centroids of 2345 reflections above 20 σ(I) with 5.480° < 2θ < 32.04°. Data were corrected for absorption effects using the multi-scan method (SADABS). The ratio of minimum to maximum apparent transmission was 0.497.

The structure was solved and refined using the Bruker SHELXTL Software Package, using the space group P -1, with Z = 1 for the formula unit, $C_{125.10}H_{67.10}Cl_{29.30}CuN_4O_{16}$. The final anisotropic full-matrix least-squares refinement on F^2 with 902 variables converged at R1 = 14.83%, for the observed data and wR2 = 35.22% for all data. The goodness-of-fit was 1.327. The largest peak in the final difference electron density synthesis was 1.494 $e^-/Å^3$ and the largest hole was -0.912 $e^-/Å^3$ with an RMS deviation of 0.189 $e^-/Å^3$. On the basis of the final model, the calculated density was 1.442 g/cm^3 and F(000), 1501 e^-.

Table 1. Sample and crystal data for 1190LE.

Identification code	1190LE	
Chemical formula	$C_{125.10}H_{67.10}Cl_{29.30}CuN_4O_{16}$	
Formula weight	2984.35 g/mol	
MoietyFormula	$C_{110}H_{52}Cl_2CuN_4O_{16}$, C_6H_6, 9.1($CHCl_3$)	
Temperature	100(2) K	
Wavelength	0.71073 Å	
Crystal system	triclinic	
Space group	P -1	
Unit cell dimensions	a = 15.113(11) Å	α = 95.428(12)°
	b = 15.658(11) Å	β = 114.382(11)°
	c = 16.500(12) Å	γ = 100.312(11)°
Volume	3436.(4) $Å^3$	
Z	1	
Density (calculated)	1.442 g/cm^3	
Absorption coefficient	0.789 mm^{-1}	
F(000)	1501	

Table 2. Data collection and structure refinement for 1190LE.

Diffractometer	Bruker SMART APEX CCD
Radiation source	fine-focus tube, MoKα

Theta range for data collection	1.35 to 27.21°	
Index ranges	-19<=h<=19, -20<=k<=20, -21<=l<=19	
Reflections collected	14385	
Independent reflections	14385 [R(int) = 0.0000]	
Coverage of independent reflections	93.7%	
Absorption correction	multi-scan	
Structure solution technique	direct methods	
Structure solution program	SHELXS-97(Sheldrick 2008)	
Refinement method	Full-matrix least-squares on F^2	
Refinement program	SHELXL-2014/6 (Sheldrick, 2014)	
Function minimized	$\Sigma\, w(F_o^2 - F_c^2)^2$	
Data / restraints / parameters	14385 / 177 / 902	
Goodness-of-fit on F^2	1.327	
Δ/σ_{max}	2.219	
Final R indices	5089 data; I>2σ(I)	R1 = 0.1483, wR2 = 0.3103
	all data	R1 = 0.2986, wR2 = 0.3522
Weighting scheme	$w=1/[\sigma^2(F_o^2)+(0.1000P)^2+0.0634P]$ where $P=(F_o^2+2F_c^2)/3$	
Largest diff. peak and hole	1.494 and -0.912 eÅ^{-3}	
R.M.S. deviation from mean	0.189 eÅ^{-3}	

Vita

Catalina Suárez is originally from Cali, Colombia. Since she was a child, she showed interest on life sciences; in high school she worked in a neurobiology research lab in Universidad del Valle. Eager to continue learning more, Catalina decided to pursue a career in life sciences and she studied chemistry at Universidad ICESI.

Catalina got one of the top scores in the admission test and won a scholarship for her entire undergraduate studies. During her Bachelors studies she was an outstanding student and was in the honors list every semester. She started doing research in her sophomore year working in an organic chemistry lab. Later, she decided to explore a different field of chemistry and worked during her last two years of her Bachelors in computational chemistry. Her academic performance and willing to learn new things, allowed her to do two summer internships while she was an undergraduate student. She went in the summer of 2011 to the University of Wisconsin-Madison to work on atmospheric chemistry, and in the summer of 2012 to the University of Texas at El Paso (UTEP) to work in organic chemistry. She came back to UTEP on 2013 to pursue graduate studies in Chemistry and graduated with a Masters of Science in 2017. Catalina has three co-author papers and several first-author papers in preparation. She has experience in different areas such as: organic chemistry, inorganic chemistry, biochemistry and analytical chemistry.

Catalina is a lover of outdoor activities and crossfit. She has completed three Sprint distance triathlons and has participated in two crossfit competitions.